



Design of A Mems Device for Studying Cell Migration and Differentiation

by

Ivan Torres

Student id: 130459769

Thesis submitted in fulfilment of the requirement for the Degree of Doctor of
Philosophy in the Faculty of Science, Agriculture and Engineering

School of Engineering

Newcastle University, United Kingdom

September 2019

Abstract

This work presents a novel device to study forces involved in cell migration using micro force-sensing arrays fabricated of a flexible and optical clear polymer called PDMS (polydimethylsiloxane). These arrays consisted of several micropillars with different arrangements and they were fabricated using soft lithography and replica moulding techniques. Three micropillar dimensions were proposed with a stiffness of 155 nN/ μm , 56 nN/ μm and 34 nN/ μm respectively to detect forces within tens of nanonewton range using image analysis techniques.

Device functionalization was performed with a protein called fibronectin which served as a model for the ECM (extracellular matrix). The novelty of this thesis relies on the adaptation of the functionalization techniques to coat the micropillars top only and not leave protein between pillars. Three different methods were compared including the traditional reverse microprinting technique, silane method and EDC/NHS (1-Ethyl-3-(3-dimethylaminopropyl) carbodiimide/N-hydroxysuccinimide) activation. It was demonstrated that EDC/NHS coupling was the more reliable method to functionalize this type of devices.

Force detection was done by recording videos of a cell migrating in the PDMS micropillars substrates. This cell migration caused deflections on the micropillars and these deflections were detected by a MATLAB code which calculated the corresponding exerting force with a resolution of 0.01 nN. The novelty of the image processing relies on a customised MATLAB code. This code detected the position of each pillar frame by frame; and then, exerted forces are calculated by using a mathematical equation which considers the micropillar stiffness and the relative displacement with respect to the previous frame.

The efficiency of the devices was tested in epithelial cells and fibroblasts. It was demonstrated that devices were efficient to measure local forces of epithelial cell lines A549 and NCI-H226 and it was highlighted the key differences between their migration behaviour. Additionally, it was possible to study how cells sense the surrounding area with its lamellipodium as part of cell migration of A549 cells.

Parallely, devices were tested with human dermal fibroblasts where cell migration was minimal. This minimal migration led to the conclusion that this type of device was not suitable for cell migration studies due to the lack of data to carry a study and therefore,

it is suggested to fabricate a device with a bigger stiffness to enhance cell migration in fibroblast cells.

It was concluded that this device is ideal to study epithelial cell's migration and therefore, processes where its migration are involved for instance metastasis. A better understanding of cell migration of cancerous cells could lead to the development of drugs to stop metastasis.

*To my parents Ivan and Kethy,
for their inspiration, guidance and support to fulfil my studies.*

Acknowledgements

I would like to acknowledge the Ecuadorian government for funding my studies at Newcastle University. I would like to express my sincere gratitude to all the people who are acknowledged here for all the guidance and support during this PhD.

To my supervisor Dr John Hedley for his guidance and patient during this PhD, without him this PhD would not be possible. For his motivation through difficult times and for his advice to overcome work difficulties.

My eternal gratitude to Prof. Paul Millner from the University of Leeds who received me in his bio incubator lab. Prof. Paul Millner and his group contributed with valuable content to this thesis. Specifically, I was trained and allowed to perform the midland blotting procedure which was previously created in his group.

To Prof. Andrew Houlton for allowing me to work with his group in the NanoScience lab at the chemical school. From this group, I would like to give a special acknowledgement to Dr Osama El-Zubir, for his patient and time during the last year of my experiments which greatly improved my device fabrication, characterization and functionalization. I wouldn't be able to succeed in this PhD without Osama El-Zubir guidance. Also, special gratitude to Dr Gema Dura for the guidance to perform the functionalization with EDC/NHS.

To Dr Lucy Eland and Dr Carl Dale for kindly guided me to start my work in my first year. To the group from the Newcastle Institute of Cancer Research to share his facilities with me to perform my final experiments and to Professor Jeremy Lakey and Daniel Peters from medical school for the contribution in the characterization of the protein labelling.

Table of contents

Abstract.....	iii
Acknowledgements.....	vii
Table of contents.....	ix
List of figures.....	xi
List of tables.....	xvi
Glossary of abbreviations.....	xvii
Publications.....	xix
Chapter 1. Introduction.....	1
1.1 Aim and objectives.....	2
Chapter 2. Literature review.....	4
2.1 Cell mechanotransduction.....	6
2.1.1 Cell response to topographical substrates features.....	9
2.1.2 Cell response to substrate stiffness.....	13
2.2 Micro force-sensing arrays (μ FSA).....	20
2.2.1 Micro force-sensing arrays for macro-organisms.....	29
2.3 Summary.....	30
Chapter 3. Device fabrication.....	32
3.1 Introduction.....	32
3.2 Materials and methods.....	32
3.2.1 Finite element analysis.....	32
3.2.2 Designing micropillar arrangements.....	36
3.2.3 Master mould fabrication.....	40
3.2.4 Silicon mould characterization.....	41
3.2.5 Silanization process.....	44
3.2.6 Polydimethylsiloxane (PDMS) micropillar curing and demoulding.....	45
3.3 Results and discussion.....	46
3.4 Summary.....	48

Chapter 4. Device functionalization.....	50
4.1 Introduction	50
4.2 Understanding protein adsorption	50
4.3 Materials, methods and results	52
4.3.1 Fibronectin-FITC labelling methodology	52
4.3.2 Microcontact printing technique (μ CP).....	55
4.3.3 Reverse microcontact printing technique (R μ CP).....	56
4.3.4 Adapted method for reverse micro printing technique	60
4.3.5 Silane method.....	63
4.3.6 Micropillar array functionalization via Glutaraldehyde.....	65
4.3.7 Micropillar array functionalization via EDC/NHS coupling.....	68
4.4 Summary.....	73
Chapter 5. Cell migration studies using PDMS micropillar devices.....	76
5.1 Introduction	76
5.2 Materials and methods	76
5.2.1 Tissue culture preparation	76
5.2.2 Video acquisition.....	77
5.2.3 Data analysis	78
5.2.4 Noise removal.....	81
5.3 Results and discussion.....	84
5.3.1 Cell migration of an epithelial A549 cell line	85
5.3.2 Cell migration of an epithelial NCI-H226 cell line	88
5.3.3 Cell migration of a fibroblast HDF cell line	91
5.4 Summary.....	94
Chapter 6. Conclusion.....	96
6.1 Future work	99
References	101
Appendix A	107

List of figures

Figure 1.1. Bright-field image of (i) Rounded cancerous cells. (ii) Large and flat healthy cells. [4].....	1
Figure 2.1. Frequency response of radio frequency (RF) filter design. S21: RF attenuation through the filter. S11: RF signal reflected to the filter input. [6]	5
Figure 2.2. Cell migration steps during cell mechanotransduction.	6
Figure 2.3. In-plane deformable MEMS design. [23, 24] (A) Cell seeding reservoir. (B) Moveable platform. (C) Support ligaments. (D) Migration gap. (E) Reference surfaces.	7
Figure 2.4. White light optical profilometer set-up [23, 24]. (A) Platform containing several MEMS devices. (B) Holder. (C) Inner chamber. (D) Outer chamber. (E) Micrometre. (F) Spring. (G) Windows distance. (H) Profilometer. (I) 45° mirror. (J, K) windows.	8
Figure 2.5. Single line groove effect on the cell migration path. Showing three behaviours named as cross, turn and constraint [19].	9
Figure 2.6. SEM image of intersecting grooves called micropillars [19].	10
Figure 2.7. Number of cells per mm ² in micropillars with different diameters. Devices were seeded with hepatocytes, fibroblasts and HeLa cells. [20].	11
Figure 2.8. Percentage of cells (A) migrating from flat to pillar surface which stayed in the flat surface (flat) or migrated to the micropillar substrate (pillar). (B) migrating from the micropillar to flat substrate which migrated to the flat surface (flat) or stayed in the micropillar substrate (pillar) [21].	11
Figure 2.9. Cell between pillar substrate with dimensions of 7 µm diameter, 10 µm height and spaced by 10 µm. [21].	12
Figure 2.10. Analysis of focal adhesion (FA) of 3T3 cells lying in a micropillar substrate. (A) covered area (B) Lifetime [21].	13
Figure 2.11. Micropillar arrangement with constant spacing in the “x” direction. Pillar radius: “r”. Horizontal spacing: “S”. Vertical spacing: “l” [33].	15
Figure 2.12. Diagram of the micropillar arrangement with increasing spacing. Pillar radius: “r”. Space between pillars in the “x” and “y” axis: “S” [33].	16
Figure 2.13. Ghasemi et al. substrate. Pillars from the upper region are 6.6 µm long. Pillars from the lower region are 3.9 µm long. Pillars diameter is 1 µm [41].	17
Figure 2.14. Stepped PDMS micropillar illustration [13].	18
Figure 2.15. Cell stress fibre in substrate (a) soft (b) stiff. [13]	18

Figure 2.16. Schematic representation of shear forces induced in a single cell using a PDMS micropillar [9].	19
Figure 2.17. Schematic illustration of the cell-trapping device [49].	20
Figure 2.18. SEM image of micropillars deflected by cell's migration [27].	20
Figure 2.19. Demoulding methods for PDMS micropillars. (A) Using a negative photoresist. (B) Using a positive photoresist [27].	22
Figure 2.20. MDCK cells in μ FSA. (A) HGF absence (B) HGF treated, white arrows shows generated actin protrusions [26].	24
Figure 2.21. Upside-down micropillar configuration [29].	25
Figure 2.22. Force orientation vs Focal adhesion direction plot [29].	25
Figure 2.23. Cell average force vs stiffness (A) MDCK (B) 3T3 cell lines [30].	26
Figure 2.24. Maximum pulling force of S180 (isolated) and S180 cells expressing Cad7, E-cad and N-cad [34].	27
Figure 2.25. Force versus focal adhesion area for BPASMCs cells. Blue area corresponds to focal adhesions smaller than $1 \mu\text{m}^2$ [36].	28
Figure 2.26. Human dermal fibroblasts (HDF) graphs. (a) Focal adhesion area against generated forces (b) relationship between focal adhesion fluorescence intensity and force (c) focal adhesion orientation versus force orientation [38].	29
Figure 2.27. Coloured micropillar array [50]. (a) Coloured micropillars under the microscope (b) macroscale image (c) <i>Drosophila melanogaster</i> (d) <i>Caenorhabditis elegans</i> .	30
Figure 3.1. Cross-sectional areas of proposed micropillars. Two circulars with $2 \mu\text{m}$ and $3 \mu\text{m}$ respectively and one elliptical with a major axis of $3 \mu\text{m}$ and a minor axis of $2 \mu\text{m}$.	33
Figure 3.2. Illustration of bending and shear stress on the micropillars according to Schoen [51].	34
Figure 3.3. Micropillar finite element analysis. $D=2 \mu\text{m}$ $L= 5 \mu\text{m}$.	35
Figure 3.4. Computer-aided designs (CAD) of silicon wafer designs 1, 2 and 3.	36
Figure 3.5. CAD image of silicon wafer design 4.	38
Figure 3.6. CAD images of silicon wafer designs 5 and 6.	38
Figure 3.7. CAD images of silicon wafer designs 7, 8 and 9.	39
Figure 3.8. CAD images of silicon wafer designs 9 and 11.	40
Figure 3.9 SEM image of a cross-sectional area of $5 \mu\text{m}$ depth silicon chips.	43
Figure 3.10. Profilometer results for $5\text{-}\mu\text{m}$ Silicon chip.	44

Figure 3.11. SEM images of torn PDMS pillars (left) and incrustated PDMS on the silicon wafer (right).	44
Figure 3.12 SEM image of PDMS pillars. (left) before CPD. (right) after CPD.	46
Figure 3.13. SEM images of PDMS pillars of 3 μm diameter and 5 μm length.....	46
Figure 3.14. Profilometer PDMS micropillar characterisation.	47
Figure 3.15. AFM results of PDMS micropillars.....	47
Figure 4.1. PDMS chemical structure [59].	52
Figure 4.2. Nanodrop results from a FITC-Fibronectin labelling.	53
Figure 4.3. SDS-PAGE results of FITC-Fibronectin solution (a) Coomassie Brilliant Blue and (b) fluorescent FITC filter.....	55
Figure 4.4. Traditional microcontact printing technique[79].	56
Figure 4.5. Soft lithography process flow.	57
Figure 4.6. Protein transfer by soft lithography. 25 s exposure time.....	58
Figure 4.7. Non-uniformity protein transfer by soft lithography. 1 s exposure time. 5 min stamp pillar contact time.....	58
Figure 4.8. (Left) Contact angle before treatment. (Right) Contact angle after exposing for 90 s to oxygen plasma.	59
Figure 4.9. Water contact angle vs oxygen plasma exposure time in seconds.	59
Figure 4.10. Adapted microcontact printing technique schematic view. Protein in the glass stamp is pressed against the tip of the pillars with the aid of a 20 g weight.	61
Figure 4.11. Adapted method for μCP (Left) fluorescent. (Right) brightfield.....	62
Figure 4.12. Adapted method for μCP showing the edge of printing (Left) fluorescent and brightfield image (right).....	62
Figure 4.13. Silane method. (Left) fluorescent image of protein adsorption showing “bridges” between pillars. (Right) brightfield image used as control.	64
Figure 4.14. Silane method results. (Left) Fluorescent image of successful protein adsorption. (Right) brightfield image used as control.	64
Figure 4.15. Relationship between swelling ratio and solubility parameter. Solvents are ranked according to his ability to swell PDMS [92].	65
Figure 4.16. Schematic illustration of PDMS functionalization with GA [54].	67
Figure 4.17. Micropillar array functionalization with glutaraldehyde crosslinker. (left) fluorescent (right) brightfield.....	68
Figure 4.18. Schematic illustration of EDC/NHS coupling.	69
Figure 4.19. Midland blotting overview. Target groups (A) NH_2 (B) COOH [102].	70

Figure 4.20. Chemiluminescence of NH ₂ groups using Midland blotting procedure in PDMS micropillars. (A) APTES Treated (B) APTES untreated.	72
Figure 4.21. Midland blotting validation for carboxyl groups. (A) and (B) were functionalized samples with EDC/NHS. (C) and (D) were non-functionalized control samples. (D) without adding Biotin during Midland blotting procedure.	73
Figure 4.22. Confocal microscope image of ECM protein in EDC/NHS functionalized devices. (left) fluorescent (right) brightfield.	73
Figure 5.1. Schematic view of experimental set-up in an inverted microscope. PDMS micropillar devices were placed upside down in a metallic chamber with a coverslip glass bottom.	77
Figure 5.2. MDCK cell migration video processed in MATLAB [104].	78
Figure 5.3. First and last frame from a video of a migrating A549 cell.	82
Figure 5.4. Original vs corrected noise by Gaussian filtering of pillar 2.	82
Figure 5.5. Displacement vs time plot. Pillar 7 and pillar 10 were control samples. Pillar 1 and pillar 2 were pillars deflected by A549 cells.	83
Figure 5.6. Removing motion noise from pillar 2 using control samples.	84
Figure 5.7. Cell lying in a micropillar device with pillars with 2 μm diameter and 5 μm length.	84
Figure 5.8. Two behaviours of a cell a migrating A549 cell in micropillar devices with 3 μm diameter and 5 μm length. Migration from (a) to (b) migration. Cell lamellipodium exploring the surrounding area from (b) to (c).	85
Figure 5.9. Boxplot of migration forces of an A549 cell. The central red line indicates the median, and the bottom and top edges of the box indicate the 25th and 75th percentiles, respectively. The whiskers extend to the most extreme data points not considered outliers, and the outliers are marked with a red '+' symbol.	86
Figure 5.10. Force vs time plot of relevant micropillars during cell migration.	87
Figure 5.11. Forces in relevant micropillars in cell lamellipodium exploration.	87
Figure 5.12. NCI-H226 cell migrating in micropillar device.	89
Figure 5.13. Boxplot of exerted forces of an NCI-H226 cell. On each box, the central red line indicates the median, and the bottom and top edges of the box indicate the 25th and 75th percentiles, respectively. The whiskers extend to the most extreme data points not considered outliers.	89
Figure 5.14. Force vs time plot of pillars 1,2,4 and 6 of NCI-H226 migrating cell.	90
Figure 5.15. Force vs time plot of pillars 3,5 and 7 of NCI-H226 migrating cell.	91
Figure 5.16. HDF cell migrating in a micropillar array.	91

Figure 5.17. Boxplot of exerted forces of an HDF migrating cell. On each box, the central red line indicates the median, and the bottom and top edges of the box indicate the 25th and 75th percentiles, respectively. The whiskers extend to the most extreme data points not considered outliers, and the outliers are marked with a red '+' symbol.

.....92

Figure 5.18. Force vs time plot of pillars 2,4, 6 and 13 of an HDF migrating cell.....93

Figure 5.19. Force vs time plot of pillars 10,12, 15 and 16 of an HDF cell.94

List of tables

Table 2.1. Immunofluorescence analysis and AFM measurements in tissues of seven patients with different types of cancer [4].	4
Table 2.2. Previous PDMS micro force sensing arrays studies.	23
Table 3.1. FEA results and its approximation to Euler and Schoen equation.	35
Table 3.2 SEM images of fabricated silicon master moulds.	41

Glossary of abbreviations

μm	Micrometre
AFM	Atomic force microscope
APTES	(3-Aminopropyl) triethoxysilane
CAD	Computer-aided design
cal	Calorie
CH_3	Methyl group
cm	Centimetre
CO_2	Carbon dioxide
COOH	Carboxyl group
CPD	Critical point drying
DI water	Deionized water
DMEM	Dublecco's modified eagle medium
DMSO	Dimethyl sulfoxide
DNA	Deoxyribonucleic acid
DRIE	Deep reactive ion etching
ECL	Enhanced chemiluminescence
ECM	Extracellular matrix
EDC	1-Ethyl-3-(3-dimethylaminopropyl) carbodiimide
FEA	Finite element analysis
FITC	Fluorescein isothiocyanate
GA	Glutaraldehyde
HBE	Human bronchial epithelial cell
HDF	Human dermal fibroblast cell
HGF	Hepatocyte growth factor
HMDS	Hexamethyldisilane
HRP	Horseradish peroxidase
IPA	Isopropyl alcohol
m	Metre
MCF	Mouse embryonic fibroblast cell
MDCK	Madin-Darby Canine kidney cell
MEMS	Microelectromechanical systems
mm	Millimetre
MPa	Mega pascal
MW	Molecular weight
NH_2	Primary amine group
NHS	N-hydroxysuccinimide
NICR	Newcastle institute of cancer research
nN	Nano newton
NRK	Normal rat kidney cell
PBS	Phosphate buffered saline
PDMS	Polydimethylsiloxane

RF	Radiofrequency
RPM	Revolutions per minute
s	Second
SCCM	Standard cubic centimetre per minute
SDS	Sodium dodecyl sulphate
SDW	Sterile deionised water
SEM	Scanning electron microscope
SF ₆	Sulfur hexafluoride
SPR	Surface plasmon resonance
UV	Ultraviolet light
W	Watts
XPS	X-ray photoelectron spectroscopy

Publications

Torres I, Eland L, Redfern C, Hedley J. Design of a Mems device for studying cell migration and differentiation. *In: 2017 IEEE Sensors*. 2017, Glasgow, UK: IEEE. DOI: 10.1109/ICSENS.2017.8233948

Chapter 1. Introduction

Nowadays, worldwide cancer is the second death cause. It is estimated that cancer is responsible for 1 of 6 deaths and it took 9.6 million lives in 2018. Globally, age plays a key role where individuals younger than 75 years have a 20 % risk of getting cancer and 10% of mortality. The three most common cancers for both sexes are lung, breast and colorectal cancer. This incidence varies according to sex, being breast cancer the most common cancer for females while lung and prostate are for males. [1-3]

An individual is prone to get a certain type of cancer depending on his genetics and exposure to external risk factors. These external risk factors are obesity, poor diet, sedentary lifestyle, alcohol and tobacco. Reducing the exposure to these major cancer risk factors currently leads to prevent 30-50% of the known cancer types. Even though that a cure for cancer at an advanced stage has not been developed, there is a high chance of cure if the cancer is detected at initial stages. This is the reason why the early detection of cancer has been intensely studied to treat it before it spreads into the body when it becomes lethal. [1, 2, 4]

Current techniques for cancerous cell detection; such as Immunofluorescence analysis, focus on shape recognition in which normal healthy cells have a large flat morphology while cancer cells are rounded in shape, see [Figure 1.1](#). However, healthy cells may have similar shape than cancer cells and consequently, the test might provide a false positive error. In order to overcome this, complementary techniques to discriminate cells need to be carried out. [4]

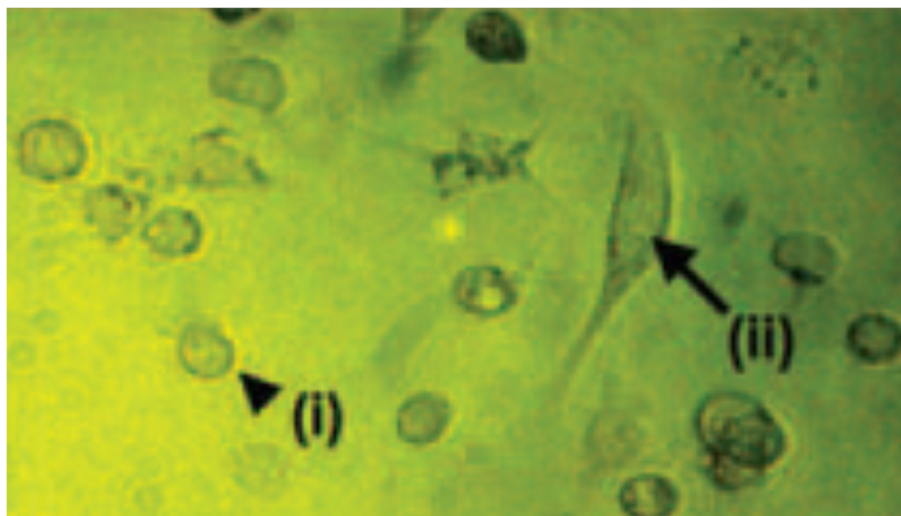


Figure 1.1. Bright-field image of (i) Rounded cancerous cells. (ii) Large and flat healthy cells. [4]

Previous studies demonstrated that healthy cells could differentiate from cancerous cells by measuring their mechanical properties using atomic force microscopy (AFM) [4, 5] and electrical properties [6]. However, AFM tip could create artefacts that might give erroneous measurements while electrical based devices are effective, but they need to operate within specific conditions. Consequently, a few studies [7-9] suggested that cells could be differentiated by analysing their migration; this is because cell migration plays a key role during metastasis. In order to achieve this, researchers studied the influence of substrate stiffness [10-18], substrate topography [19-21] and generated forces during cell migration [7, 8, 13, 22-39].

Microelectromechanical systems (MEMS) are used due to the size of the cells; particularly, an optical-mechanical method using Polydimethylsiloxane (PDMS) micropillars provides a powerful method to study cell migration which can sense local forces in the order of few nanonewton. [13, 22, 25-39]

1.1 Aim and objectives

The aim of this project is to fabricate a MEMS device using a PDMS micropillar array to study cell migration against changes in substrate topography, stiffness and micropillar arrangement. It is important to highlight that a better understanding of the cell migration behaviour could give insights on the mechanisms of cell metastasis in cancer research which may lead to the development of techniques or drugs to fight cancer.

In order to achieve this, the following objectives are set:

1. Choose desired mechanical properties, micropillar shape, dimensions and arrangement.
2. Compare theoretical pillar deflection against finite element analysis (FEA).
3. Fabricate and characterise the mould for micropillar fabrication.
4. Provide a reliable method to fabricate PDMS micropillars.
5. Fabricate and characterise the PDMS micropillar devices.
6. Explore and provide a robust method to functionalized PDMS micropillars.
7. Test the reliability of the fabricated device for cell migration studies.

Six chapters structure the following thesis. [Chapter 1](#) is an introduction to cancer research and the importance to study cell migration, set aim, objectives, and an outline of how the thesis is organised is presented. [Chapter 2](#) contains a review of previous studies to differentiate cancerous cells, cell mechanotransduction and how it is affected

by topography and stiffness features. Furthermore, an introduction to micropillar technology is presented with a review of the most recent studies.

[Chapter 3](#) presents the finite element analysis of the micropillar device, silicon mould fabrication and PDMS moulding technique and solutions to common problems during demoulding are proposed. Every step is accompanied by its respective characterisation. [Chapter 4](#) starts with a deep study in protein adsorption, focusing on the electrical and surface energy conditions to achieve an optimal functionalization. This includes the preparation of a solution containing the ECM protein and a range of methodologies to functionalize specific areas of our devices with their respective characterisation. These methodologies are analysed according to their repeatability. In [Chapter 5](#) results are presented where the reliability for cell migration studies is tested. This includes methodologies to grow cells, video tracking analysis and acquisition of migrating forces. [Chapter 6](#) covers a conclusion of the work done during this thesis addressing achievements, limitations, and suggested future work.

Chapter 2. Literature review

This chapter includes an overview of devices that differentiate healthy cells from cancerous cells and showing their advantages and limitations. Additionally, an introduction to cell migration studies for cancer research with the aim to aid researchers in the development of tools and drugs to fight metastasis is presented in this section; with a special focus on the study of how cell migration is affected by the substrate topography and stiffness. These studies are called Mechanotransduction. Furthermore, an introduction to micropillar technology is presented with a review of the most recent studies. mechanotransduction, cell migration and metastasis in cancer

Table 2.1. Immunofluorescence analysis and AFM measurements in tissues of seven patients with different types of cancer [4].

Case	Age/sex	Disease	Immuno fluorescence analysis	Stiffness (kPa). *Cancerous*	Stiffness (kPa). *Normal
1	52/fem	Lung	Positive	0.56±0.09	2.10±0.79
2	60/fem	Lung	Positive	0.52±0.12	2.05±0.87
3	49/fem	Breast	Positive	0.50±0.08	1.93±0.50
4	85/male	Pancreas	Positive	0.54±0.08	0.54±0.12
5	40/male	Liver	Negative	-	1.86±0.50
6	47/male	Liver	Negative	-	1.75±0.61
7	92/fem	Skin	Negative	-	2.09±0.98

***stiffness measurements using an atomic force microscope (AFM)**

For example, Cross et al [4] using an Atomic Force Microscope (AFM) succeed to make a clear distinction between healthy and cancerous cells by measuring its stiffness. In this study, it was demonstrated that cells from different types of cancer have 70% lower stiffness than the corresponding healthy cells. These results fit with parallel immunofluorescence test results to define if they are positive or negative for cancer, see Table 2.1. The immunofluorescent test used three markers to detect cancerous cells; these markers are Calretinin, Ber-EP4 and B72.3. Calretinin characterises to be positive in healthy cells but negative in metastatic adenocarcinoma; on the other hand,

Be-rEp4 and B72.3 are positive in metastatic adenocarcinoma but negative in healthy cells.

Nevertheless, mechanical techniques might provide an erroneous result due to the presence of artefacts as seen in case 4 from Table 2.1 that both cancerous and normal cells have the same stiffness value. These artefacts may be created because of external loads exerted in the cell. Therefore, techniques which do not apply external loading in the cells has been tested [6-8, 19, 20, 24-29], these are called techniques called non-contact methods. These techniques succeeded in cell discrimination between cancerous and healthy cells without the creation of artefacts in the cell.

Non-contact methods may be classified by chemical, electronic or optical means [24]. Chemical methods are very efficient but the sample can be largely chemically altered prior analysis; therefore, strict procedures need to be implemented to minimize the secondary effects of the chemicals [6].

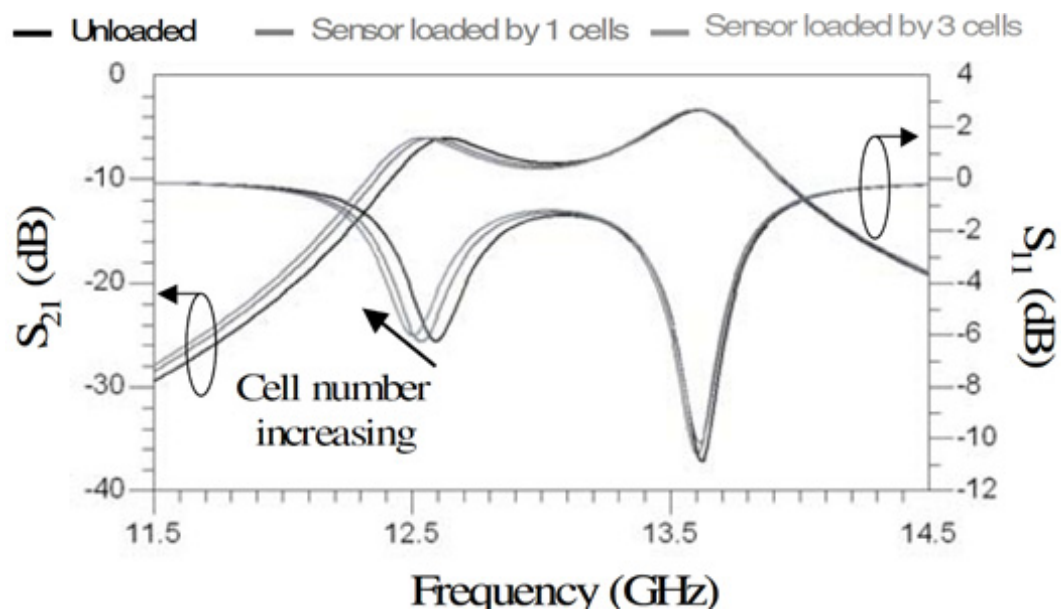


Figure 2.1. Frequency response of radio frequency (RF) filter design. S_{21} : RF attenuation through the filter. S_{11} : RF signal reflected to the filter input. [6]

Electronic techniques are very promising for instance, a previous study[6] performed cell discrimination by measuring its cell electrical impedance. Cell electrical impedance is defined by its permittivity and conductivity where cell discrimination is possible because cancerous cells have larger permittivity and conductivity than healthy cells. Another important fact is that these two parameters vary according to the cell physiological state, morphology and type. Moreover, this study provides a method to efficiently recognize a specific cell type. Cell detection is due to the induced inter

resonator increment which generates a frequency shift response that is linked to the cell electrical impedance using a simple RLC circuit. The sensitivity of this device relies on the amplitude of the frequency shift, results are presented in [Figure 2.1](#) [6].

This device has enormous potential for cell discrimination and differentiation with high sensitivity even for one cell detection. However, it is limited to work under specific conditions such as a narrow frequency range. Furthermore, the efficiency might be compromised if a large group of cells are attached to the device at the same time.

2.1 Cell mechanotransduction

There is a special focus on cell migration since it is involved in essential processes for instance wound healing, scaffold colonization and metastasis [7, 8, 19, 25-27]. Metastasis is the spread of cancerous cells in the body even if they are not directly connected through the circulatory system [8, 26, 40]. Therefore, recent studies focus on understanding the mechanical behaviour behind cell migration where processes inside the cell generate forces to move the cell forward [26]. These studies aim to understand how cells do migration, differentiation and proliferation in response to external mechanical cues such as substrate stiffness [28, 30-32, 41] and topography [19-21, 42] as part of the mechanism of the mechanotransduction process.

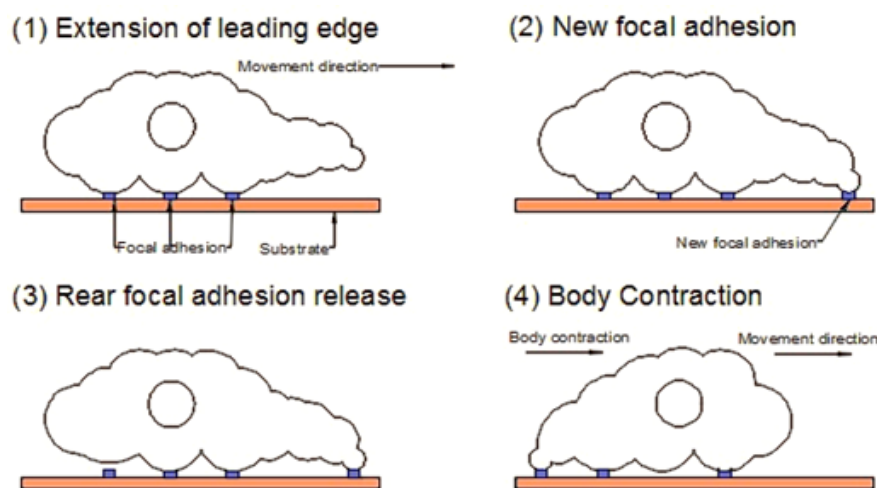


Figure 2.2. Cell migration steps during cell mechanotransduction.

Cell mechanotransduction is the process of sensing external mechanical stimulation and translating them into electrical or chemical signals within the cell. In this thesis, we focus on the migration response to the external stimulation from the substrate topography and substrate stiffness. Briefly, cell migration is explained in four steps in [Figure 2.2](#). [7, 8, 19]

The cell migration process involves a constant restructuring of the actin cytoskeleton. Migration starts with the extension of the actin cytoskeleton towards cell movement direction and shaping to a structure depending on the mechanical properties of the substrate. This structure may be wide and flat (called lamellipodium) or narrow and finger-like (called filopodium). This is a key step since it determines the cell migration direction.

Then, the extended structure will attach to the substrate via focal adhesions providing support and future force generation. Next step is the detachment of the rear focal adhesion from the substrate. Finally, interactions between molecular motors, called myosin II, initiate contraction of the actin cytoskeleton in the rear part of the cell which allows the cell to move forward.

Consequently, forces involved in cell migration can be measured in a MEMS device using mechanical means by measuring the deflection generated by cell migration [26]. Previous studies [23, 24, 43] attempted to quantify these forces and achieved relevant results. For instance, Swierczewski et al [23, 24] provided a design to measure the net force involved in cell migration using a white light profilometer, design of the device is provided in [Figure 2.3](#).

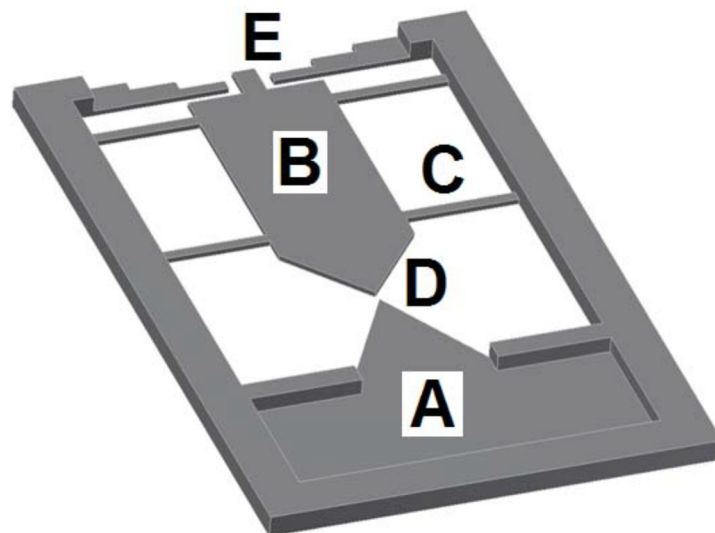


Figure 2.3. In-plane deformable MEMS design. [23, 24]

(A) Cell seeding reservoir. (B) Moveable platform. (C) Support ligaments. (D) Migration gap. (E) Reference surfaces.

This device consists of a moveable platform (B) supported by ligaments (C) acting as springs. Cells migrate from the 4.5 μl cell container (A) to the moveable platform

through a gap (D) causing the platform to deflect. Reference surfaces (E) were used to obtain high-resolution optical profiling for the platform displacement measurement.

This device achieved single force measurements by constraining the number of cells migrating at a time to one. This was done using a tip in the cell reservoir with a width of 10 μm and separated by a gap of 2 μm from a similar 10 μm wide tip on the deflectable platform.

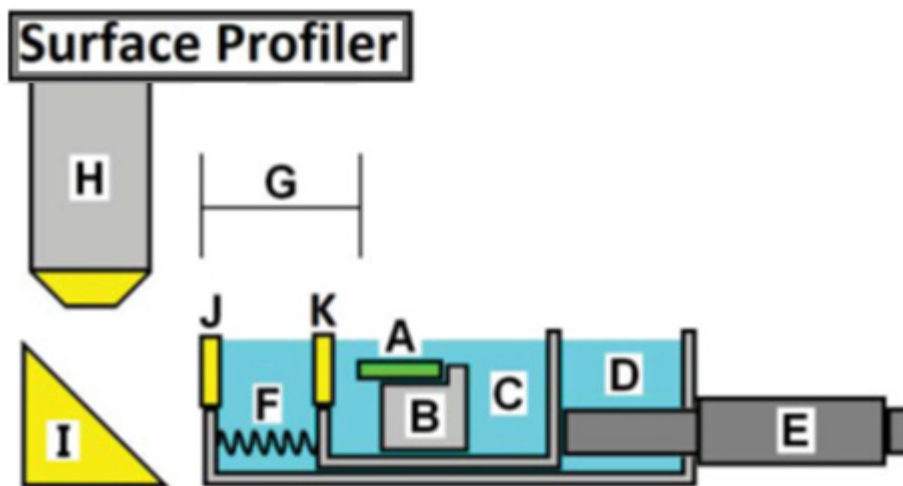


Figure 2.4. White light optical profilometer set-up [23, 24].

(A) Platform containing several MEMS devices. (B) Holder. (C) Inner chamber. (D) Outer chamber. (E) Micrometre. (F) Spring. (G) Windows distance. (H) Profilometer. (I) 45° mirror. (J, K) windows.

This displacement was measured with white light optical profilometry using the set up provided in Figure 2.4. The holder (B) secured the platform which contained the MEMS devices (A). Both (A) and (B) are inside the inner chamber (C) which is filled with cell media and contained a viewing window (K). The inner chamber sat within the outer chamber (D) which contained a viewing window (J), micrometre (E) and a spring (F). This outer chamber is filled with water and actuation on the micrometre screw permitted to adjust the width of water (G) between the two viewing windows (J, K). This variable width of water (G) gave an optical viewing depth equivalent to 3 mm of glass resulting in sharply focused fringes at the reference surface. The white light from the profilometer (H) was able to reach the MEMS device with the help of the mirror (I).

Cell reservoir and movable platform were functionalized with collagen where immortalized human bronchial epithelial cells 16HBE14o (HBE), human dermal fibroblasts (HDF) and A549 lung cancer cell lines were used. Results showed that the

mean force of A549 cells were 317 nN, 461 for HDF cell line and 254 for HBE with a resolution of 126 nN.[24]

Even though several devices succeeded in measuring net migration forces; cells are dynamic and they may remodel the cytoskeleton in response to external stimulation, making difficult to accurately measure local forces produced during cell migration. [43]

2.1.1 Cell response to topographical substrates features

The migration behaviour of cells in non-flat surfaces was studied by Okeyo et al [19], their findings suggested that cell migration path may be guided by the substrate topography. A single line groove causes three migratory paths depending on its width and angle of approach. These paths are classified as “cross”, “constraint” or “turn”, as seen in Figure 2.5.

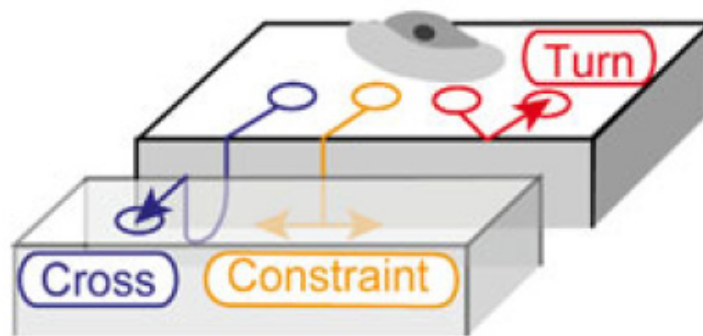


Figure 2.5. Single line groove effect on the cell migration path. Showing three behaviours named as cross, turn and constraint [19].

In the “cross” type behaviour, the cell enters the groove and then moves to the next surface. In the “constraint” type behaviour, the cell enters the groove and moves through it, this behaviour may be used to rectify a cell migration path. For the case of “turn” type behaviour, the cell bridges between the two surfaces and then it changes its direction backwards. In this study, grooves width of 20 μm , 4 μm and 1.5 μm were used for the analysis. Results for the 20 μm wide groove show that 50% of cells crossed, 30% constraint and 20% turned. In the 4 μm wide groove, 20% crossed, 10% constrained and 70% turned. And the 1.5 μm wide groove cause cells to 0% cross, 10% constrain and 90% turn. These results suggest that a wider groove induces the cell to cross while a narrow groove tends to turn. Hence, it was demonstrated that a single line groove may serve as a tool to control cell migration; however, is not completely understood how to successfully constrain the cell migration behaviour. Consequently,

a second set of experiments was carried out where the influence of intersecting grooves in cell migration was studied [19]; intersecting grooves can be called micropillars, a scanning electron microscope (SEM) image of the intersecting grooves is presented in [Figure 2.6](#).

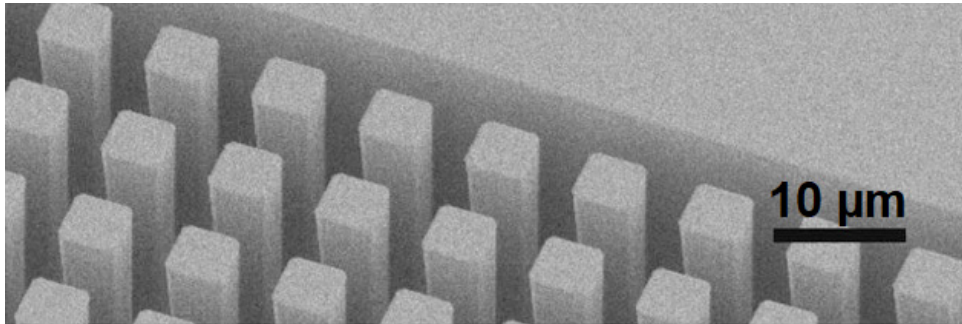


Figure 2.6. SEM image of intersecting grooves called micropillars [19].

The main purpose of this experiment is to expose cells to multiple micropillars at once. Cells experimented two initial behaviours when they move from a flat surface to a micropillar one. The former is to “stay”, this means that cell at first instance goes straight to the groove, then it anchors to the top of the pillars and after a pause, it extends to a neighbouring pillar to move across the groove. The latter is to “turn”, this means that the cell moves straight to the groove where it squashes and then changes its migration direction back to the flat surface. The tendency to “stay” either in 4 μm or 1.5 μm spaced micropillars were 60% and 10% respectively, this clearly shows the huge influence of micropillar spacing in cell migration behaviour. From the results of 4 μm spaced intersecting grooves, it was concluded that the approaching angle between cell migration and the boundary of the micropillar surface can also influence these behaviours. It was seen that if this angle is lower than 50° cells will turn, otherwise they cross. In conclusion, this study proved that changes in micropillars dimensions and spacing can be used to discriminate cells with great efficiency.

Kidambi et al [20] studied the influence of surface topography on cell adhesion and proliferation. Polydimethylsiloxane (PDMS) micropillars with cylindrical shape were fabricated with a cylindrical shape. These pillars were 2.5 μm high with different diameters: 1.25 μm, 2.00 μm, 3.00 μm, 4.00 μm, 5.00 μm, 6.00 μm, 7.00 μm, 8.00 μm, 9.00 μm while the space between micropillars was a constant value of 18 μm,

Primary hepatocytes, fibroblasts and HeLa cells were seeded on these devices; images were taken with a phase-contrast microscope to measure the average area occupied by cells, results are presented in [Figure 2.7](#). Overall, the number of cells

decreased when the pillar diameter is increased, proving that cell proliferation can be controlled by modifying the substrate topography.

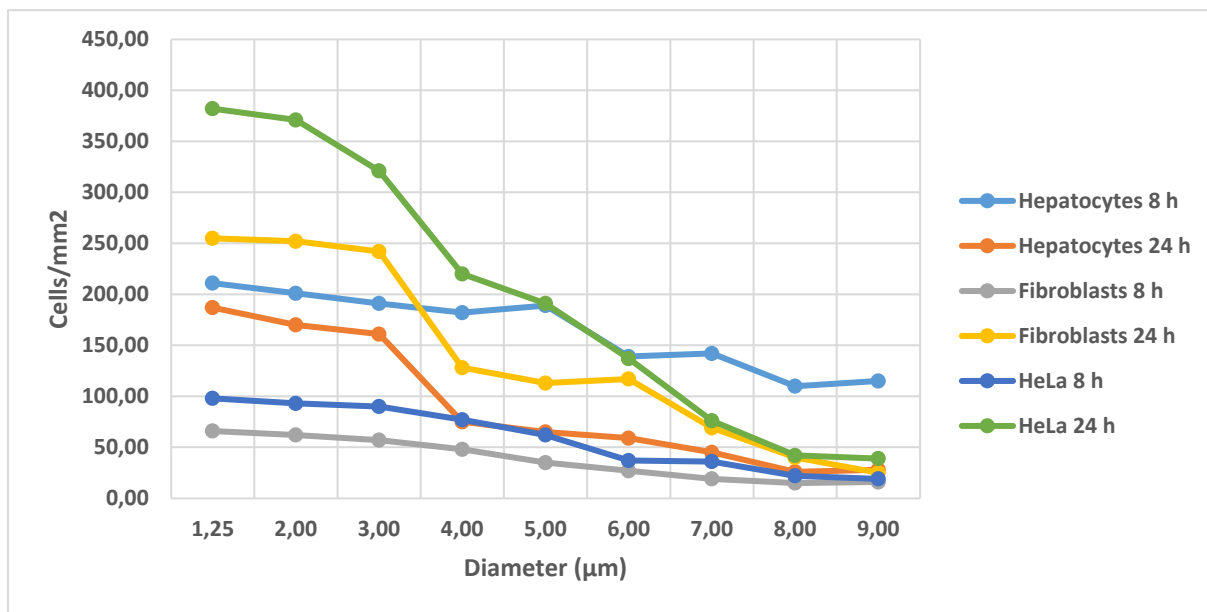


Figure 2.7. Number of cells per mm² in micropillars with different diameters. Devices were seeded with hepatocytes, fibroblasts and HeLa cells. [20].

Ghibaudo et al [21] studied the influence of the topographical features in the migration of 3T3 cells from micropillar to flat surfaces and vice versa. Two different micropillar surfaces were used to see the influence of the topography in the number of migrating cells, as presented in Figure 2.8.

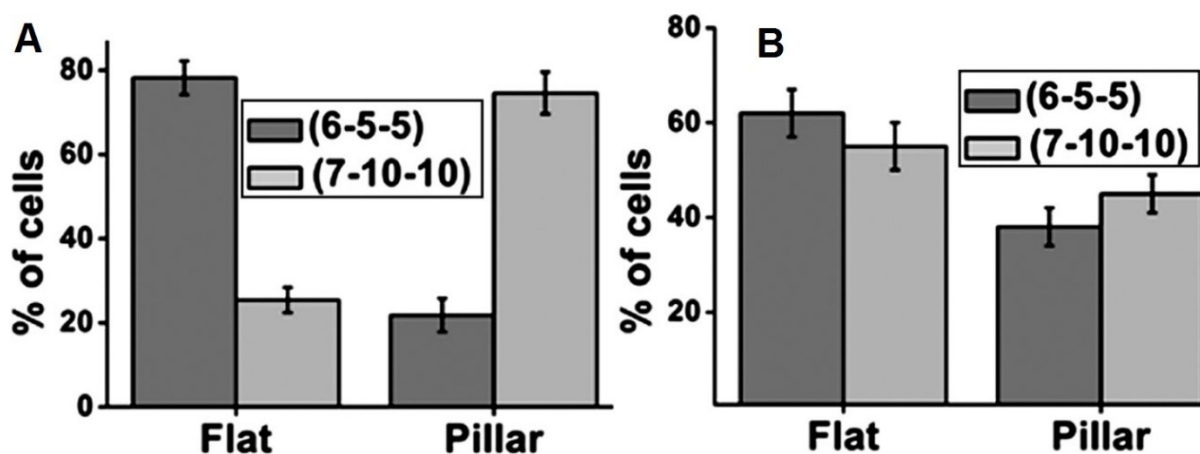


Figure 2.8. Percentage of cells (A) migrating from flat to pillar surface which stayed in the flat surface (flat) or migrated to the micropillar substrate (pillar). (B) migrating from the micropillar to flat substrate which migrated to the flat surface (flat) or stayed in the micropillar substrate (pillar) [21].

The first one has 7 μm diameter, 10 μm height and spaced by 10 μm (7-10-10) and the second one has 6 μm diameter, 5 μm height and spaced 5 μm centre to centre (6-5-5).

According to Ghibaudo et al [21], results proved that the size of features that cell encounters during migration has a substantial influence on it. For instance, the micropillar substrate 6-5-5 presented a 20% of cells migrating from the flat surface to the micropillar surface; on the other hand, 65% of cells migrated from the micropillar substrate to the flat surface. In the micropillar substrate 7-10-10, 75% of cells migrated from the flat surface to the micropillars while in the opposite direction 55% migrated. Ghibaudo et al [21] suggested in his work that a larger space between pillars enhances the migration while a shorter space limits the migration.

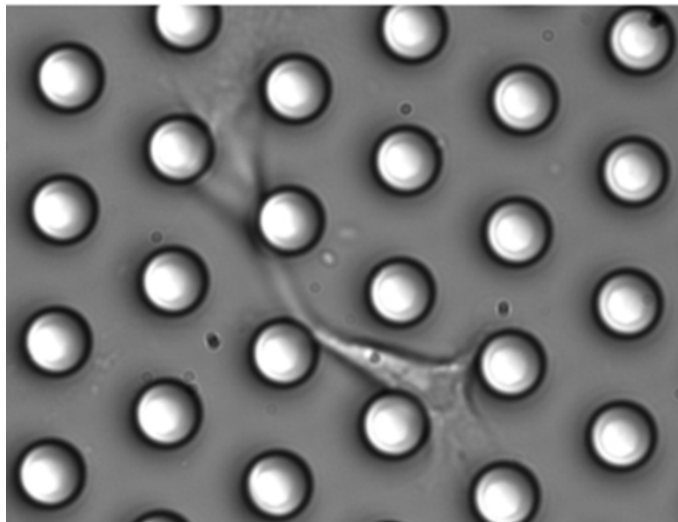


Figure 2.9. Cell between pillar substrate with dimensions of 7 μm diameter, 10 μm height and spaced by 10 μm . [21].

Ghibaudo et al [21] also observed that a high percentage of cells were found between the 10 μm spaced micropillars and therefore its stiffness may be compromised, as seen in [Figure 2.9](#), which led to the author conclusion that these experiments might be erroneous. [21]

On the other hand, in the 5 μm spaced substrate (6-5-5) thin and long protrusions were seen in the top of the pillars, the author suggested that these protrusions would limit the exerted forces to the top of the pillars. Ghibaudo et al [21] stressed that this finding highlights the importance of micropillar spacing, which must be optimised to obtain accurate results. [21]

Finally, 3T3 cells were analysed on the micropillar substrate 7-10-10 (7 μm diameter, 10 μm height and spaced 10 μm centre to centre) and in a flat surface. Cells were seeded overnight, and the migration was recorded for 2 hours. At the beginning of the migration, cells were lying in the flat surface and the focal adhesion area and lifetime were measured. The cells then migrate to the micropillar surface and the focal adhesion area and lifetime were measured again. Results are presented in [Figure 2.10](#) [21].

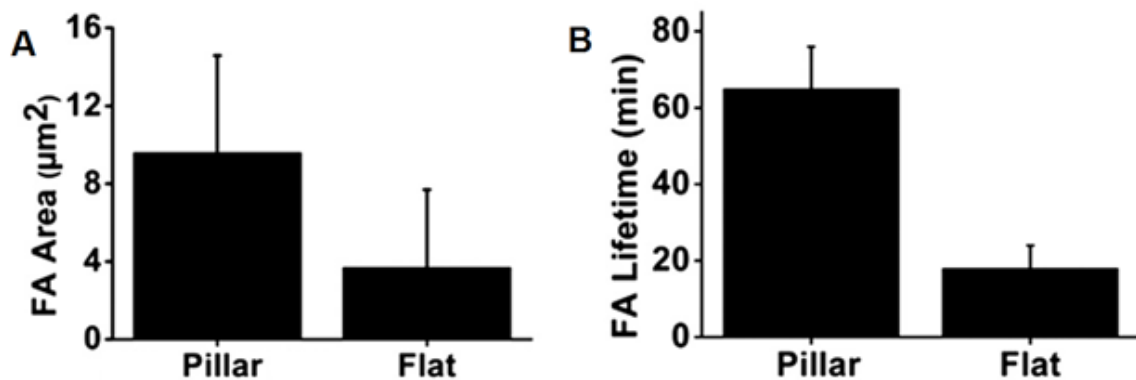


Figure 2.10. Analysis of focal adhesion (FA) of 3T3 cells lying in a micropillar substrate. (A) covered area (B) Lifetime [21].

Both focal adhesion area and lifetime were higher in the micropillar surface. This is a consequence of the cell effort to migrate to the micropillar substrate. By doing this, the cell can exert a bigger force providing more stability during cell migration. This finding explains why the cell moves slower in the micropillars when compared to a flat surface. [21]

2.1.2 Cell response to substrate stiffness.

Substrate rigidity is known to have enormous influence in cell mechanotransduction; stiffness gradients along the substrate might lead the direction of cell migration. This property is called durotaxis. [10-13, 31, 33]

Several substrates with stiffness gradients have been fabricated using photopolymerized hydrogels [16-18]. The stiffness gradient was achieved by controlling the intensity of the ultraviolet (UV) light to certain areas using masks. However, they offer a small range of stiffness gradient and cells struggle to sense it.

In order to offer better stiffness gradient, microfluidics systems in conjunction with diffusion methods have been developed [14, 15]. These systems use microfluidic channels to flow different concentrations of the hydrogel-crosslinker with the aid of a

syringe pump. Then, the device is exposed to radiation from a UV lamp which photopolymerize the hydrogel and efficiently creates a substrate with a stiffness gradient. However, the high cost, difficulties to control and low repeatability of these systems led researchers to find alternative methods to study durotaxis.

Consequently, micropillar arrays are used due to its simplicity, repeatability and low-cost design [25-30, 34-37, 44, 45]. Higa et al [33] studied the cell response against a gradient of stiffness using micropillars with the aid of an extracellular matrix (ECM) protein to enhance cell migration.

The extracellular matrix (ECM) is a 3D network of macromolecules which provides structural and biochemical support to cells. The ECM interacts with the cell surface receptors, called integrins, to regulate cell functions for instance growth, migration and differentiation. The main macromolecules within the ECM are collagens, enzymes, and glycoproteins [46]

Among the glycoproteins within the ECM, Fibronectin plays a key role in cell migration as it creates a bound between collagen and cell-surface integrins where cell migration is achieved by a reorganization of the cell's cytoskeleton. Therefore, fibronectin is the most common protein used to model the ECM for cell migration studies. [47].

Higa et al [33] coated the top of the pillars with Fibronectin to promote cell adhesion and migration. The height of the pillars remained constant with radius increments to create the stiffness gradient. It is important to keep the same percentage of the ECM protein in contact with the cells; otherwise, it might create a chemical effect that will alter cell migration. If the space between pillars is kept constant and the radius is increased, the contact area between cells and substrate is increased. To minimize this effect, the space between pillars needs to be modified according to the radius increment. This percentage of ECM protein in terms of pillar radius and micropillar space is denoted in Eq. 1 [33].

$$\%ECM = \frac{\pi \cdot r^2}{(2 \cdot r_x + S)(2 \cdot r_y + I)} \quad \text{Eq. 1}$$

Where “%ECM” is the percentage of the extracellular matrix protein, “r” is the pillar radius, “S” is the space between pillars in the “x” axis and “I” is the space between pillars in the “y” axis. For this study, %ECM was a constant value of 0.2. Two sets of experiments were carried out, one with cells migrating in the direction of increasing stiffness and vice versa. For the first set of experiments, the space in the “x” direction

“S” is remained constant while the distance in “y” direction “l” is increased on each row of pillars according to Eq. 1. A schematic diagram of the micropillars arrangement is shown in Figure 2.11. Height was kept constant to a value of 7 μm and by increasing the radius in each row, two stiffness gradients were created. The former is a low increasing gradient, which increases 0.5 $\text{nN}/\mu\text{m}$ from 5 to 50 $\text{nN}/\mu\text{m}$ with a radius range of 1-2 μm . The latter is a high increasing gradient which increases 7.5 $\text{nN}/\mu\text{m}$ from 5 to 390 $\text{nN}/\mu\text{m}$ 1-3 μm . Bovine aortic endothelial cells were used and the aim of this set of experiment is to study how the gradient stiffness affects cell migration. [33]

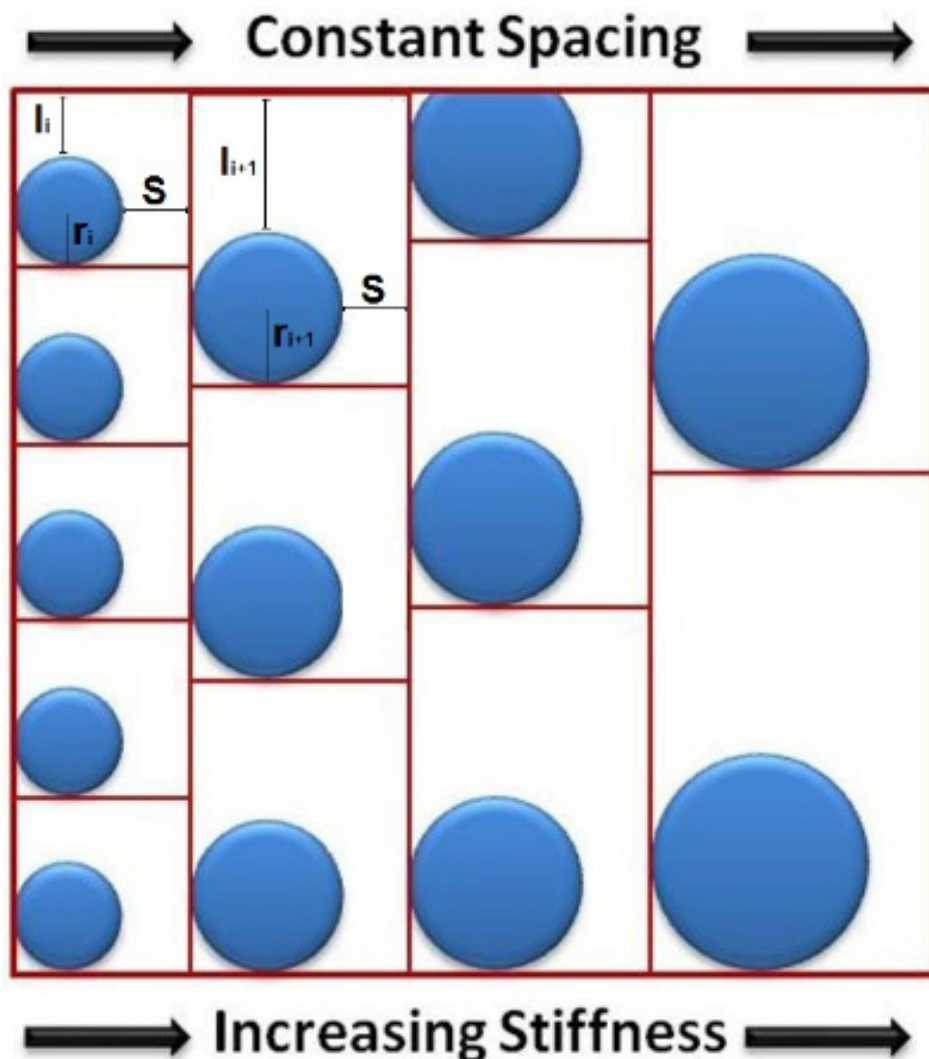


Figure 2.11. Micropillar arrangement with constant spacing in the “x” direction. Pillar radius: “r”. Horizontal spacing: “S”. Vertical spacing: “l” [33].

Results show that cells move quicker in the direction of increasing stiffness than cells moving in the opposite direction. This increment on velocity was higher in micropillars with high stiffness gradient than the ones with low stiffness gradient. This proved that substrate stiffness influence in the cell migration behaviour where cells tend to move

in the direction of increasing stiffness. However, since the space between pillars was constant in the “x” direction but increased in the “y” direction, it may influence the cell migration direction. Hence, it is needed to analyse how the space between pillars affect cell migration while the stiffness is increasing. Therefore, a second set of experiments was carried out where the micropillar spacing “ S_i ” remains equal in the “x” and the “y” direction and this distance “ S_i ” is increased in every row, as shown in [Figure 2.12](#) [33].

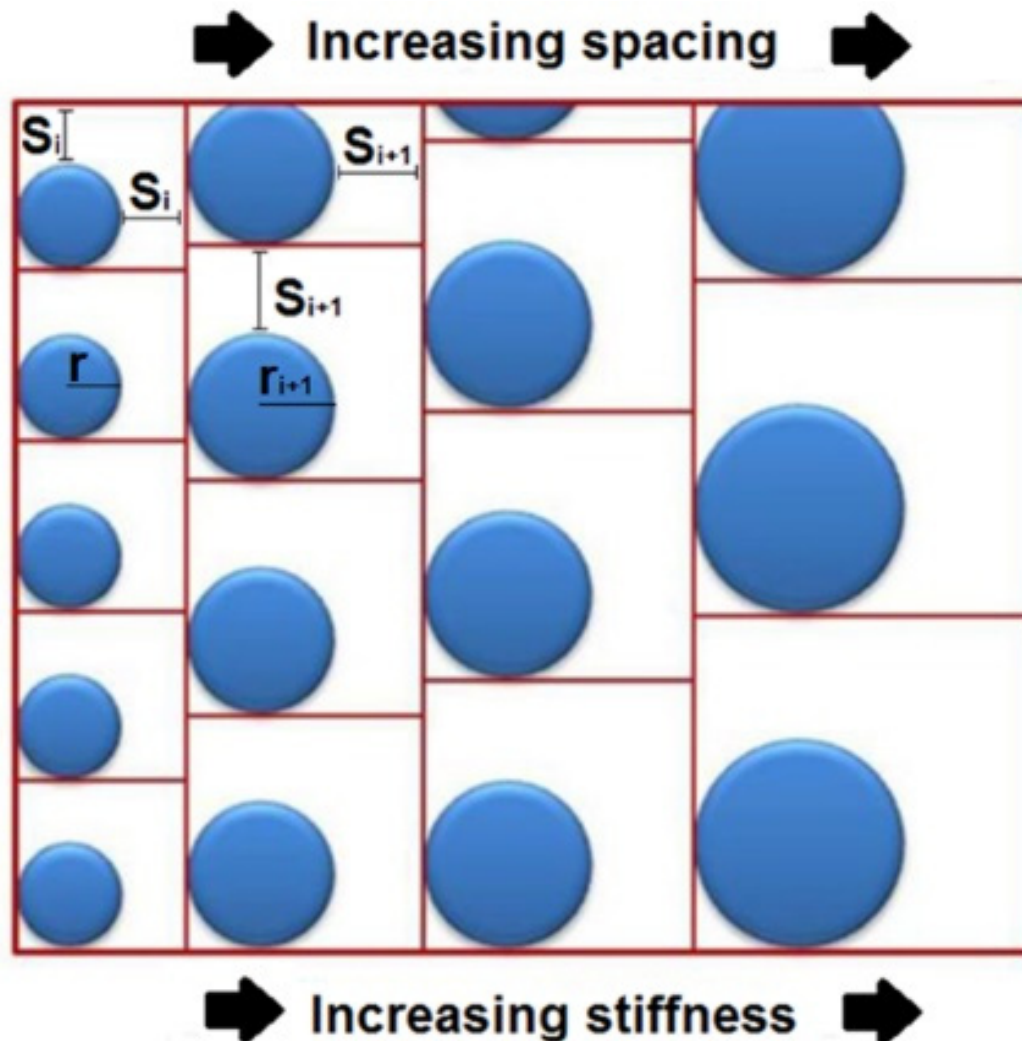


Figure 2.12. Diagram of the micropillar arrangement with increasing spacing. Pillar radius: “r”. Space between pillars in the “x” and “y” axis: “S” [33].

Radius, length of pillars, %ECM and the two types of stiffness gradient are kept the same than the first set of experiments and space between pillars range from 2 to 6 μm . The equation that describes the micropillar features and arrangement is shown in [Eq. 2](#) and it is obtained by replacing “ $S=l$ ” on [Eq. 1](#). [33]

$$\%ECM = \frac{\pi \cdot r^2}{(2 \cdot r + S)^2} \quad \text{Eq. 2}$$

Overall, cells exhibit a lower velocity in the direction of increasing stiffness than the opposite direction. This finding is contradictory to the results from the first set of experiments; therefore, it has been proved that inter-pillar spacing plays a key role in cell migration and it may be more influential than substrate stiffness. Nevertheless, there is not enough evidence for this claim and consequently, it needs to be studied more in depth [33].

An alternative approach to creating a gradient stiffness is to vary the height of the patterns, as described by Ghassemi et al and Fu et al [32, 41]. Fu et al studied cell behaviour against three micropillar substrates with different heights (0.97 μm , 6.10 μm and 12.9 μm) while Ghassemi et al developed a platform containing micropillars with different heights in the same platform, as seen in Figure 2.13. Both studies maintain the %ECM constant along the substrates. Results reconfirm that cells spread better with more actin stress fibres in stiffer areas and there is a migration tendency to stiffer areas compared to the soft ones. [32, 41]

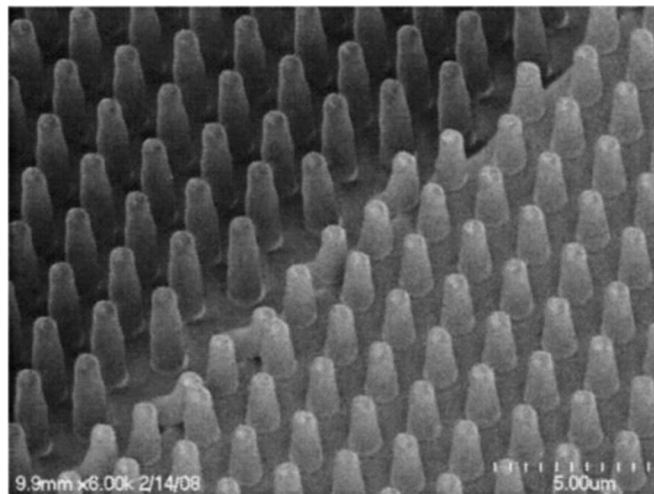


Figure 2.13. Ghassemi et al. substrate. Pillars from the upper region are 6.6 μm long. Pillars from the lower region are 3.9 μm long. Pillars diameter is 1 μm [41].

In another study, Lee et al [13], created a gradient stiffness using stepped micropillars that keep the %ECM constant. Moulds were fabricated with double-step photolithography using a negative photoresist called “Su-8” and then the PDMS was poured on them to create micropillars with two layers. To maintain the %ECM constant and create a gradient stiffness; the top layer diameter was kept uniform to a value of 2

μm while the diameter of the bottom layer was varied according to the desired stiffness gradient, as seen in Figure 2.14. Both layers had a distance between pillars of $10\ \mu\text{m}$.

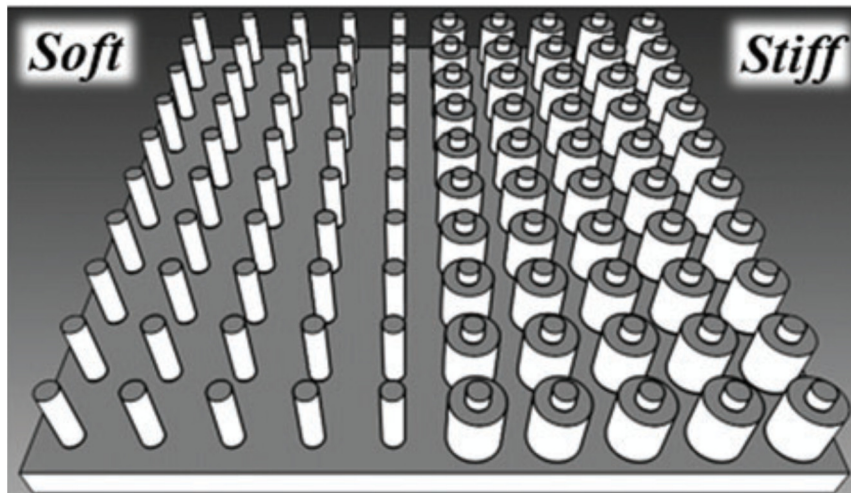


Figure 2.14. Stepped PDMS micropillar illustration [13].

Three gradient stiffnesses were created to analyse the cell behavioural response. The low gradient ($0.5\ \text{nN}\ \mu\text{m}^{-1}$) had increasing diameters from 2 to $3\ \mu\text{m}$. The medium gradient ($5\ \text{nN}\ \mu\text{m}^{-1}$) had increasing diameters from 2 to $5\ \mu\text{m}$ and the high gradient ($50\ \text{nN}\ \mu\text{m}^{-1}$) had increasing diameters from 2 to $7\ \mu\text{m}$. Results show changes in the cell morphology where more cell stress fibres can be seen in the stiff substrate than the soft one, as seen in Figure 2.15. Furthermore, cells preferred to move from the soft pillars to the stiff ones and they moved faster in the substrate with the highest gradient stiffness compared to the low and medium stiffness. [13]

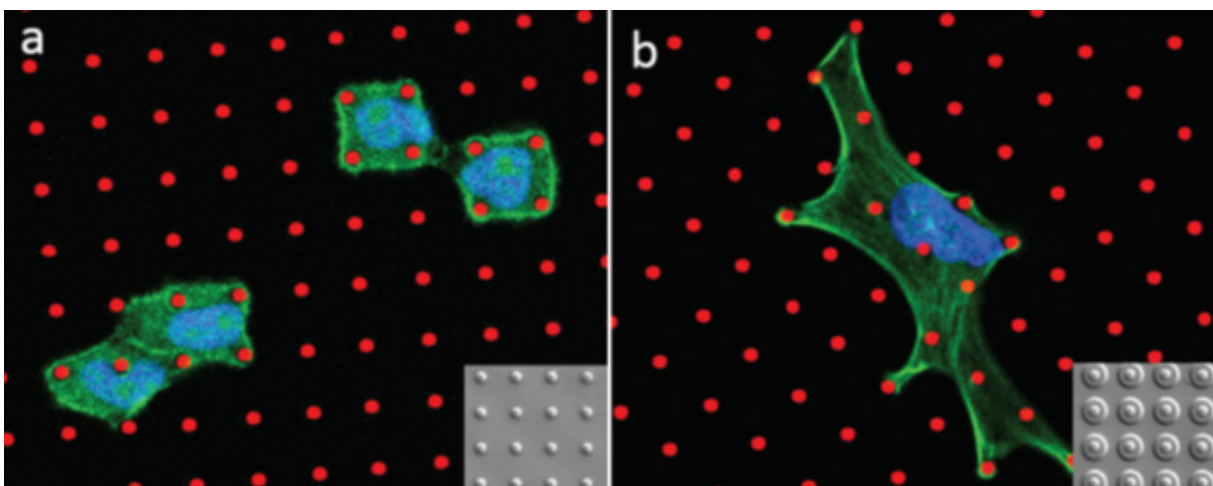


Figure 2.15. Cell stress fibre in substrate (a) soft (b) stiff. [13]

These studies [13, 33] demonstrated the durotaxis effect on cell migration and provided a method that can be used to study cell migration.

In another study, Heil et al [9] study how the cell focal adhesions (FAs) function during cell migration. It is well known that FAs are the link between the cell and the substrate where they transform chemical signals within the cell into mechanical forces and vice versa.

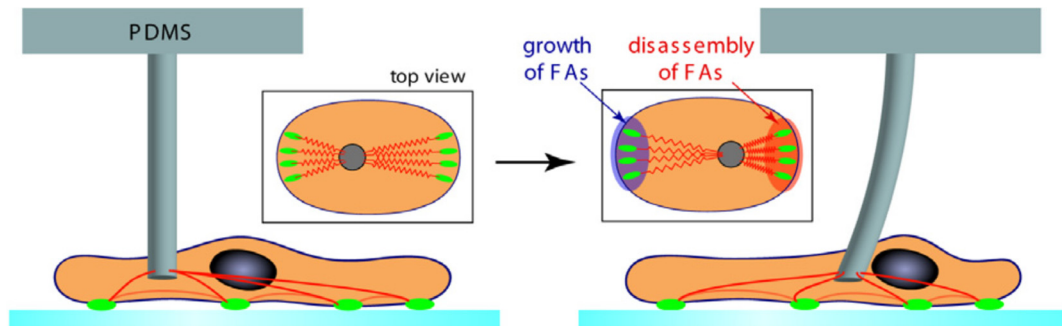


Figure 2.16. Schematic representation of shear forces induced in a single cell using a PDMS micropillar [9].

Previously, Riveline et al [48] proved that FAs growth are led by the internal contraction forces which can be replaced by external loads; however, it is unclear the exact mechanism of interaction between FAs and substrate. In order to achieve this, a single PDMS micropillar is put in contact with the cell and after 15 min the micropillar is moved horizontally to create shear forces, as shown in Figure 2.16 [9].

Results show the FAs react against lateral shear forces between 100-150 nN. The front area of the cell with increased shear forces presented FAs growth; on the other hand, the rear area of the cell with reduced shear forces did not cause any reaction on the FAs. Consequently, cell moved in the same direction of the applied shear stress. [9]

Microposts arrays may be used for multiple purposes apart from mechanotransduction studies. For instance, a novel device for cancer cell capture was developed by Xiao et al [49]. Circulating tumour cells (CTCs) are cells in the bloodstream that can easily spread through the body and its low concentration in the blood make it difficult to isolate them. To isolate them a device was fabricated containing two rows of PDMS micropillars with a diameter of 40 μm , rows are spaced by 600 μm and 15 μm between 2 adjacent pillars, which, corresponds to the size of a tumour cell. Additionally, groves are placed between the micropillars rows to control the flow direction. A schematic illustration is shown in Figure 2.17. Results show that this device has an efficiency of 90% based on the relation between the amounts of captured cancerous cells [49].

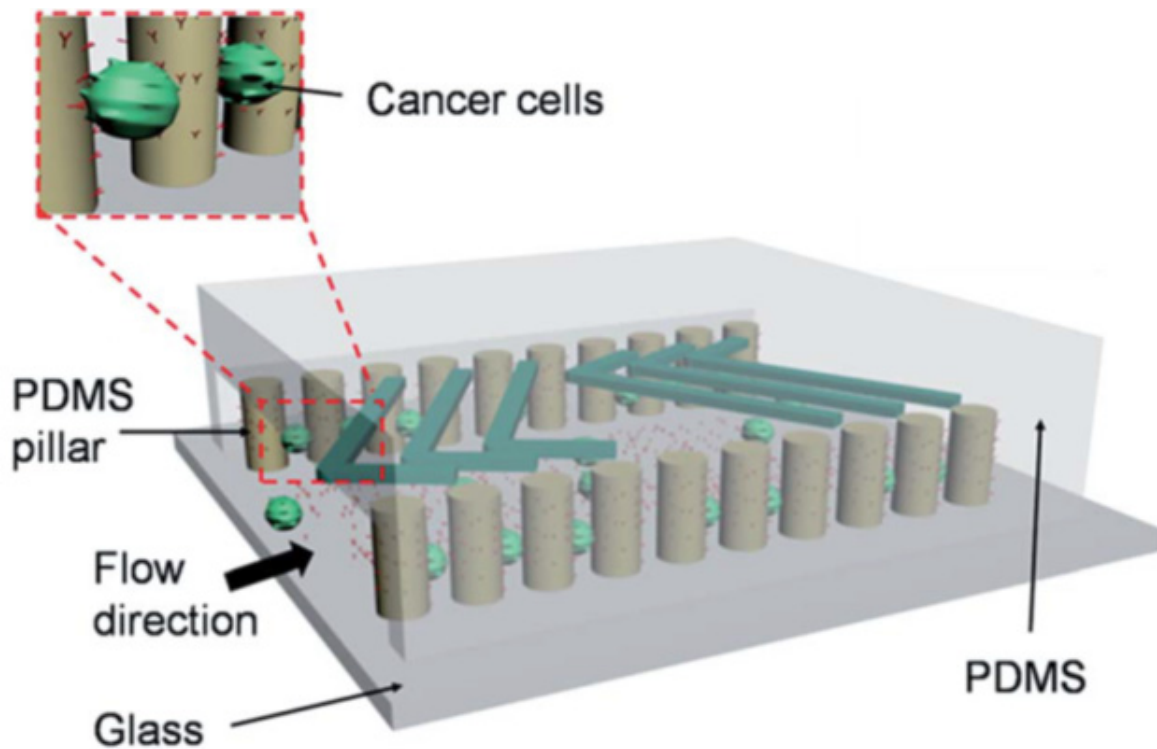


Figure 2.17. Schematic illustration of the cell-trapping device [49].

2.2 Micro force-sensing arrays (μ FSA)

Micropillars could be designed to deflect by the action of migration forces and to constraint the migration forces to the top of the pillars. This allows designing a powerful tool to measure the forces involved during cell migration. Measuring the forces involved during cell migration will enhance the understanding of cell mechanical behaviour response. These micropillars are called micro force sensing arrays (μ FSA), see Figure 2.18. [25-27, 29-32, 34-39, 44, 45]

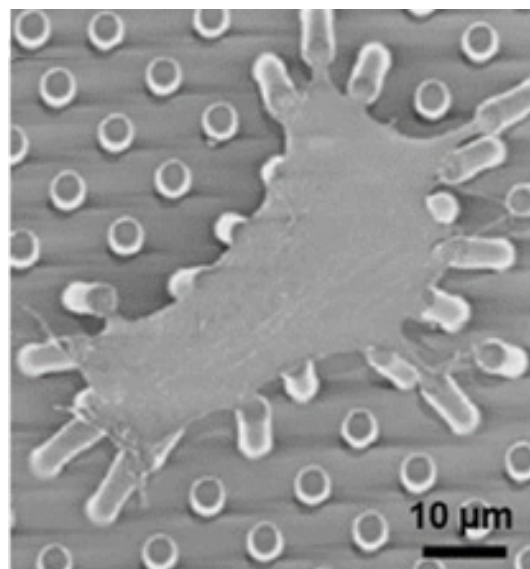


Figure 2.18. SEM image of micropillars deflected by cell's migration [27].

These devices consist of vertical micropillars that are uniformly spaced with the purpose of measuring the deflection generated by cell migration. This device presents three main advantages:

- 1) High sensitivity to measure deflections up to tens of micrometres with generated forces in the order tens of nN, depending on the pillar stiffness [25, 29, 38].
- 2) A simple design allows treating each pillar as a cylinder and therefore the generated forces during migration can be easily measured [25-27, 29-32, 34-39, 44, 45].
- 3) Pillar deflection is independent of the neighbouring pillar; for this reason, local forces can be measured [25-27, 29, 30, 32, 34-38, 45].

As cell migrates, it causes a deflection in the micropillars and this deflection can be calculated by using the Euler-Bernoulli beam theory, see [Eq. 3](#) [25-27, 30, 36, 37, 41].

$$F = k \cdot x = \left(\frac{3}{4} \cdot \pi \cdot E \cdot \frac{r^4}{L^3} \right) \cdot x \quad \text{Eq. 3}$$

Where k is the stiffness, x is the cylinder deflection, E is Young's modulus, r is the cylinder's radius and L is the length of the pillar.

These pillars are often fabricated of silicon [28] or PDMS; where PDMS is preferred over silicon because of its lower Young's modulus. A lower Young's modulus implies a lower spring constant that offers a more sensitive force detection. The two most predominant methods to fabricate these devices are shown in [Figure 2.19](#) [25-27].

These methods differ in the type of photoresist used during the fabrication of the master mould. The first method is shown in [Figure 2.19\(A\)](#), consists in the deposition of a negative photoresist in a silicon wafer such as Su-8. Exposure to UV light causes the negative photoresist to become insoluble to the photoresist developer while the unexposed areas can be dissolved with the developer. After applying the photoresist developer, a photoresist micropillar replica is created which acts as a master mould. Then, PDMS is poured in this master mould to be cured and peeled it off to obtain a PDMS negative replica. To obtain the final device, PDMS is poured in the PDMS negative replica and then cured and peeled off. One PDMS negative replica could be used several times to fabricate multiple PDMS micropillar devices. The advantage of this method is that the master mould is sporadically used to fabricate PDMS negative replicas, avoiding wear and tear of the master mould. A disadvantage of this method

in that the user must handle with extra care when fabricating the PDMS negative replica because the micropillars might break during the first peeling off step.

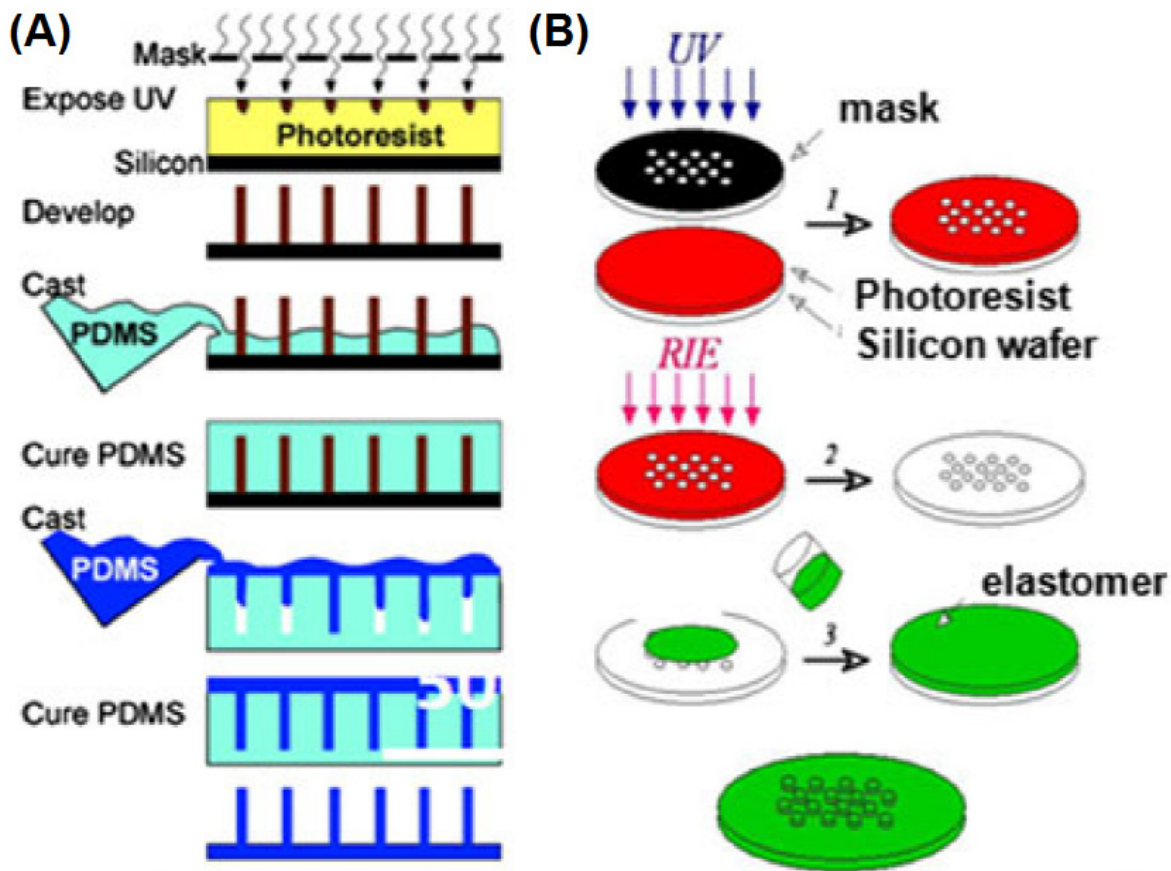


Figure 2.19. Demoulding methods for PDMS micropillars. (A) Using a negative photoresist. (B) Using a positive photoresist [27].

On the other hand, the second method is shown in Figure 2.19(B) uses a positive photoresist to fabricate the master mould. This positive photoresist becomes soluble to the photoresist developer when exposed to UV light and the unexposed areas become insoluble to the developer. This means that the application of the photoresist developer creates a photoresist negative replica of the micropillars. Deep reactive ion etching (DRIE) is then applied which etch the exposed areas of the silicon wafer and creates a silicon negative mould. This silicon negative mould acts as a master mould. Next, PDMS is poured, cured and peeled off from the master to obtain the PDMS micropillar devices. The advantage of this method is that fewer steps are used to fabricate PDMS micropillars and the low risk to damage the master mould during the peeling off step. The disadvantage of this methodology is that the frequent manipulation of the master mould will accelerate its wear and tear.

Previous studies [26, 27, 29-32, 34-39], have successfully demonstrated that forces can be measured using PDMS micropillars, there are summarised in [Table 2.2](#).

Table 2.2. Previous PDMS micro force sensing arrays studies.

Author	Cell line	Dimensions (μm)		Young's modulus (kPa)	Stiffness (nN/ μm)	Force (nN)	
		radius	length			Min-Max	Average
Du Roure[26]	MDCK*	1	6	2000	21.81	1-40	5
		0.5	5.2		2.09	0.1-3	N.G
Digabel [27]	NRK*	1	4.2	2000	64	1-175	10
Van Horn [29]	3T3**	1	6.9	2330	16.71	0-10	4
	MCF7*					0-20	N.G.
Ghibaudo [30]	3T3**	[0.5-1]	[2.8-7]	2000	[1.07-214]	0.03-55	0.08-10.9
	MDCK*					0.03-100	0.01-18
Saez [31]	MDCK*	[0.5-1]	[3.3-5.3]	2000	[2-130]	0.1-100	0.3-10
Saez [37]	MDCK*	[0.5-1]	[2-7]	[1.5-150]	[1-2000]	[0.1-110]	1
Fu [32]	hMSCs	0.915	10.3	2500	3.77	70-1050	N.G
			8.3		7.21	150-1100	N.G
			6.1		18.19	220-1200	N.G
	HUVECs	0.915	12.9		1.92	30-400	N.G
			10.3		3.77	180-780	N.G
			8.3		7.21	150-800	N.G
Jasaitis [34]	S180	1	3.6	2000	100.00	20-75	58
	S-180 Cad7					20-95	75
	S-180 Ecad					20-130	83
	S-180 Ncad					20-140	78
Li [35]	NIH3T3**	1	5	2000	37.69	0.1-1	N.G
Tan [36]	BPASMCs	[1-5]	[3-50]	2500	[2.7-1600]	N.G.	[9-27]
Balaban [38]	HDF**	0.4	2	[10-20]	[0.075-0.15]	[1-30]	10
Ganz [39]	C2	1	3.4	1700	101.9	5-50	15
	GT1-7					5-50	14

*Epithelial, **Fibroblast, N.G: not given data.

Cell lines description: MDCK (Madin-Darby Canine Kidney cells), NRK (Normal Rat Kidney), 3T3 (mouse embryonic fibroblast cells), MCF7 (Michigan Cancer Foundation-7 from human breast cancer), hMSCs (Human mesenchymal stem cells), HUVECs (Human umbilical vein endothelial cells), S180 (Murine Sarcoma), BPASMCs (bovine pulmonary artery smooth muscle cells), HDF (Human Dermal Fibroblast), C2 (mouse myogenic cells), GT1-7 (Hippocampal mouse).

These studies from [Table 2.2](#) [26, 27, 29-32, 34-39], have in common the following findings. Firstly, bigger forces are measured in stiffer micropillars than soft ones. Secondly, reverse microcontact printing technique was used to transfer the ECM protein to the tip of the pillars except for Ganz [39] which used a silanization method; this method will be explained in [section 4.3.5](#). Finally, the maximum exerted forces were located at the edge of the cell where the cell is migrating.

Moreover, Du Roure [26] studied the relationship between cell morphology and traction forces generated by Madin-Darby canine kidney cells (MDCK). These cells were cultured for 1 day at sub-confluency density because no significant pillar deflection was observed at confluency. Then, measurements were acquired before and after treatment with a cell motility promoter called hepatocyte growth factor (HGF). As seen in [Figure 2.20](#), after HGF stimulation cells started to form thin actin protrusions ending in a micropillar top, along with this finding, traction stresses incremented from 1.6 to 3.8 nN/ μm^2 after HGF treatment. This result proves that cell morphology, specifically actin organization, adapt to traction forces. Additionally, it was an estimated velocity of 1 $\mu\text{m}/\text{min}$ for MDCK cells migrating in μFSA .

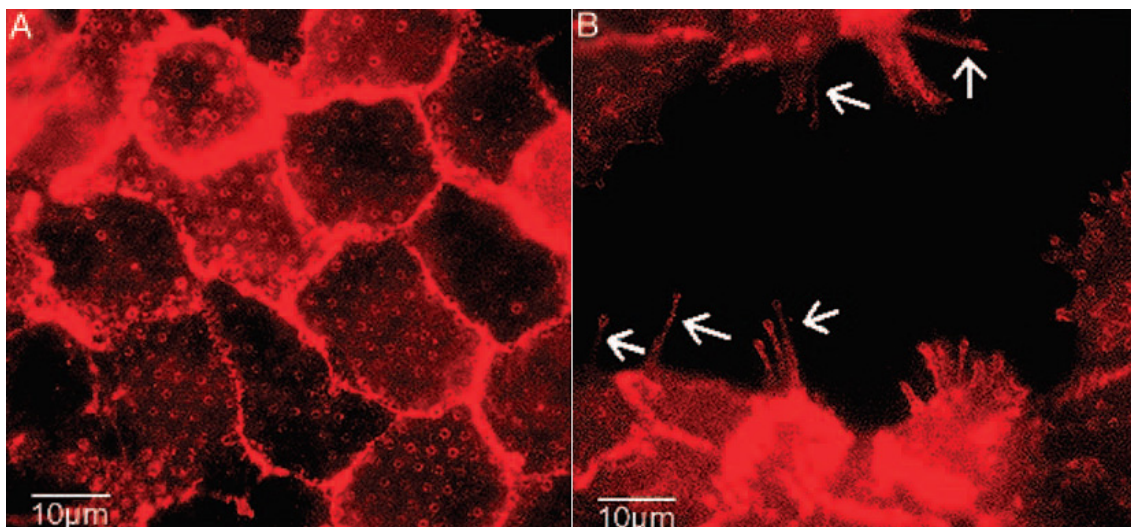


Figure 2.20. MDCK cells in μFSA . (A) HGF absence (B) HGF treated, white arrows shows generated actin protrusions [26].

Van Hoorn [29] studied how the focal adhesions deform to cause enough activity to initiate mechanotransduction during force exertion. He proposed an upside-down configuration of micropillar arrays; in this configuration, it was needed a spacer of 50 μm to avoid cells being squeezed by the device, as seen in [Figure 2.21](#). Additionally, this study proves that cells behave identically in this configuration as they were in the typical upright set up.

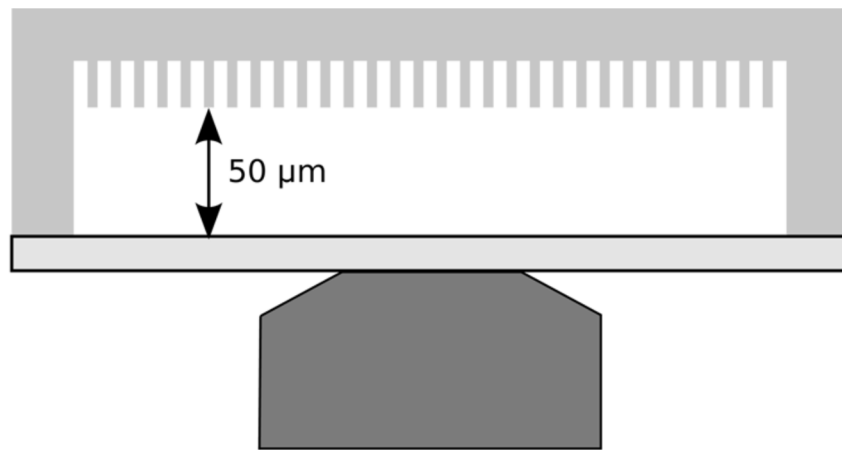


Figure 2.21. Upside-down micropillar configuration [29].

For measurements, the top of the micropillars was coated with fluorescent-labelled fibronectin to detect pillar deflection. Simultaneously, focal adhesions were detected by using an antibody that specifically targets phosphorylated paxillin. Phosphorylated paxillin is a common protein available within the focal adhesion and it was found a linear relationship in the orientation between focal adhesion and generated forces within a standard deviation of 10° , as seen in Figure 2.22. For both 3T3 fibroblasts and epithelial MCF-7 cells, the focal adhesion elongation was in the range of 100-280 nm. This study gives an insight into the role of focal adhesions in mechanotransduction. [29]

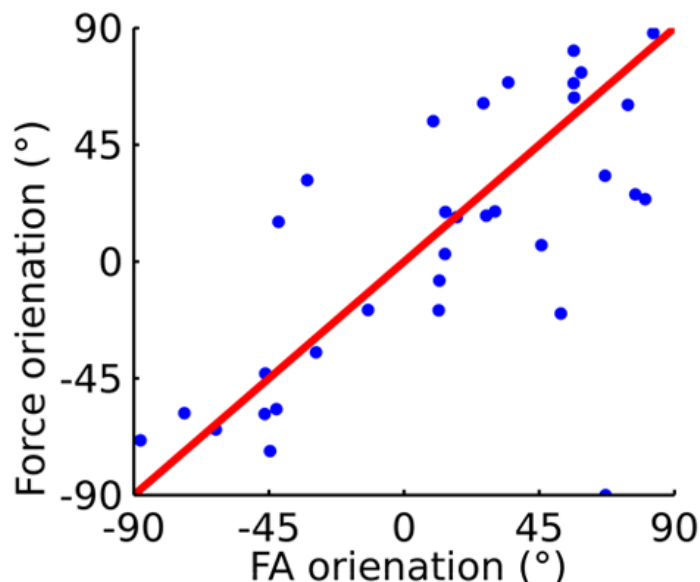


Figure 2.22. Force orientation vs Focal adhesion direction plot [29].

Furthermore, an important contribution to the understanding of force-rigidity relationship was found by Ghibaudo [30] and Saez [31, 37]. In order to study more in

depth this relationship, Ghibaudo[30] seeded 3T3 fibroblasts and epithelial MDCK cells in micropillar arrays with stiffness varying from 1 to 200 nN/ μ m. Results are presented in Figure 2.23.

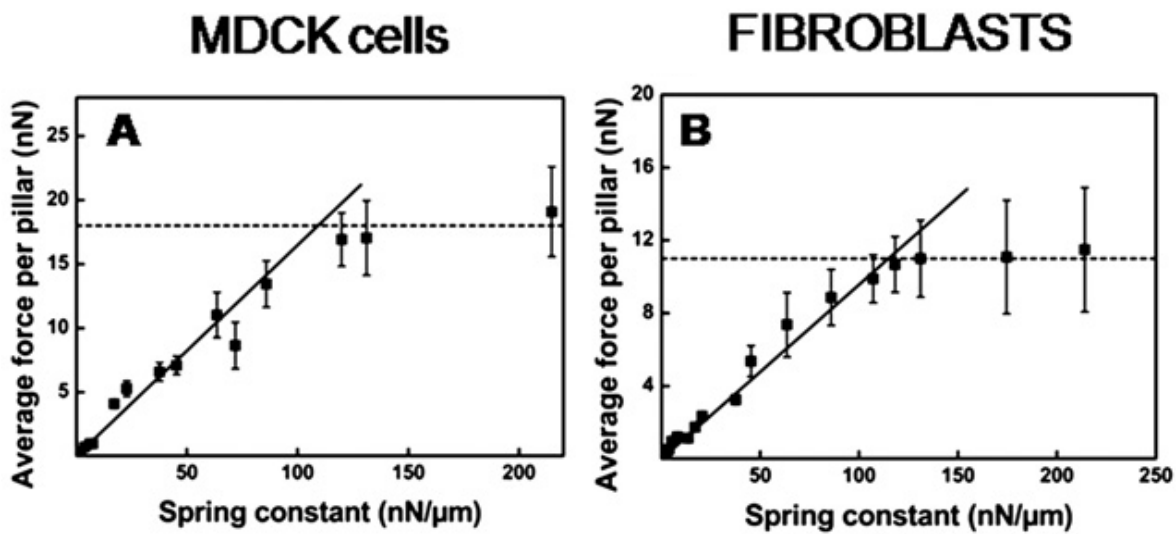


Figure 2.23. Cell average force vs stiffness (A) MDCK (B) 3T3 cell lines [30].

These forces are directly proportional to the stiffness for both cell lines until it reaches a plateau of 18 nN at for MDCK epithelial cells and 11 nN for 3T3 fibroblasts at 130 nN/ μ m micropillar spring constant. This linear relationship gave a constant pillar deflection of 100 nm for 3T3 fibroblasts and 160 nm for MDCK epithelial cells which is in mutual agreement with Saez [31, 37]. Additionally, cells were seeded in elliptical micropillars, 1 μ m minor axis and 2 μ m major axis, it was seen that cells migrated in the direction of increasing stiffness. Apart from the fact that this study corroborates that forces increase according to substrate stiffness, it shows that this increment reaches a plateau depending on the cell line at a certain stiffness [30, 31, 37].

The influence of substrate rigidity in cell morphology, focal adhesions, cytoskeletal contraction and stem cell differentiation was investigated by Fu [32]. Human mesenchymal stem cells (hMSCs) and human umbilical vascular endothelial cells (HUVECs) were cultivated in micropillar arrays of increasing stiffness ranging from 6.1 to 12.9 nN/ μ m. Overall, cells lying in stiffer substrates spread well with bigger focal adhesions and bigger forces than the softer ones. To analyse the effect of rigidity on cell differentiation, cells were exposed to normal growth medium or a differentiation medium. Cells in the differentiation medium exhibit a higher level of differentiation in the stiffer micropillar arrays than the soft ones. Cells that did not differentiate, the ones

in the normal growth medium, remain contractile regarding the micro-posts stiffness [32].

In addition, Jasaitis [34] studied the effect of cadherins receptors in cell mechanotransduction. Cadherins are the main mediating receptors in cell-to-cell junctions when cells are in contact and they interact with the cytoskeleton to transmit forces through the cell. Equivalently, integrins are the main receptors between focal adhesions and the ECM protein interacting with the cytoskeleton to produce forces against external cues. To study this effect, Murine Sarcoma cancer cell line (S180) cells were seeded in micropillar arrays to measure forces of isolated cells (without cadherins receptors) versus a cluster of cells (with the presence of cadherins). These clusters expressed three types of cadherins: Cad7, E-cad from epithelial tissue and N-cad from neurons. Results are presented in [Figure 2.24](#).

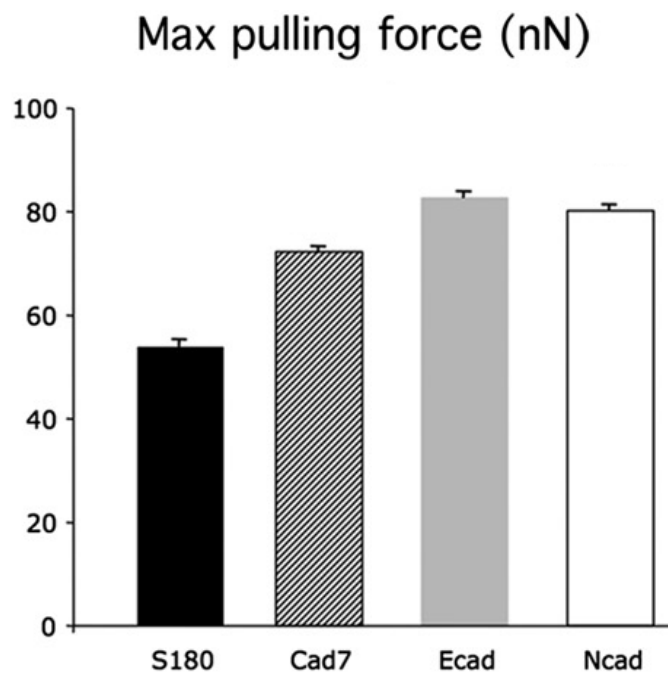


Figure 2.24. Maximum pulling force of S180 (isolated) and S180 cells expressing Cad7, E-cad and N-cad [34].

Isolated S180 cells exerted a mean maximum pulling force of 58 nN while islands of cells expressing Cad7, E-cad and N-cad generated 75 nN, 83 nN and 78 nN respectively. These results prove that the presence of cadherins receptors increases the generated forces at focal adhesions [34].

The study carried out by Ganz [39] studied N-cadherin junctions to see if they can induce mechanical stresses. For this study C2 mouse myogenic and GT1-7 cell lines

were cultivated in μ FSA coated with N-cad Fc chimaera proteins. This layer of N-cad Fc chimaera interacts with the N-cadherin from living cells and it stimulates the cell-cell adhesion process. Furthermore, cells were grown on fibronectin-coated micropillars as a control measure. Results showed that both cell lines spread and exert forces on N-cad coated micropillar arrays. On the other hand, both cell lines exerted twice the force in fibronectin than N-cad fc coated array. Interestingly, C2 cells tend to sink in one area instead of migrating along the device, this was seen only in N-cad fc coated arrays and it suggests that this is a specific response of C2 cells against N-cad Fc protein. It was demonstrated that N-cadherin junctions can induce forces in the ECM protein likewise integrins do.

Tan [36] studied the relationship between generated forces and focal adhesion size for Bovine pulmonary artery smooth muscle cells (BPASMCs). Results are presented in [Figure 2.25](#) and it was seen that an increase in focal adhesion size will generally increase the forces that are exerted on the arrays. However, this relationship was not followed when the focal adhesions were smaller than $1 \mu\text{m}^2$ where bigger forces were generated.

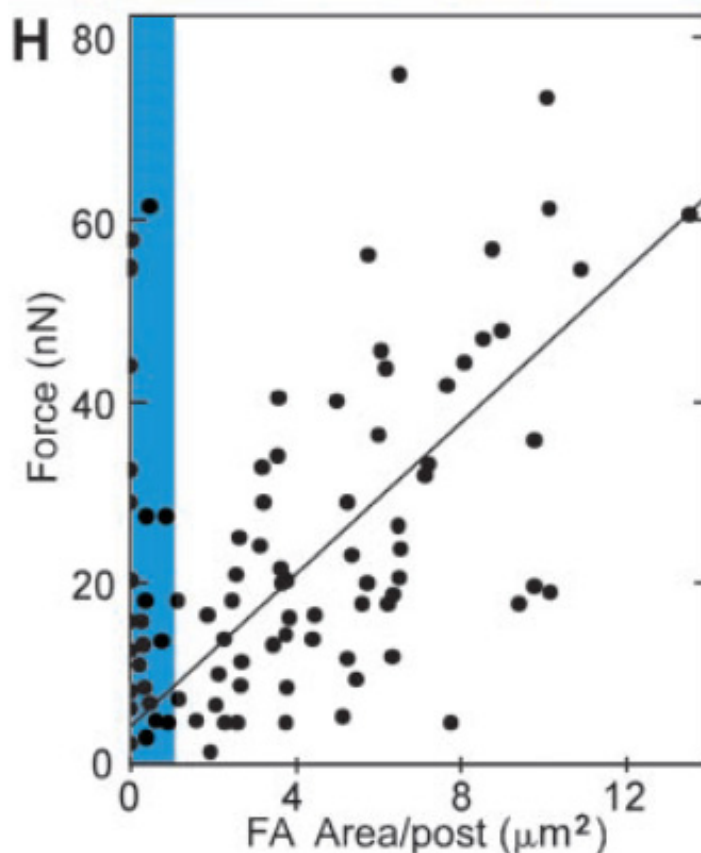


Figure 2.25. Force versus focal adhesion area for BPASMCs cells. Blue area corresponds to focal adhesions smaller than $1 \mu\text{m}^2$ [36].

These findings suggest that forces generated in focal adhesions that are smaller than $1 \mu\text{m}^2$ might be residues of previous focal adhesions. Notably, these two force-size regimes can coexist within the same cell. According to the author, the cause of having these big forces in focal adhesions smaller than $1 \mu\text{m}^2$ remains unclear; nonetheless, this author suggested that it may be because of previous well defined focal adhesions [36].

Another study regarding forces and focal adhesions was presented by Balaban [38], in this paper human dermal fibroblasts were seeded in micropillar arrays and results are illustrated in Figure 2.26.

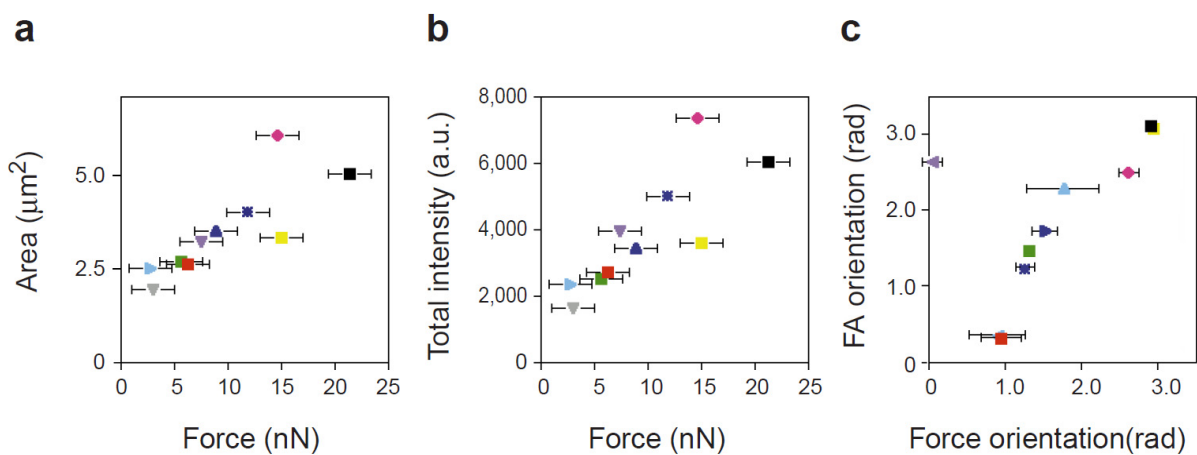


Figure 2.26. Human dermal fibroblasts (HDF) graphs. (a) Focal adhesion area against generated forces (b) relationship between focal adhesion fluorescence intensity and force (c) focal adhesion orientation versus force orientation [38].

As seen in Figure 2.26(a)-(b), the area and total intensity of focal adhesions have a linear relationship with the applied forces. This finding suggests that constant stress of $5.5 \pm 2 \text{ nN}/\mu\text{m}^2$ is applied to each focal adhesion point and in conclusion, the forces are strongly associated with the assembly of the adhesion sites. Additionally, in Figure 2.26(c) it was confirmed Van Hoorn[29] finding that force and focal adhesion orientation were in the same direction [38].

2.2.1 Micro force-sensing arrays for macro-organisms

Another application for μFSA is presented by Khare et al [50], where migration of macro-organisms are studied. In this paper, the migration forces of two-worm type's organisms were analysed (*Caenorhabditis elegans* and *Drosophila melanogaster*). This device consists of a pillar array with hexagonal arrangement with $50 \mu\text{m}$ diameter

and spaced by 70 μm . These pillars were coloured with an orange dye to help make a contrast between pillars, the clear PDMS base and the organism as seen in [Figure 2.27](#) [50].

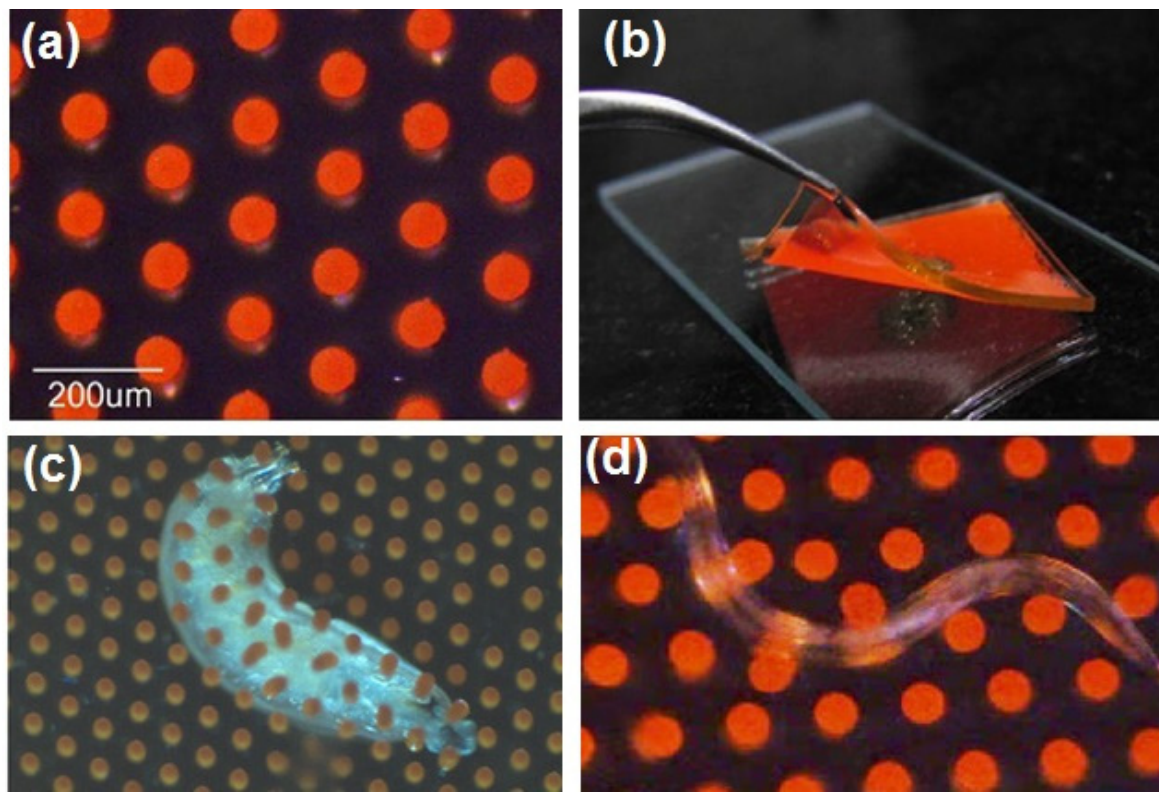


Figure 2.27. Coloured micropillar array [50]. (a) Coloured micropillars under the microscope (b) macroscale image (c) *Drosophila melanogaster* (d) *Caenorhabditis elegans*.

This device can give the following parameters: body length, body diameter, total average force, individual forces on each pillar. Results show that “*Caenorhabditis elegans*” exerts a total average force of 7.68 μN where the movement was aggressive in the first 30 seconds and then the organism started to resume their normal locomotion speed. On the other hand, *Drosophila melanogaster* exert a total average force of 1.58 μN , it starts to crawl slowly and after 45 seconds it reaches its normal locomotion speed. [50]

2.3 Summary

Cell migration is involved in essential processes such as wound healing, scaffold colonization and metastasis. This led cancer researcher studies to focus on the understanding of the mechanisms of cell migration during metastasis. Therefore, the study of cell mechanotransduction could give insights into how metastasis could be controlled before it spreads through the body which could lead to the development of

treatments to fight cancer. Current techniques to study mechanotransduction are expensive and complex; consequently, there is the urge to develop a device which is cheap, simple and easy to fabricate that can be used or implemented in a basic lab. The accuracy of these techniques relies on using non-contact methods to eliminate external loads that may influence cell migration behaviour. Previous researchers focused on the study of local forces rather than net forces because the variation of local forces on each focal adhesion is not fully understood in terms of force strength, direction, and speed.

Based on the literature review from this chapter, it was decided to use micro force sensing arrays to study cell mechanotransduction due to its great fabrication repeatability, good force measurement resolution, simple design and ability to accurately measure local forces. These devices can also be used to study focal adhesions, cell morphology, cell capturing techniques and to study macro-organisms such as worms. These devices consist of micropillar arrays made of PDMS that deflect when the cell attach their focal adhesion points to them. These deflections are recorded with a camera and used to calculate useful information such as force strength, direction and speed. Previous micropillar's studies gave insights of how cell mechanotransduction functions; however, this is not fully understood and therefore, this thesis will develop a device to fulfil our aim to provide an efficient device to study cell migration. These insights were that substrate topography and stiffness influences the cell behaviour during its migration where pillar diameter and spacing from devices of previous researchers, served as a rough guide to select our micropillar dimensions. These dimensions were in the 2-5 μm range and consequently, dimensions for this project are selected within this range.

Furthermore, previous studies addressed the requirement to coat micropillar tips with an ECM protein in order to create an optimal attachment of cell focal adhesion to the tip of the micropillars. The microcontact printing technique is often used to coat micropillars with an ECM protein. Therefore, this thesis studies this technique and explore other methods for assessing their reliability.

Chapter 3. Device fabrication

3.1 Introduction

This chapter includes the fabrication of the micropillar devices which were done in the Nanoscience lab facilities of Bedson building of Newcastle University. Micropillar arrays were fabricated by casting and demoulding them from silicon wafers moulds, these moulds have the dimensions of our micropillars. A single wafer master was fabricated with rows of moulds with different micropillar arrangements and dimensions. Moulds were diced into chips of 10 x 10 mm to facilitate handling, storage. Once a chip was removed from the silicon master, it was glued into a 30 mm petri dish. Each silicon chip can be reused multiple times, during this project each silicon chip started to build up some PDMS residues inside the silicon mould, causing the devices to have missing pillars. Silicon moulds remained functional until 40 times of use when around 15% of pillars were missing. Occasionally, these PDMS residues were extremely difficult to remove chemically or physically due to the microscopic dimensions of our patterns and therefore these silicon chips were replaced.

There are two crucial dimensions when fabricating these devices; the former is the pillar radius which must be small enough to accommodate just one focal adhesion but big enough to successfully contain all the contact area of the individual focal adhesion. The latter is the space between pillars; it should be small enough to avoid anchoring of the cell between pillars [21, 25]. The finite element analysis (FEA) was carried out for one single micropillar to ensure that theoretical assumptions are appropriate. Once the FEA was finished, a range of micropillar arrangements for the silicon moulds was proposed and fabricated.

3.2 Materials and methods

This section describes the methods used to fabricate PDMS micropillar devices, all reagents were purchased from Sigma-Aldrich (UK) unless otherwise is stated.

3.2.1 Finite element analysis

Modelling and finite element analysis (FEA) were performed using the ANSYS APDL software version 15.0 available at the mechanical school in Stephenson Building. Modelling for the FEA analysis was done to a single pillar because each pillar deflection is independent of each other. A total of three FEA analysis were carried out using three different cross-sectional areas on each analysis; two circulars with 2 and 3- μm

diameter and one elliptical with a minor axis of 2 μm and a major axis of 3 μm , these cross-sectional areas are shown in Figure 3.1. The micropillar length for all the FEA analysis was set to 5 μm . Furthermore, it was added a circular base of 3 μm and 1 μm thickness to emulate the surrounding area.

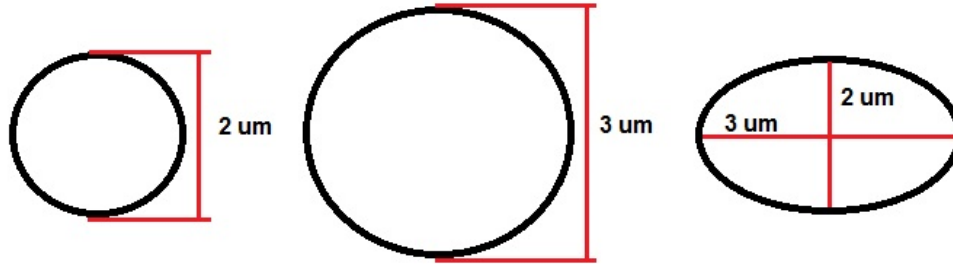


Figure 3.1. Cross-sectional areas of proposed micropillars. Two circulars with 2 μm and 3 μm respectively and one elliptical with a major axis of 3 μm and a minor axis of 2 μm .

The material for the base and pillar is PDMS and their properties were set to 2 MPa young's modulus, a density 965 kg/m^3 and 0.49 Poisson ratio. Element type was BEAM 189 because each pillar behaves as a beam. Each node of this element type has 6 degrees of freedom namely x, y and z translations and rotational in x, y and z-axis. Part of the modelling includes positioning the applied force which was chosen to be a constant force of 1 nN in a node in the centre of the pillar tip. Furthermore, the base of our model was constrained in every degree of freedom as it is assumed that the base is a rigid and static element. These FEA analyses were compared with a theoretical calculation to ascertain that our assumptions were correct.

For the theoretical calculations, the Euler Bernoulli beam theory previously denoted in Eq. 3 from 2.2, has been used to calculate forces in micropillar arrays by previous researchers [25-27, 29-32, 34-38, 44, 45] even though it does not take into account the effect of shear stresses.

$$F = k \cdot x = \left(\frac{3}{4} \cdot \pi \cdot E \cdot \frac{r^4}{L^3} \right) \cdot x \quad \text{Eq. 3}$$

However, the selected element type for the FEA is BEAM 189 which is based in the Timoshenko beam theory rather than the Euler Bernoulli beam theory. The Timoshenko beam theory includes shear deformation effects, and this might lead to having discrepancies between the FEA and theoretical assumptions. Consequently,

the equation proposed by Schoen [51] is used for the theoretical calculations, see Eq. 4 and Figure 3.2. This equation calculates the deflection (x) caused by bend and shear stresses in a beam. Euler Bernoulli equation (Eq. 3) and Schoen equation (Eq. 4) were compared against the FEA analysis to ascertain which equation is more appropriate and therefore used for our data analysis.

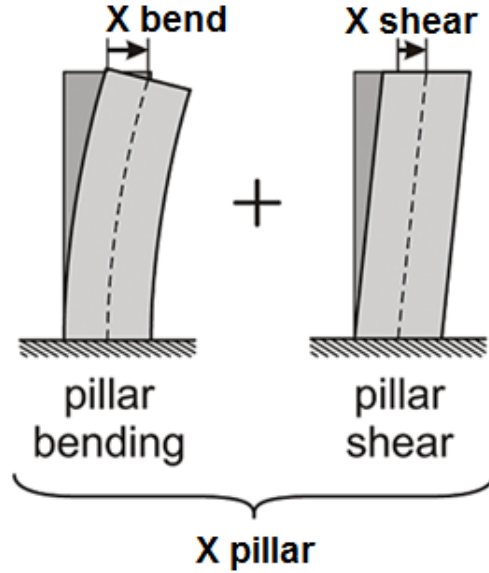


Figure 3.2. Illustration of bending and shear stress on the micropillars according to Schoen [51].

$$X_{pillar} = X_{bend} + X_{shear} = (k_{bend}^{-1} + k_{shear}^{-1}) \cdot F$$

With,

$$k_{bend} = \frac{3 \cdot E \cdot I}{L^3} ; k_{shear} = \frac{K \cdot G \cdot A}{L}$$

$$I = \frac{\pi \cdot D^4}{64} ; G = \frac{E}{2 \cdot (1 + \nu)} ; K = \frac{6(1 + \nu)}{(7 + 6 \cdot \nu)} ; A = \frac{\pi \cdot D^2}{4}$$

Then:

$$X_{pillar} = \left(\frac{16}{3} \left(\frac{L}{D} \right)^3 + \frac{7+6 \cdot \nu}{3} \left(\frac{L}{D} \right) \right) * \left(\frac{4 \cdot F}{\pi \cdot E \cdot D} \right) \text{ Eq. 4}$$

Where “ I ” is the second moment of inertia, “ ν ” is the Poisson ratio, “ G ” is the shear modulus, “ K ” is the Timoshenko’s shear coefficient and “ A ” is the cross-sectional area.

On the other hand, this equation does not work for micropillars with elliptical cross-sectional areas since the stiffness varies depending on the movement orientation.

From the linear elastic theory, we obtain a deflection equation for elliptical cross-sectional areas, see Eq. 5 [30].

$$F = K \cdot (\theta) \cdot \partial \bar{u} = \frac{3}{4} \cdot \pi \cdot E \frac{a \cdot b}{L^3(a^2 \cdot \cos^2 \theta + b^2 \cdot \sin^2 \theta) \cdot \delta \bar{u}} \quad \text{Eq. 5}$$

Where “K (θ)” is the spring constant, “∂u” is the displacement, “E” is the young modulus, “a” is the major axis, “b” the minor axis, “L” is the pillar length and “θ” is the bending direction. For FEA purpose, the bending direction in the elliptical pillar is in the direction of the major axis. For future calculations, the angle “θ” will be calculated with the data obtained from the MATLAB code. Results from FEA and theoretical calculations are presented in Table 3.1 and Figure 3.3 shows the FEA for the 3 μm diameter and 5-μm length micropillar design.

Table 3.1. FEA results and its approximation to Euler and Schoen equation.

Design		Displacement			Error.
		FEA	Euler	Schoen	
Circular	D= 2 μm	2.936 x10 ⁻⁸ m	2.653 x10 ⁻⁸ m	2.916 x10 ⁻⁸ m	0.68%
	D= 3 μm	6.525 x10 ⁻⁹ m	5.240 x10 ⁻⁹ m	6.412 x10 ⁻⁹ m	1.77%
Elliptical	Major = 3 μm Minor = 2 μm	1.710 x10 ⁻⁸ m	1.768 x10 ⁻⁸ m	-	3.30%

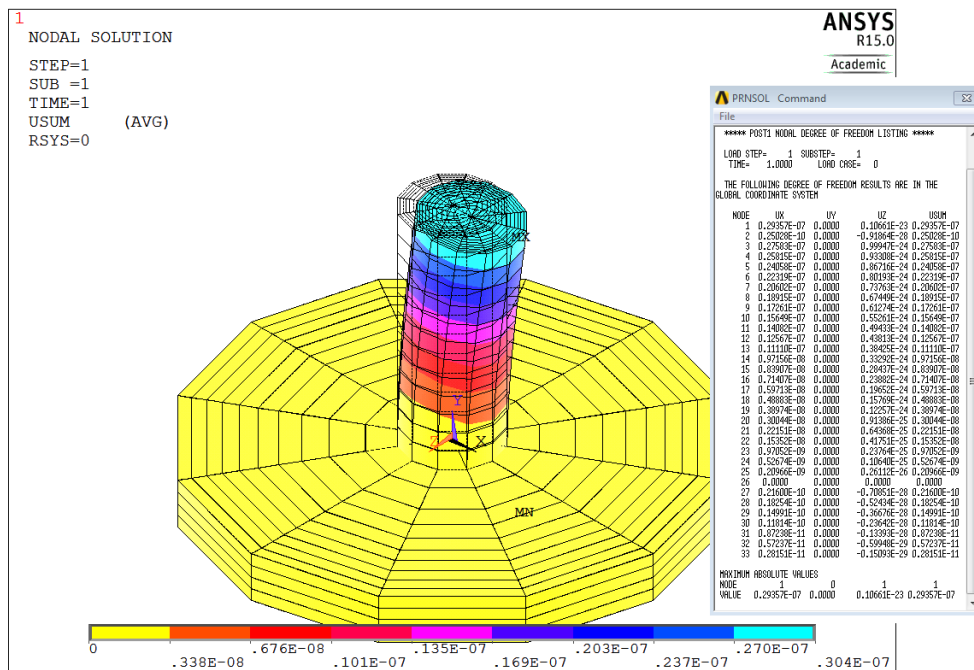


Figure 3.3. Micropillar finite element analysis. D=2 μm L= 5 μm.

The theoretical and FEA results were satisfactory with an error of less than 1% for the 2 μm diameter pillar, 1.77% error for the 3- μm diameter pillar and 3.30% error for the elliptical one. Consequently, both Eq. 4 and Eq. 5 were used to calculate the micropillar stiffness for micropillars with circular and elliptical cross-sectional areas respectively as the low error percentage demonstrates that the Schoen equation gives a more realistic approximation than Euler equation. The calculated stiffness was 155.969 nN/ μm for the 3 μm circular pillar, 34.291 nN/ μm for the 2 μm circular pillar and 56.549 nN/ μm for the elliptical micropillar.

3.2.2 Designing micropillar arrangements

From the micropillar literature review from Table 2.2, micropillar diameters from these studies range from 2-5 μm and micropillar arrangement of rows and columns with equal spacing. Based on these values it was chosen three types of cross-sectional areas, previously shown in Figure 3.1. These are two circular sections with diameters of 2 μm and 3 μm and one elliptical with a major axis of 3 μm and a minor axis of 2 μm . To choose the micropillar arrangement and spacing.

A total of 11 designs were which are named from 1 to 11 as illustrated in Figure 3.4, Figure 3.5, Figure 3.6, Figure 3.7, and Figure 3.8. Dimensions for design #1 was chosen to be 2 μm pillar diameter and 4 μm micropillar distance centre to centre as shown in Figure 3.4 (1).

The appropriate spacing between pillars for the remainder designs was calculated using Eq. 1 and Eq. 2 from section 2.1.2 so they maintain the same ECM protein percentage than design #1. Exceptions made for designs 4, 7, 8 and 9 which did not have the same percentage of ECM protein than design #1.

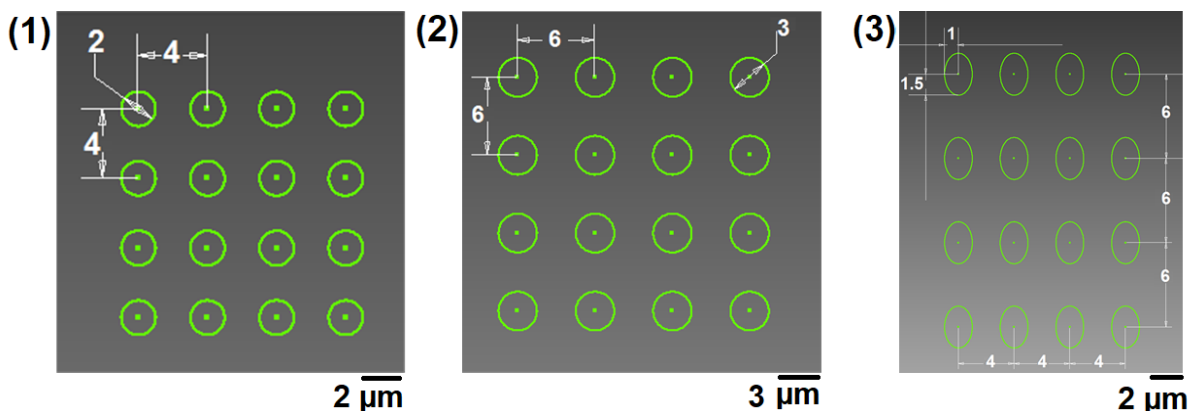


Figure 3.4. Computer-aided designs (CAD) of silicon wafer designs 1, 2 and 3.

Three templates for the designs 1,2 and 3 are presented in [Figure 3.4](#). The micropillar dimensions for design 2 correspond to the second cross-sectional area which has 3 μm diameter. Micropillars in design 1 has a diameter of 2 μm and a 4 μm centre to centre distance, this means that the micropillar spacing (S_1) for design 1 is 2 μm . The micropillar spacing was calculated using [Eq. 2](#).

$$\%ECM_1 = \%ECM_2$$

$$\frac{\pi \cdot r_1^2}{(2 \cdot r_1 + S_1)^2} = \frac{\pi \cdot r_2^2}{(2 \cdot r_2 + S_2)^2}$$

By replacing the values of $S_1= 2 \mu\text{m}$, $r_1= 1 \mu\text{m}$ and $r_2= 1.5 \mu\text{m}$, it is obtained an S_2 of 3 μm that corresponds to a distance centre to centre of 6 μm as shown in [Figure 3.4 \(2\)](#).

The third cross-sectional area from [Figure 3.1](#) was used for design #3 which corresponds to an elliptical area. Therefore, for micropillar spacing calculation [Eq. 1](#) was adapted for elliptical features as shown in [Eq. 6](#).

$$\%ECM = \frac{\pi \cdot a \cdot b}{(2 \cdot a + S)(2 \cdot b + I)} \quad \text{Eq. 6}$$

Where “a” is the minor axis, “b” the major axis, “S” is the horizontal spacing and “I” is the vertical micropillar spacing. Likewise, design #2, design #3 will keep the same percentage of ECM protein than design #1. The horizontal distance “S” remained the same than design #1 and the vertical distance “I” was calculated. The calculation is as follows:

$$\frac{\pi \cdot r_1^2}{(2 \cdot r_1 + S_1)^2} = \frac{\pi \cdot a \cdot b}{(2 \cdot a + S_2)(2 \cdot b + I)}$$

Where the inputs were: “r1” equal to 1 μm , 3 μm major axis “a”, 2 μm minor axis “b” and both “S₁” and “S₃” equal to 2 μm . By replacing these values, we obtained a vertical distance “I₃” of 3 μm as shown in [Figure 3.4 \(3\)](#).

Design #4 presented in [Figure 3.5](#), was designed to have a honeycomb shape which did not have the same percentage of ECM protein than design #1. The rationale behind this design is to ascertain whether cells sink inside the honeycomb or they remain in the top of the pillars.

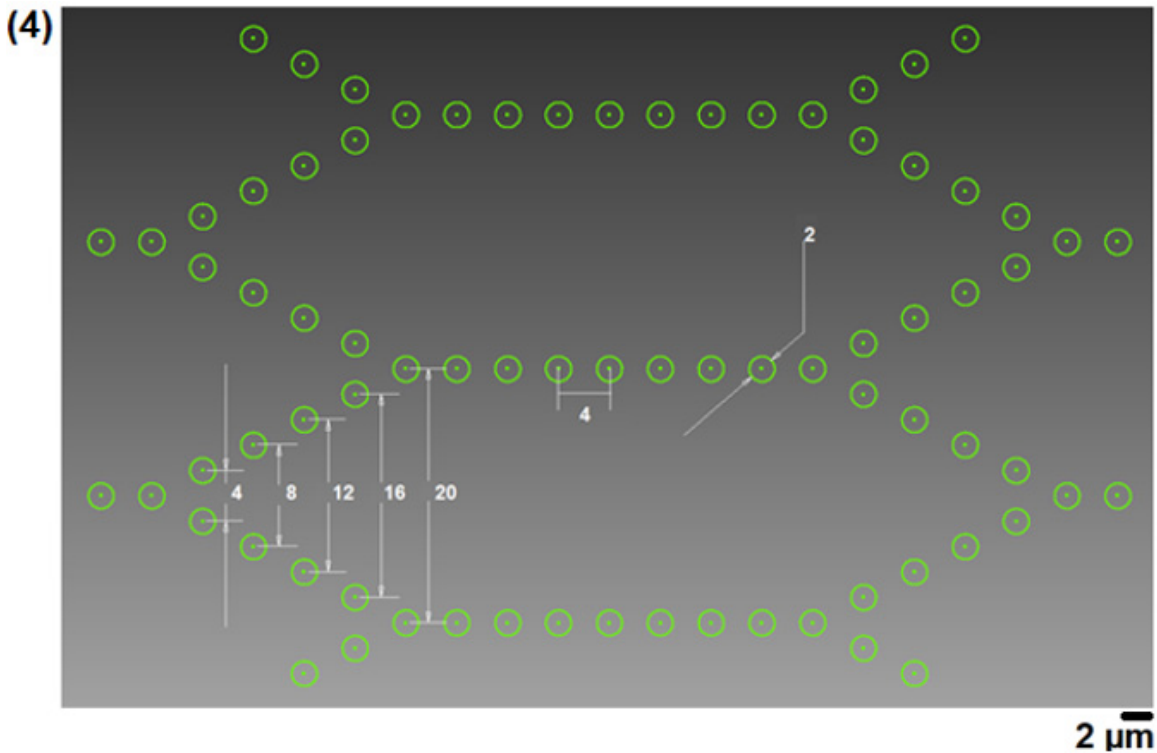


Figure 3.5. CAD image of silicon wafer design 4.

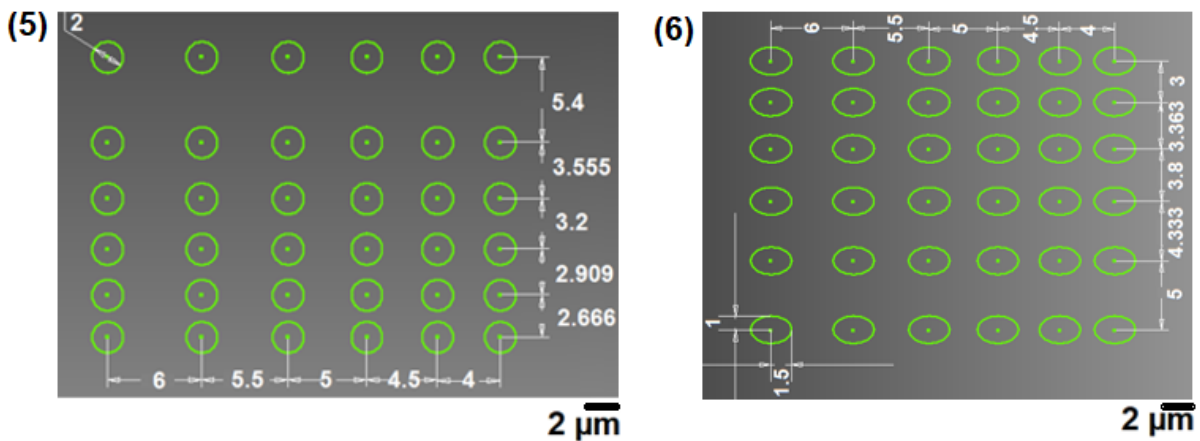


Figure 3.6. CAD images of silicon wafer designs 5 and 6.

The designs presented in Figure 3.6, were intended to verify the limitations of fabricating PDMS devices. As shown in Figure 3.6 (5) and (6), both designs have rows and column with increasing micropillar spacing leading to have areas with very narrow distances between pillars. This could lead to irreversible stiction of pillars as they bend and touch a neighbouring pillar during the PDMS demoulding from these templates. The micropillar spacing for design 5 was calculated using Eq. 1 to maintain the same percentage of ECM protein than design #1 while calculations for design #6 were done with Eq. 6.

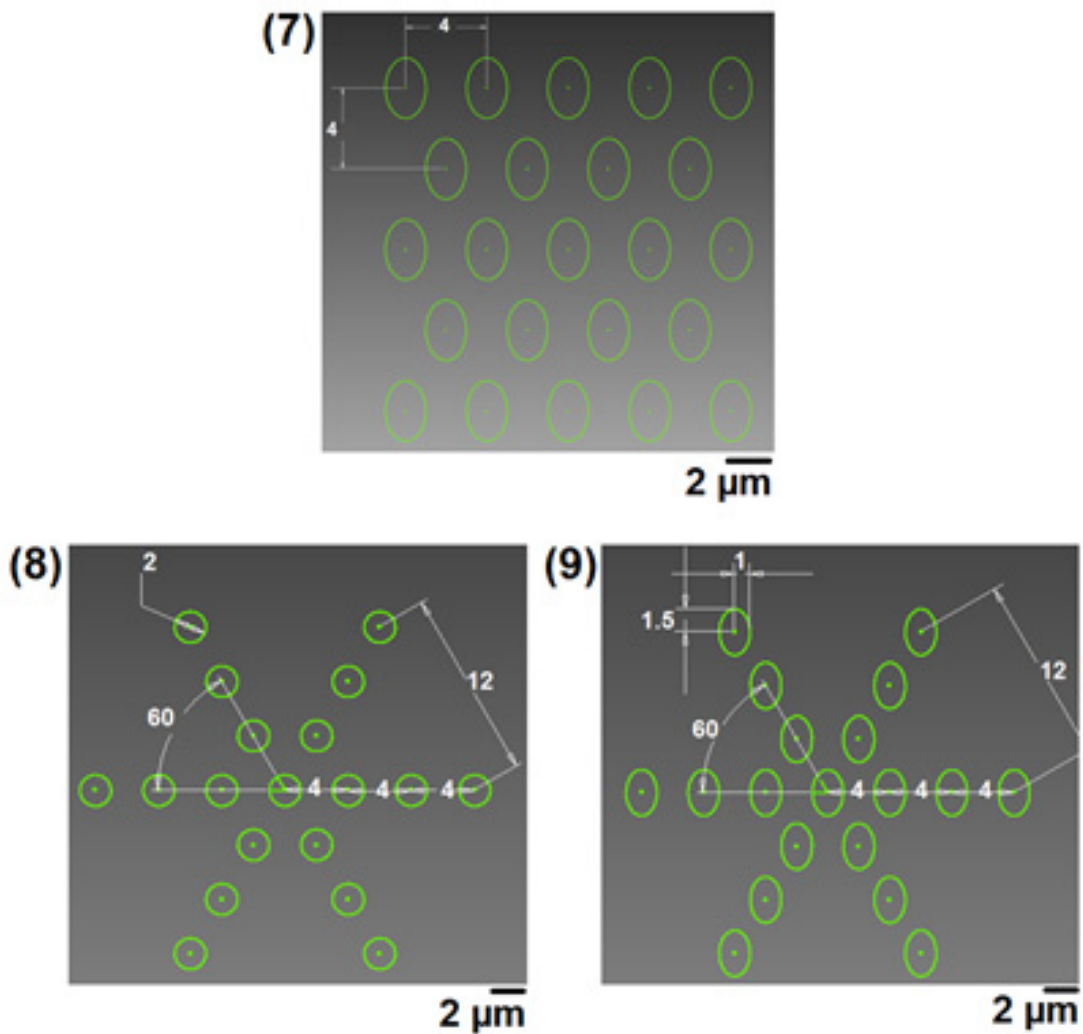


Figure 3.7. CAD images of silicon wafer designs 7, 8 and 9.

Similar to design #4, the designs presented in Figure 3.7 did not have the same percentage of ECM protein than design #1 and their pillar spacing was selected rather than calculated. Design #7 is a modified version of design #3 where the even rows were not aligned with the previous one, as seen in Figure 3.7 (7). This caused to increase the proximity of pillars between each other in elliptical micropillars with the aim to study how cells behave in this scenario. Designs 8 and 9 have a star shape intended to guide cells to the centre of this star with the aim to study how cells can be confined to a specific area.

Designs 10 and 11 from Figure 3.8, were designed to have rows equally spaced by 4 μm (centre to centre). Here, we highlight that the percentage of ECM protein in these two designs are not equal to design #1 but and they maintain the same percentage of ECM protein through them using Eq. 1 and Eq. 6. These designs were intended to confine cells within the centre of the device, similar to design 8 and 9.

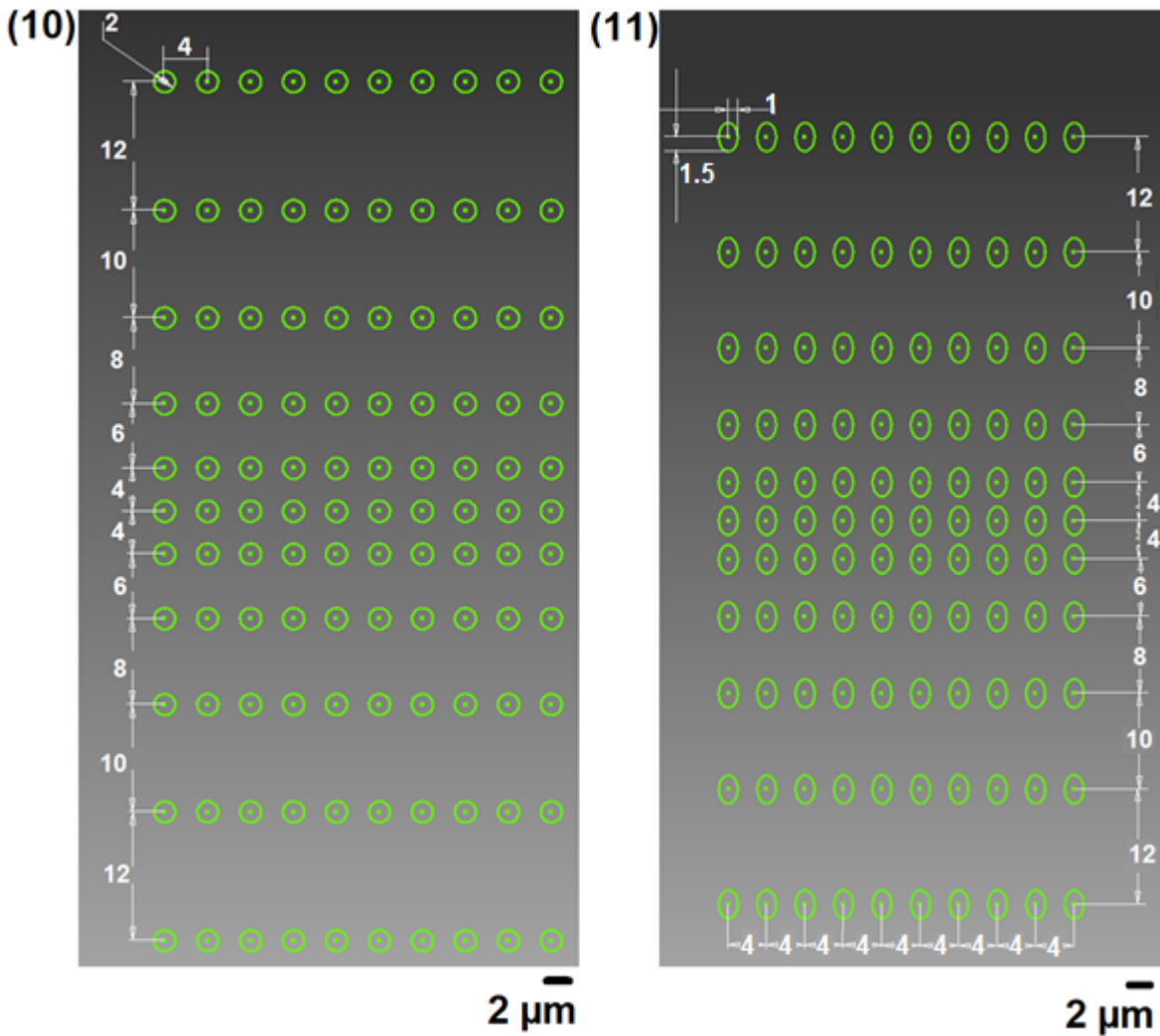


Figure 3.8. CAD images of silicon wafer designs 9 and 11.

3.2.3 Master mould fabrication

The methodology to be used to fabricate the silicon master moulds were briefly presented in Figure 2.19 (b) and will be fully explained in this section. The reason to choose this method over the methodology in Figure 2.19 (a) is that it has fewer steps to fabricate PDMS devices and that the risk to damage these masters by manipulation is low. This method fabricates silicon moulds with arrays of holes containing the 11 designed micropillar patterns where the PDMS will be poured, cured and demoulded.

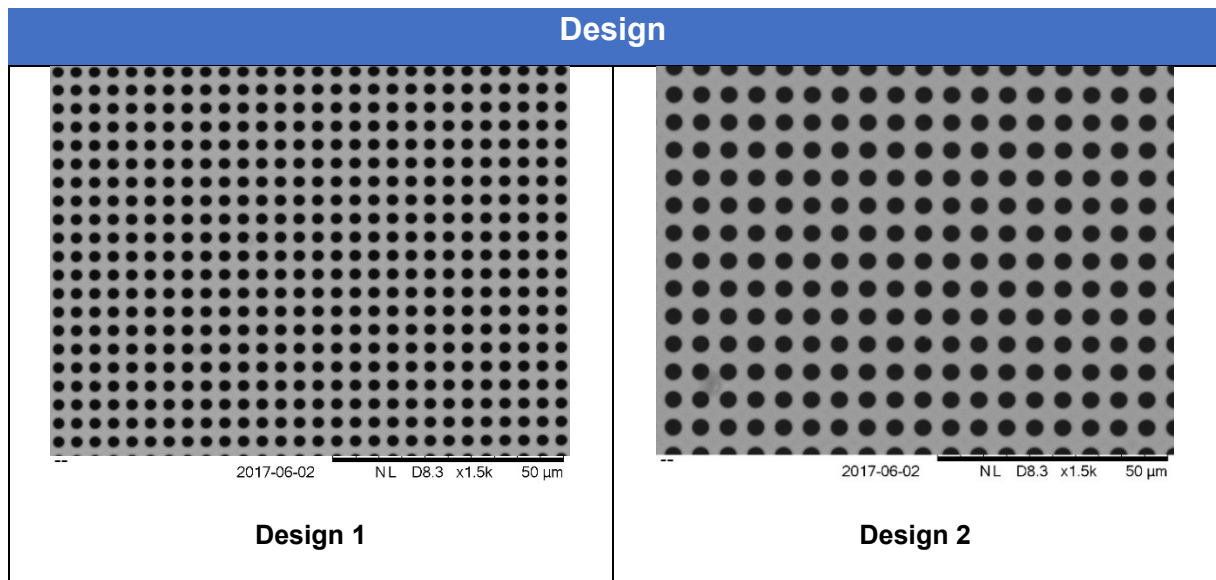
Silicon masters were fabricated by INEX, a company located in Newcastle University that requested to export the 11 CAD designs provided in section 3.2.2 to a specialised software called Tanner L-EDIT which is available in the school of engineering of Newcastle University. The methodology to fabricate these silicon masters is as follows.

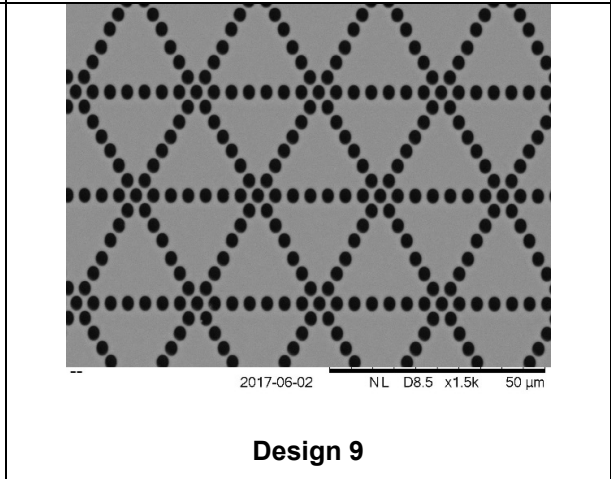
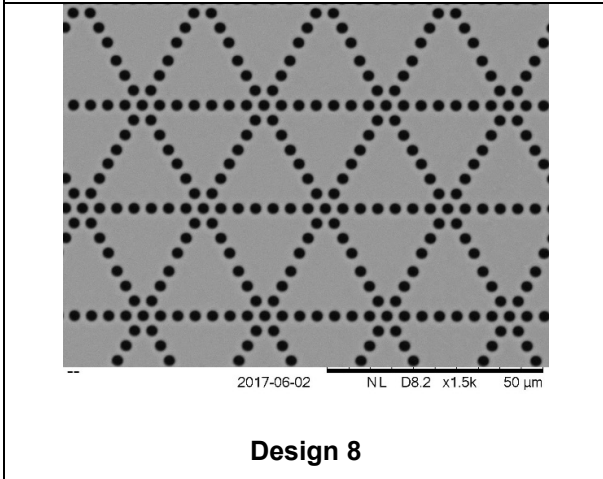
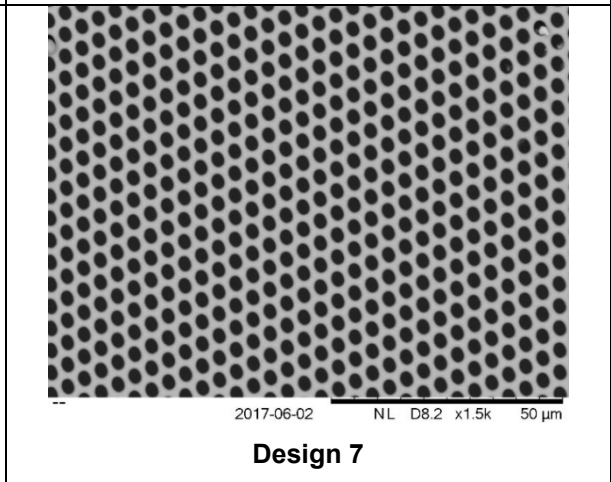
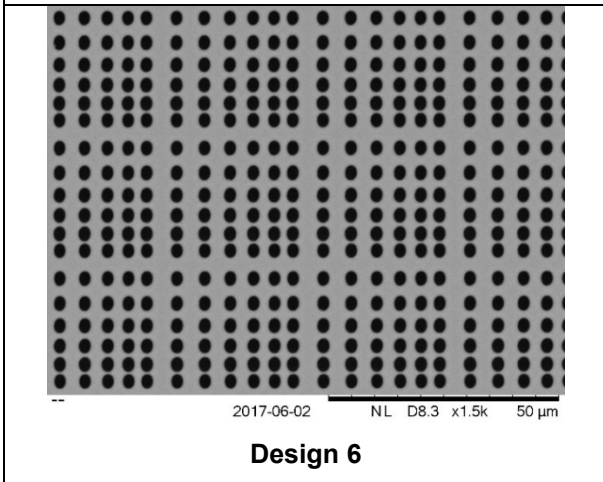
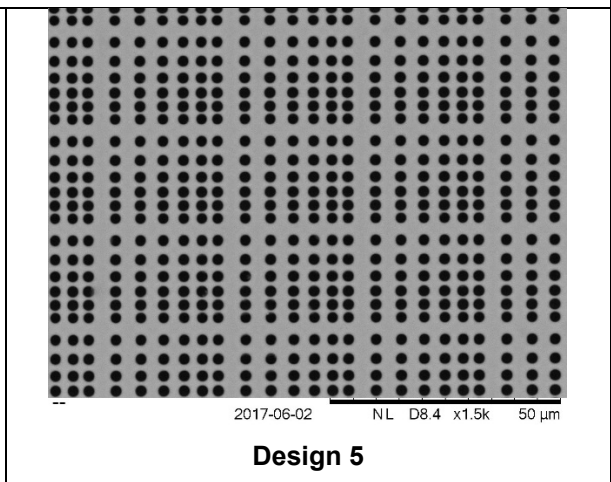
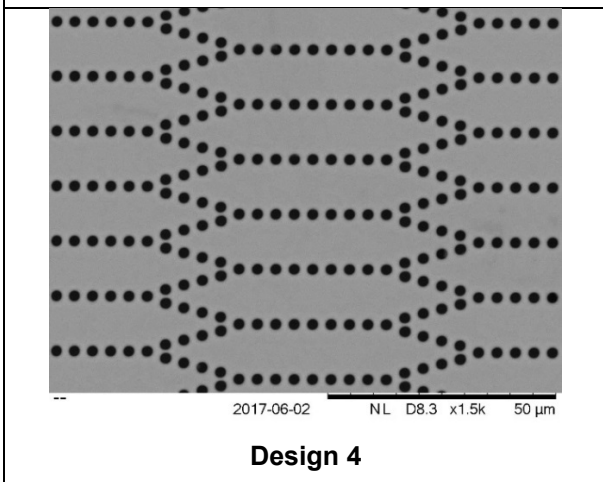
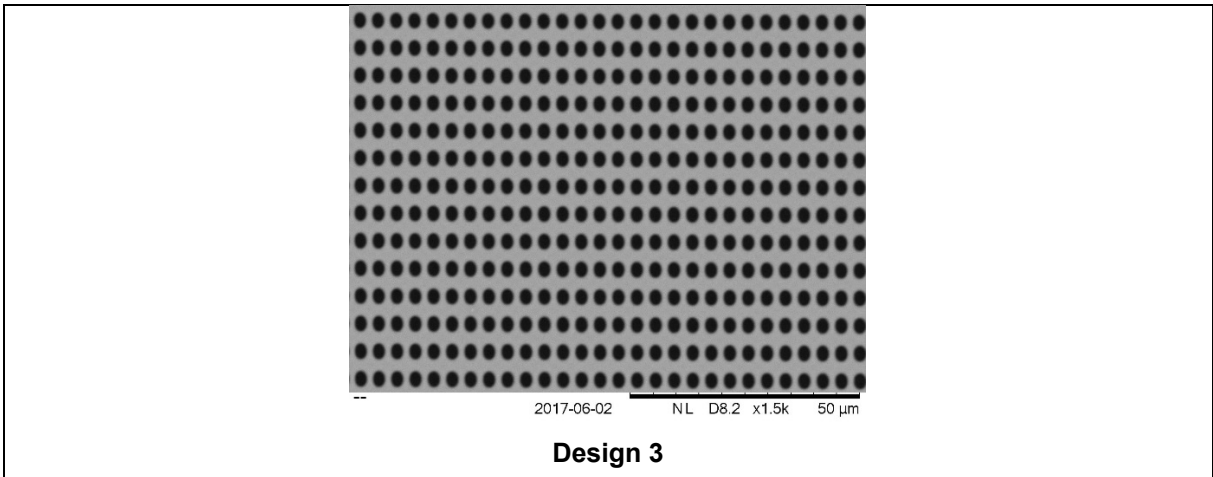
Opaque chrome masks which contained holes with the patterns of the 11 designs were fabricated. Then, the silicon wafer was cleaned with ultrasonic bath under acetone, rinsed with isopropyl alcohol (IPA) and deionised (DI) water and dried under a stream of N₂. Next, the silicon wafer was prepared for a coating with hexamethyldisilane (HMDS) by dehydration of the silicon wafer in a hot plate for 10 min at 150 °C. HMDS is an adhesion promoter for photoresists and it was applied to the silicon wafer by spin coating of 1 ml of HMDS for 30 s at 4000 RPM. Next, 5 ml of the positive AZ 5214 photoresist was spin-coated for 30 s at 4000 RPM and cured in an oven for 1 min at 100 °C. The chrome photomask was then placed on top of the photoresist and it was exposed to UV light under vacuum for 5 s. Next, the wafer was developed with AZ 400K for approximately 60 s. Wafer was then rinsed with DI water for 1 min and dried with an N₂ gun. DRIE was then applied to the exposed silicon areas with an alternate cycle of etching with octafluorocyclobutane gas (C₄F₈) for 6 s and Passivation with Sulfur hexafluoride gas (SF₆) for 4 s. The photoresist was then removed using the photoresist stripper AZ 300T for 10 min, followed by a rinse with DI water and dry with N₂ gun. Finally, moulds were diced into chips of 10 x 10 mm to facilitate handling and stored under vacuum.

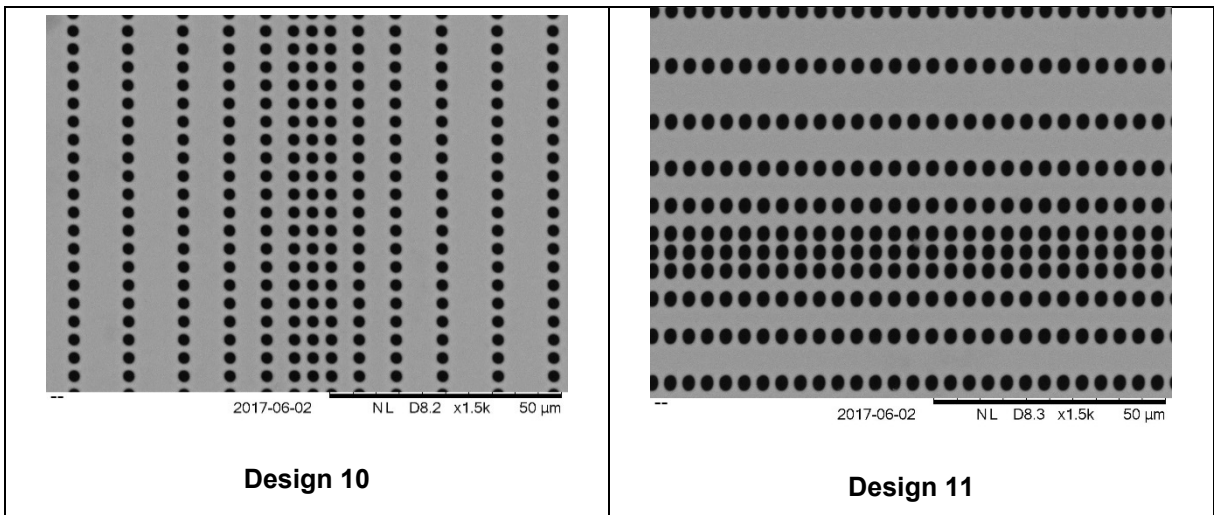
3.2.4 Silicon mould characterization

Characterisation of the micropillar arrangement was done by taking images with a scanning electron microscope from the mechanical school, these images are presented in [Table 3.2](#). It was seen that the micropillar arrangement and diameter match the provided CAD designs.

Table 3.2 SEM images of fabricated silicon master moulds.







To validate the depth of the features, silicon chips were diced, and cross-sectional images were taken with a scanning electron microscope (SEM). An SEM image of a sample with 2 µm diameter and 5 µm length is presented in [Figure 3.9](#) and it shows that this silicon chip has 4.542 µm length and a diameter of 2.248 µm.

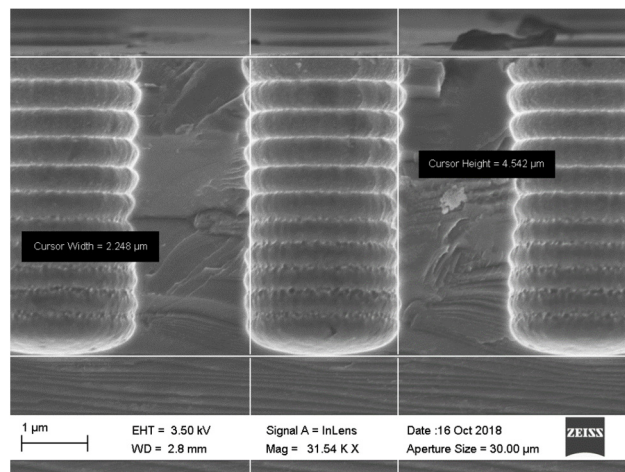


Figure 3.9 SEM image of a cross-sectional area of 5 µm depth silicon chips.

Length dimension did not match to the expected 5 µm value. SEM provides a powerful imaging tool; however, it is not accurate enough for measuring distances. To confirm this result, we performed a second characterisation using a profilometer. The ZYGO profilometer from the MEMS lab in Mertz court was used to characterise the dimensions of the features from the silicon chips. A profilometer uses a laser, a mirror and a detector providing accurate readings in the range of few nanometres. ZYGO measurements are presented in [Figure 3.10](#) and it was found that chips were 4.825 µm depth with a standard deviation of 0.105 µm and have a diameter of 2 µm with a standard deviation of 0.097 µm. These values will be used for future calculations of micropillar stiffness.

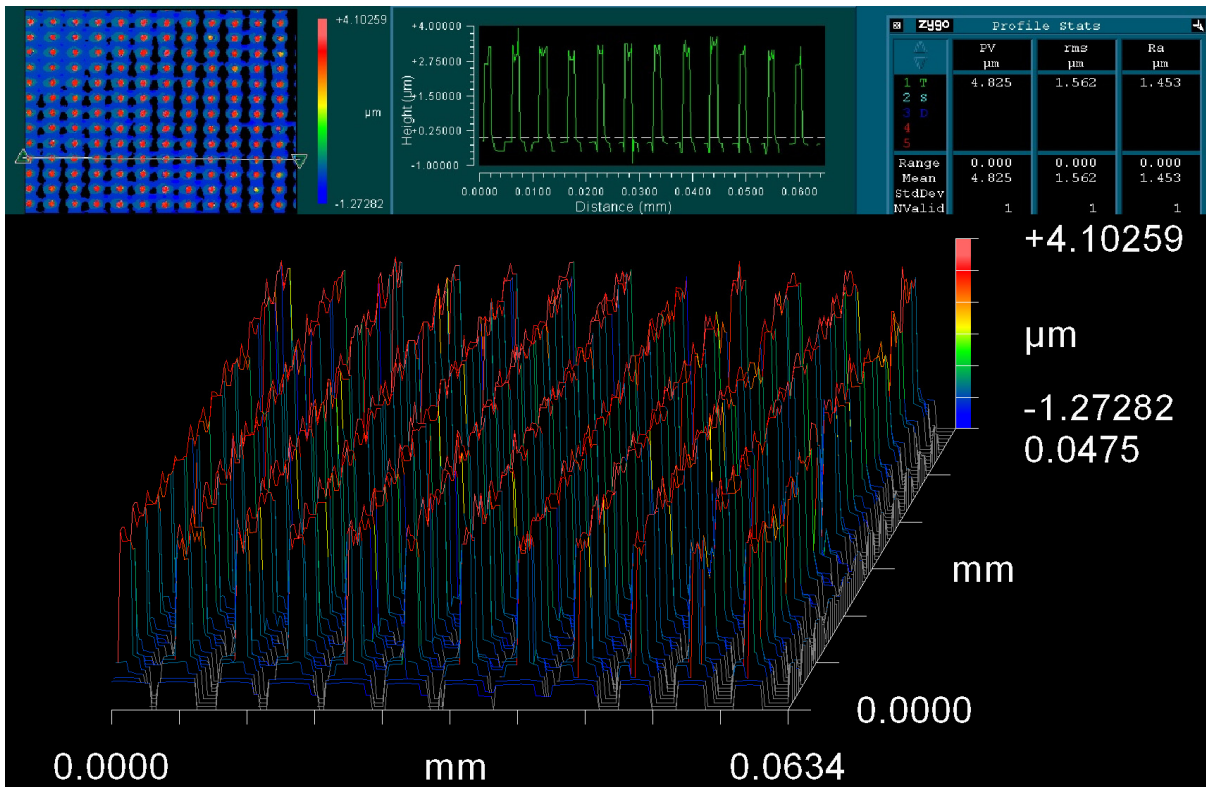


Figure 3.10. Profilometer results for 5-µm Silicon chip.

3.2.5 Silanization process

One of the major problems of working with PDMS it is the sticky natural behaviour that will lead to difficulties to do the peel off. As seen in Figure 3.11, micropillars snapped in the neck because of the stiction between PDMS pillars silicon wafer surface. Therefore, a silanization process was performed in the silicon wafers to solve this issue. This process coats the silicon surface with a hydrophobic silane and consequently, PDMS will not stick to it.

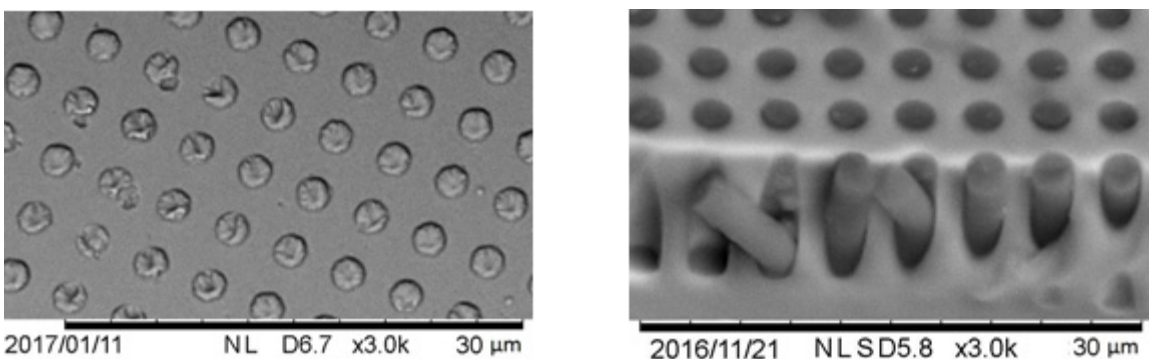


Figure 3.11. SEM images of torn PDMS pillars (left) and incrusted PDMS on the silicon wafer (right).

Silanization was performed with 1H,1H,2H,2H-Perfluorooctyl-trichlorosilane solution taking into consideration all the safety regulations provided by the manufacturer. Firstly, the silicon chips were fixed to a glass slide using carbon tape, rinsed with isopropanol and dried with N₂. In a desiccator, 40 µL of 1H,1H,2H,2H-Perfluorooctyl-trichlorosilane solution was deposited in a lens cleaning tissue. This type of tissue is lint-free so it will not leave any residues to the silicon chips. Then, house vacuum was applied for 2 min and then the inlet valve was closed. Vacuum cause evaporation of the silane solution and then, the silicon chip was incubated for 30 minutes to allow the silane to deposit on the silicon chip. Finally, air was reintroduced to the chamber by gradually opening the inlet valve. If air is introduced too quickly, the silicon chip can be thrown against the chamber and it will be destroyed. This compound is corrosive; therefore, silanization was done in a dedicated vacuum chamber in a fume hood and always wearing gloves and safety goggles.

3.2.6 Polydimethylsiloxane (PDMS) micropillar curing and demoulding.

PDMS type SYLGARD 184 from Dow Corning company, was prepared with 1:10 curing-base ratio according to manufacturer instructions to obtain a Young modulus of 2 MPa and then manually mixed and left in vacuum for 30 minutes to eliminate air trapped in the mixture. The degassed PDMS was then poured into a petri dish containing the silicon mould chip which was previously glued to it. Next, vacuum was applied again for 40 min to remove the air from inside the chips and to allow the PDMS mixture to enter inside the mould. This prolonged vacuum time ensured that all the air was removed from inside the silicon chips. PDMS was cured in an oven at 65°C for 1 hour. It is important to be careful to not overexpose the silicon wafers to heat, otherwise, the PDMS will be too stiff to be peeled off and micropillars will break.

Once the PDMS was fully cured, it was carefully peeled off from the chip using a pair of tweezers. A previous study [45], proved that micropillars with length-diameter bigger to 3 will collapse and irreversible stick with the neighbouring pillar just after peeling off. Despite having a length-diameter ratio smaller than 3, it was seen that pillars collapsed occasionally. This led to performing the peeling off step under 70% of ethanol to reduce this bouncing effect as a preventive measure. Additionally, it was seen that evaporation of ethanol caused the collapse of micropillars due to surface tension forces, as seen in [Figure 3.12](#). This collapsing was solved by either keeping the devices always wet or by performing a critical point drying step (CPD) where ethanol changes from liquid to a gas state without the direct state transition, this means that ethanol will change to

vapour with zero surface tension. Carbon dioxide (CO₂) is commonly used for CPD due to its achievable critical point of 31.1°C at 72.9 atm [52, 53].

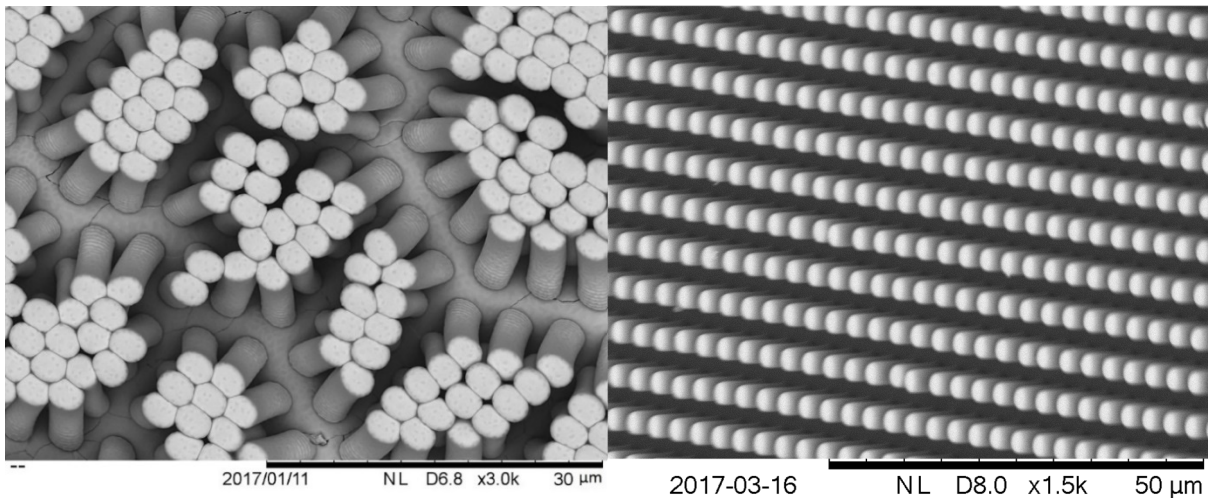


Figure 3.12 SEM image of PDMS pillars. (left) before CPD. (right) after CPD.

3.3 Results and discussion

At this stage, we have successfully developed PDMS micropillars to be functionalized for cell culture procedures except for designs #5 and #6 which collapsed. These designs failed in areas where the distance between pillars was less than 3.5 µm.

Micropillars were then coated with a layer of 10 nm of gold because PDMS is an optically transparent material and SEM images were obtained to characterise the dimensions of the final PDMS micropillars. SEM images are presented in [Figure 3.13](#). More SEM images can be found in [Table A 1](#) from [Appendix A](#).

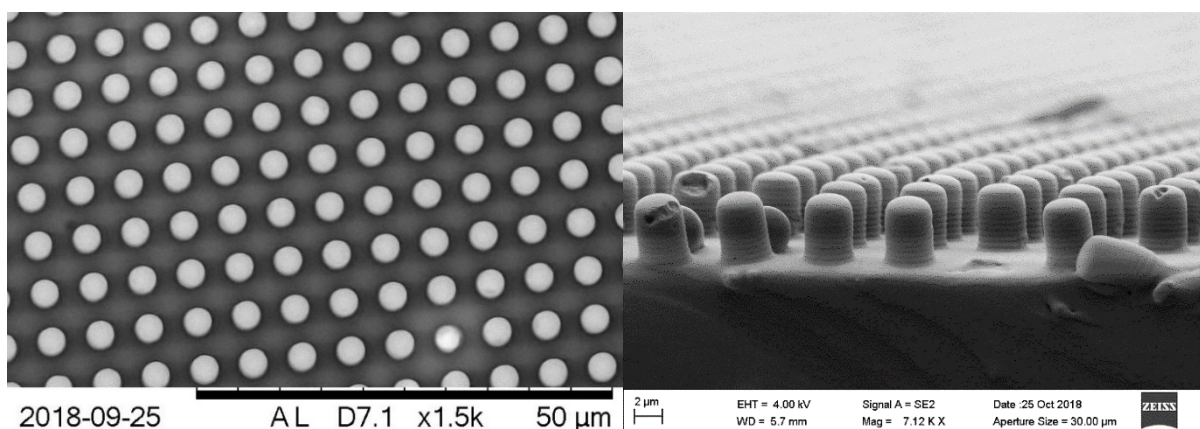


Figure 3.13. SEM images of PDMS pillars of 3 µm diameter and 5 µm length.

Dimensions and arrangement were satisfactory, it was found that in every sample around 1% of micropillars collapsed only. Length of the fabricated PDMS micropillars

was checked using a profilometer and an atomic force microscope (AFM), and their results are shown in Figure 3.14, Figure 3.15.

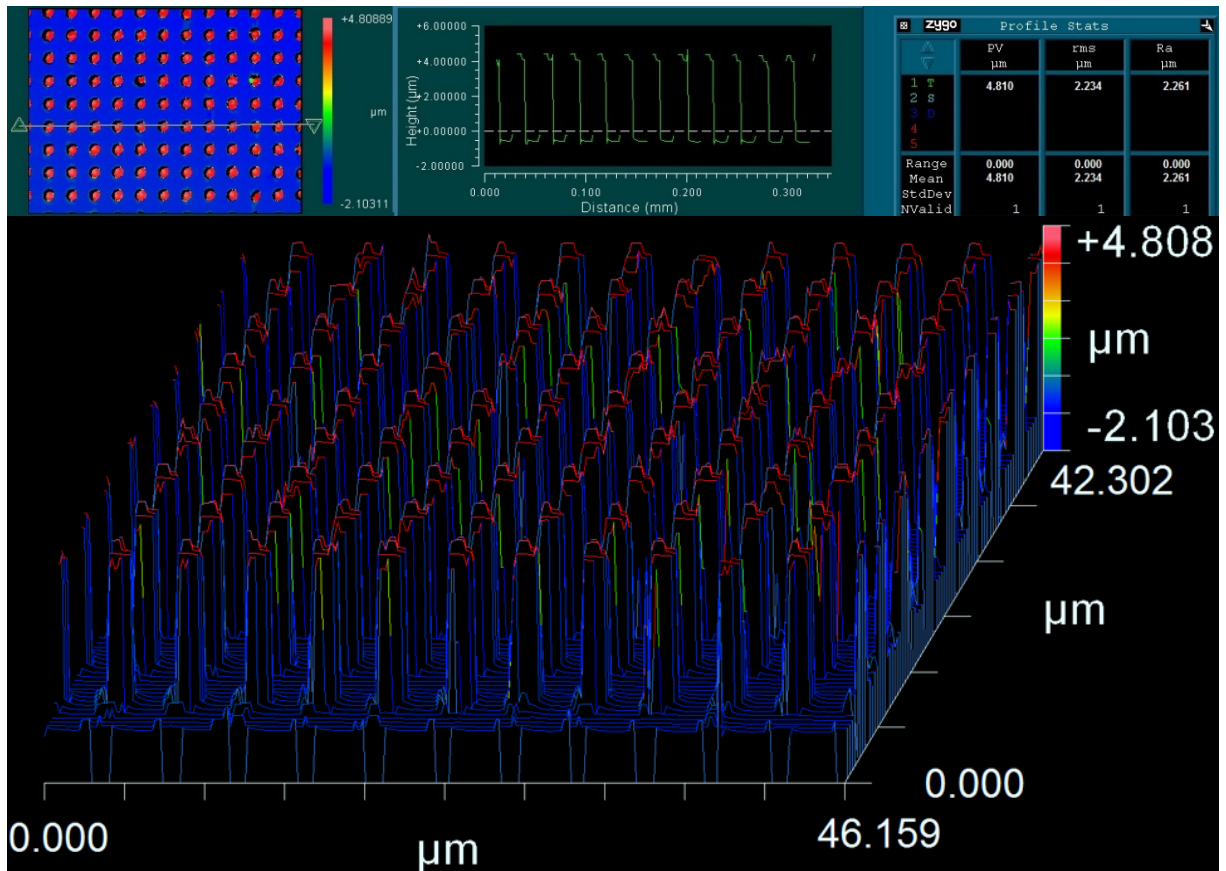


Figure 3.14. Profilometer PDMS micropillar characterisation.

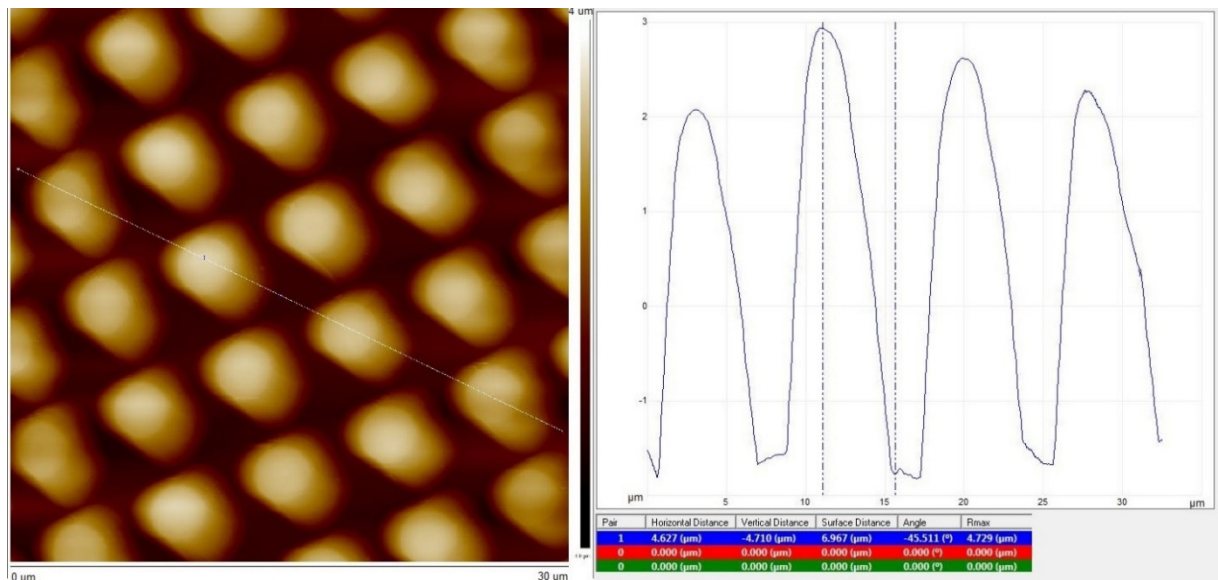


Figure 3.15. AFM results of PDMS micropillars.

Results from the profilometer showed that the length of the PDMS pillars was 4.810 µm with a standard deviation of 0.165 µm; which is in mutual agreement with the length

obtained from the silicon wafers in [Figure 3.10](#). On the other hand, AFM measurements showed some interesting results, some of the PDMS pillars were not the same high, the highest pillar is $4.710\ \mu\text{m}$ while some were as low as $4\ \mu\text{m}$ resulting in a standard deviation of $0.258\ \mu\text{m}$. This difference could be due to AFM restrictions; in other words, the AFM tip might not have the size and shape to reach the space between the pillars. This discrepancy in the pillar height led to assume a pillar height equal to $5\ \mu\text{m}$ for stiffness calculations.

3.4 Summary

This chapter presented the fabrication of the PDMS micropillar devices. These micropillars designs were $5\ \mu\text{m}$ long and had three cross-sectional areas. Two circular micropillar cross-sectional areas with $2\ \mu\text{m}$ diameter ($34.291\ \text{nN}/\mu\text{m}$ stiffness) and $3\ \mu\text{m}$ diameter ($155.969\ \text{nN}/\mu\text{m}$ stiffness) respectively. The third cross-sectional area had a major axis of $3\ \mu\text{m}$ and a minor axis of $2\ \mu\text{m}$ which had a stiffness of $56.549\ \text{nN}/\mu\text{m}$. The young modulus was estimated to be $2\ \text{MPa}$ following the recipe of the manufacturer.

Theoretical calculations were done using the Euler-Bernoulli equation and Schoen equation which were compared against FEA analysis. The key difference between them is that Schoen equation includes bending and shear deformation effects while Euler-Bernoulli only considers bending deformation effect. It was demonstrated that the Euler-Bernoulli equation was satisfactory against the FEA analysis for the elliptical micropillars. However, Schoen equation had a much closer approximation to the FEA results than the Euler equation and therefore, it was used to calculate the micropillar stiffness for circular micropillars.

Micropillars arrangements were designed with the aim to study the influence of substrate topography in cell migration behaviour. A total of 11 templates were designed, with 4 different aims. The first aim was to provide a micropillar device which had the same percentage of ECM protein all over the substrate to efficiently measure local migration forces, these are templates #1, #2 and #3. The second aim was to test the limits of the PDMS fabrication, these templates were #4, #5 and #6. The third aim, presented in design #7, was to study how cells behave in elliptical micropillars which are close to each other and do not have the same percentage of ECM protein. The

fourth and last aim was to provide a micropillar arrangement which is effective to confine cells to a specific area, these are designs #8, #9, #10 and #11.

Silicon moulds were successfully fabricated using a negative photoresist and DRIE methodology; hole diameters and depth were verified using profilometry. Then, silicon wafers were silanized with an antiadhesive solution to avoid irreversible stiction between PDMS and the silicon wafer.

PDMS was then poured, cured and peeled off under ethanol. Critical point drying was performed as a preventive measure to avoid pillar collapsing when the ethanol evaporates. All designs were successfully fabricated apart from pillars from designs #5 and #6 which collapsed due to the narrow space of less than $3.5\ \mu\text{m}$ between pillars.

Dimensions of the fabricated PDMS micropillar devices were verified with profilometry and AFM where micropillar diameter matched with the original designs. However, micropillars had different micropillar lengths ranging from 4 to $4.7\ \mu\text{m}$. Consequently, the micropillar length was estimated to be $5\ \mu\text{m}$ for calculations purposes of cell force measurements in [chapter 5.2.3](#) along with the estimated Young modulus of 2 MPa from PDMS supplier's recipe. This leads to obtaining stiffness values of $34.291\ \text{nN}/\mu\text{m}$, $155.969\ \text{nN}/\mu\text{m}$ stiffness for the micropillars with diameters of $2\ \mu\text{m}$ and $3\ \mu\text{m}$ respectively and $56.549\ \text{nN}/\mu\text{m}$ for the elliptical micropillar.

Chapter 4. Device functionalization

4.1 Introduction

Despite the fact that PDMS is a biocompatible material, the high PDMS hydrophobicity limits cell migration so it is needed to functionalize the substrate with an ECM protein [54]. This is the most critical step in this project because a good cell attachment will efficiently transmit forces to the micropillar tip. The ECM protein will be attached to the micropillar tops only and avoiding leaving residues in areas between pillars, this is because cells may attach to the protein present between pillars giving us erroneous measurements. Moreover, it is important to create aseptic conditions all over the project; therefore, PDMS devices were sterilized by autoclaving and procedures carried out in a laminar flow class II. After each functionalization method from this chapter, samples were submerged for 1 hour in pluronics F-27, this solution coats the micropillars with a non-adhesive layer to prevent possible cell migration between pillars.

This chapter presents an overview of protein adsorption mechanisms, protocols to prepare the solution containing the extracellular matrix protein (ECM) and a deep analysis of different methods to coat PDMS micropillar posts.

4.2 Understanding protein adsorption

By definition [55], adsorption is the ability of all solids to attract molecules of gases or solutions to their surfaces. Adsorption of proteins plays a key role in a system performance especially in the fields of medicine, biotechnology, food processing and biosensors. Importance issues are: controlling the amount of adsorbed protein, protein orientation, adsorption selectiveness or adsorption on specific areas depending on the application. [56]

For instance, an enzyme-linked immunoassay is often used to detect amounts of specific antibodies using proteins where the protein is first allowed to adsorb onto a plastic surface. The protein is then linked to an enzyme which reacts with the antibody to produce a detectable signal allowing detection of the antigen. The analytical sensitivity will be affected by the protein orientation which should be oriented in such a way that it can properly recognize the antibody. An example of the importance of the amount of adsorbed protein is in the design of biocompatible materials for surgical implants where adsorption of fibrinogen should be reduced as much as possible to avoid blood agglutination [56].

Adsorption can be caused by physical (physisorption) or chemical interactions (chemisorption) [55]. Physisorption is a spontaneous process where more energy is released than gained and it is more favourable at room temperature with the extra benefit of almost negligible protein denaturation. Most common methods for protein adsorption are via physisorption due to its feasibility and lower costs compared to chemisorption. However, chemisorption has the advantage over physisorption in creating a covalent bond between protein and substrate [56, 57].

The influencing factors on protein physisorption are protein properties, substrate properties and environmental conditions. As described by Nakanishi et al [56], protein adsorption is a common but complicated phenomenon specifically because the various protein properties that play a role in the amount of adsorbed protein. These properties are protein charge, size, the stability of the structure (hard or soft) and amino acid composition which roles are not fully understood. In another study, Rabe et al. [57] added to Nakanishi findings that the complexity of protein adsorption also relies on how proteins behave against contact with a substrate. This behaviour is different than small molecules that behave like rigid particles where protein attachment or detachment do not follow certain adsorption and desorption probabilities. This means that the complex composition and structure of proteins induces interesting phenomena such as structural rearrangements, surface affinities changes, size exclusion effects or surface aggregation.

However, both Nakanishi [56] and Rabe [57] agreed that among all properties, the surface hydrophobicity and the electrostatic interaction between protein and substrate have the most significant contribution to protein adsorption. This conclusion was also supported in Walgreen [58] study.

Hydrophobicity significantly affects protein adsorption where an increase in surface hydrophobicity will increase the amount of adsorbed protein regardless of protein electric charge. On the other hand, protein may adsorb to hydrophilic surfaces if opposite charges are present between them. Therefore, it is important to be aware of surface and protein properties in terms of their hydrophobicity and electrostatic state. [56, 58]

As previously stated, PDMS will be used to fabricate micropillars and it has a backbone of methyl groups (-CH₃) attached to a chain of silicon and oxygen atoms, as illustrated in [Figure 4.1](#) [59]. These methyl groups are the functional groups on the surface that

affects the hydrophobicity of the material [60-62]. As a result of being a material rich in methyl groups, it presents a very high hydrophobicity with contact angles between 95° and 120° according to previous studies [35, 54, 59, 63-69].

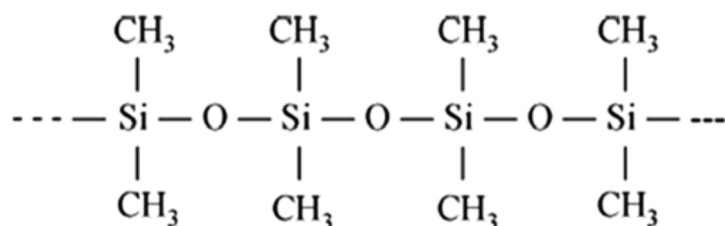


Figure 4.1. PDMS chemical structure [59].

Regarding the protein electrostatic charge, we aim to have a negatively charged protein. Two parameters define the electrostatic charge of a protein; these are the pH of the buffer where the protein is dissolved and the protein isoelectric point (pI). If the pH buffer is lower than the protein pI then the protein will be positively charged; on the other hand, if the pH buffer is higher than the protein isoelectric point then the protein will be negatively charged [57]. It is aimed to create favourable conditions to enhance adsorption such as hydrophobic surface and opposed electrically charged protein. PDMS meet the first condition by being a hydrophobic surface if untreated. For PDMS to meet the second condition, the protein is prepared in a way that is negatively charged.

4.3 Materials, methods and results

This section describes the methods used to functionalize PDMS micropillar devices, all reagents were purchased from Sigma-Aldrich (UK) unless otherwise is stated.

4.3.1 Fibronectin-FITC labelling methodology

Optical diffraction between the body of the cell and the top of the micropillar may interfere in our readings; to avoid this the protein will be labelled with a green fluorescent dye, such as Fluorescein Isothiocyanate (FITC, molecular weight (mw): 389.4 g/mol). Fibronectin protein was used to model the ECM due to its availability and for being the most common protein for cell migration studies.

Bovine fibronectin powder was purchased from Sigma Aldrich with a molecular weight of 450×10^3 g/mol (Da) and is formed by two chains of 220 KDa and 212 KDa respectively [70]. An isoelectric point of 5.46 was calculated using the ProtParam tool from the ExPASy website [71], this means that any buffer with a pH greater than 5.46 will negatively charge the fibronectin.

Firstly, 0.1 M borate buffer pH 9 was prepared by diluting 0.61 g of boric acid in 80 ml of deionised water, then 1 M sodium hydroxide (NaOH) was added until PH9 was reached and makeup with deionised water until 100 ml. Next, 1 mg of fibronectin powder was dissolved in 500 µl of borate buffer to obtain 2 mg/ml protein concentration. FITC was then dissolved in Dimethyl sulfoxide (DMSO) at 1 mg/ml concentration. As 100 ng of FITC for every 1 µg of protein is required, it was mixed 500 µl of the fibronectin solution [2 mg/ml] with 100 µl of FITC in DMSO [1 mg/ml]. Final protein solution volume was 600 µl with a concentration of 1.666 mg/ml. Finally, either the final protein solution was incubated at 37 °C for 90 min or overnight at 4 °C to let the FITC bind to the fibronectin [72].

The unbounded FITC was discarded by gel filtration and buffer changed to an appropriate storage solution such as phosphate-buffered saline (PBS) at pH 7.4. Zeba spin desalting columns with an exclusion limit of 2000-40000 g/mol purchased from Thermofisher (UK) were used for this purpose. Our labelled fibronectin FITC solution was then poured into the Zeba column where FITC with a molecular weight (389.4 g/mol) was temporally trapped into the gel [73].

A gel filtration drawback is that the original solution is diluted in order to maximise the number of collected particles; therefore, the final concentration was measured on each labelling to have consistency between experiments. Furthermore, the efficiency of the labelling was determined by the molar fluorescing protein ratio. A Nanodrop was used to obtain both parameters.

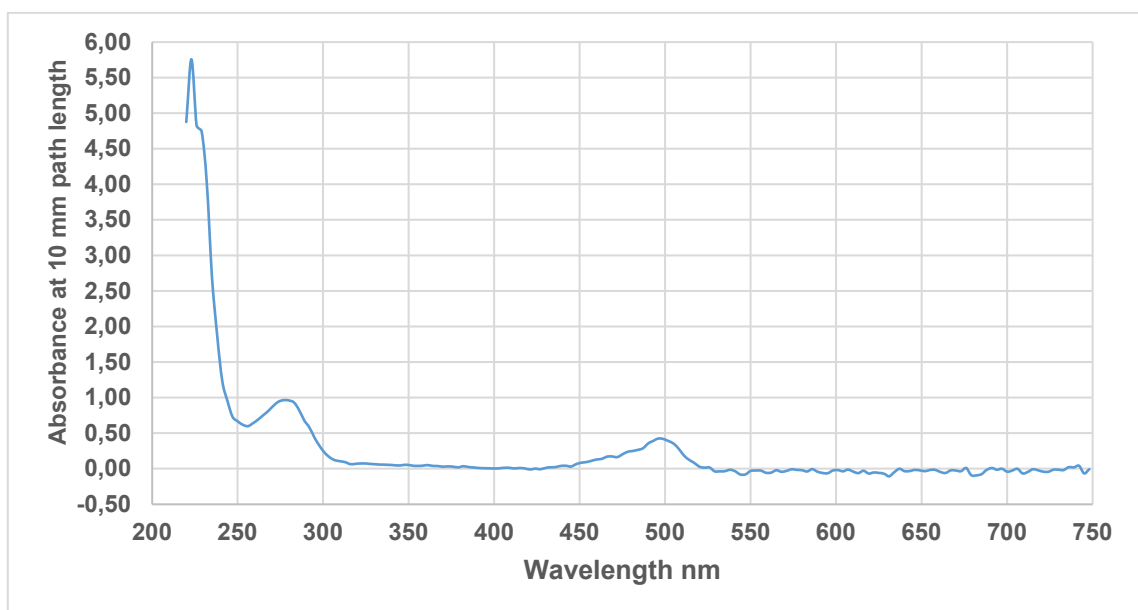


Figure 4.2. Nanodrop results from a FITC-Fibronectin labelling.

According to SIGMA-ALDRICH suggestion [74], the optimal fluorescein protein ratio should be between 0.3-1.0 to avoid either low signal or high background. However, this may change depending on the application. For instance, our micropillar tips have a small area (2-3 μm diameter) resulting in adsorption of only a few protein molecules to each pillar. Therefore, we prioritise the fluorescence signal for a feasible micropillar detection with higher values of fluorescein protein ratio than SIGMA suggestion. Nanodrop results are presented in [Figure 4.2](#).

Results for absorbance at 280 nm and 495 nm wavelengths were 0.956 and 0.420 respectively with 0.7 mg/ml protein concentration. The formula [74] to calculate the fluorescein protein ratio is:

$$\text{Molar } \frac{F}{P} = \frac{MW * E^{0.1\%}}{389 * 195} * \frac{A_{495}}{A_{280} - (0.35 * A_{495})} \quad \text{Eq. 7}$$

where MW is the protein molecular weight, $E^{0.1\%}$ is the protein's percentage extinction coefficient at 0.1%, A_{495} is the absorbance of FITC at 495 nm, A_{280} is the absorbance of protein at 280 nm, 389 is the FITC molecular weight and 195 is the FITC's percentage extinction coefficient at 0.1% [74].

From the manufacturer SIGMA [74], $E^{1\%}=12.9$ and MW is 220 KDa, replacing these values and the measured absorbance values ($A_{495}= 0.42$ and $A_{280}=0.956$) we obtain a fluorescein protein ratio of 1.942. If we experience a high background after labelling our micropillars, we will need to reduce the amount of FITC during the ECM protein preparation.

SDS-PAGE technique (sodium dodecyl sulphate–polyacrylamide gel electrophoresis) was used to ascertain that all unbound FITC was removed from the solution after performing gel filtration. This technique separates molecules according to its molecular masses within 5 to 250 KDa range using an electric field. The sodium dodecyl sulphate (SDS) and coomassie brilliant blue stain help to identify the molecular weight of the molecules within the gel using a camera. Then the camera is set to detect only FITC fluorescence to ascertain that all the fibronectin was labelled [75].

Firstly, our ECM protein solution was mixed with SDS at 1% concentration and then heated at 95 $^{\circ}\text{C}$ for 10 min. The heat will facilitate the denaturation process caused by SDS, this means the disruption of secondary, tertiary and quaternary structures that

will unfold the protein. This will bring the fibronectin to its two linear molecules of 220 KDa and 212 KDa respectively [76-78].

Once the protein was unfolded, the sample was added into three wells to the electrophoresis chamber to separate the molecules by mass. During electrophoresis chamber preparation, the percentage of polyacrylamide gel was kept low (7.5%) for better viewing of the bands. Once the electrophoresis process was finished, the gel was submerged into coomassie brilliant blue stain targeting the reference bands and the protein, see [Figure 4.3\(a\)](#). Prior to adding the coomassie stain, a fluorescent image for FITC (green) was captured to show where the FITC from the labelled protein falls, as seen in [Figure 4.3\(b\)](#).

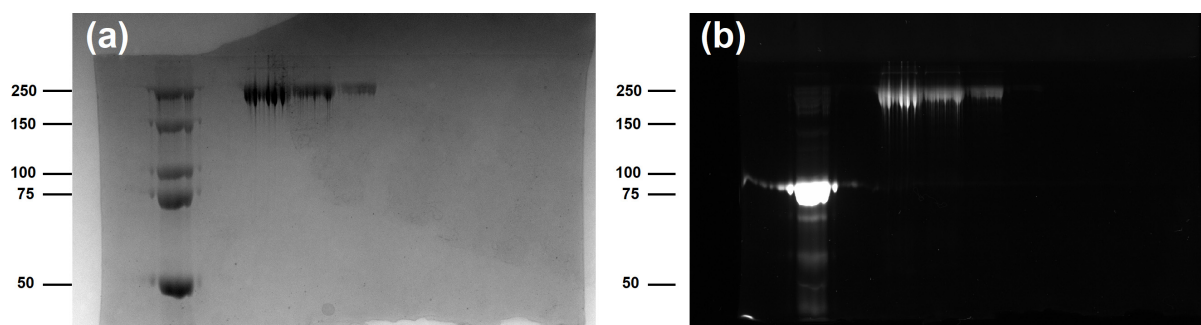


Figure 4.3. SDS-PAGE results of FITC-Fibronectin solution (a) Coomassie Brilliant Blue and (b) fluorescent FITC filter.

Results confirm that the mass weight of coomassie brilliant blue stain and FITC labelled pictures match at an approximate value of 220 KDa. At this stage, our ECM protein was ready to be used to stain the tips of our micropillars.

4.3.2 Microcontact printing technique (μ CP)

Microcontact printing technique (μ CP) is a technique where PDMS stamps are inked with a solution to be transferred to a flat substrate where glass and metals (e.g. silicon, gold, and palladium) are often used. These stamps contain the pattern to be transferred. The technique is illustrated in [Figure 4.4](#). [79-84]

Concisely, the stamp with the desired patterns is inked with a solution containing the molecules to be transferred. The solution is then removed, and the stamp is dried with a stream of N_2 . Next, the stamp is brought into contact with the substrate and peeled off. The low interfacial free energy from PDMS (21.6 mN/m) do not allow molecules to irreversible adhere to it; therefore, molecules are successfully transferred to the substrate [81]. Furthermore, it is important to put the stamp in contact with the substrate

as soon as it is dried; it was recorded [82] that after 1 min, the success of transfer is significantly decreased.

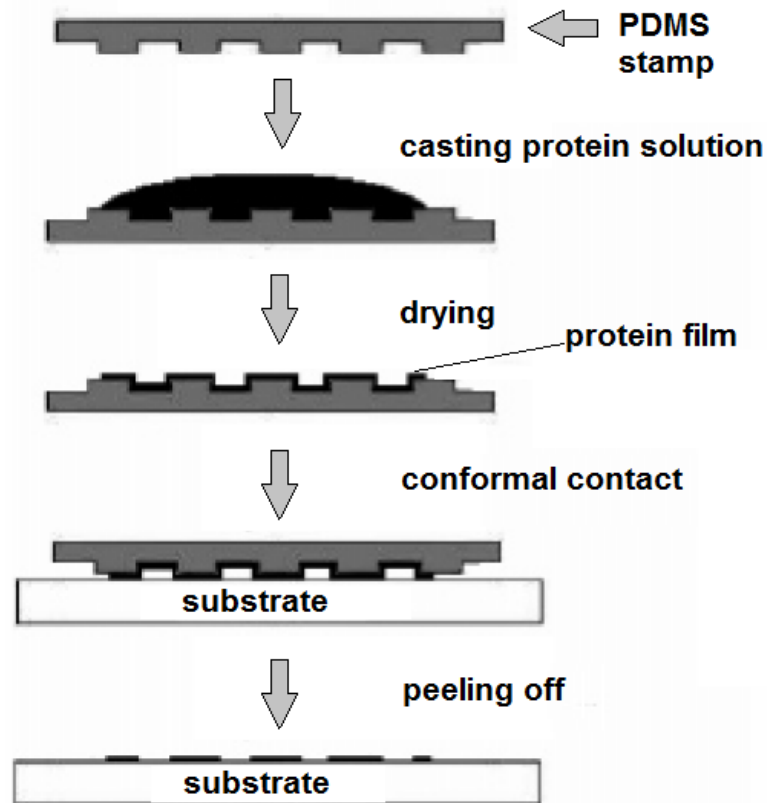


Figure 4.4. Traditional microcontact printing technique[79].

This technique has many advantages such as low cost, no need for specialised labs such as clean room, and it is easy to learn [81, 84]. It was initially developed to transfer thiol groups; however, it may be used to transfer silanes, lipids, proteins, Deoxyribonucleic acid (DNA), nanoparticles and metal nanofilms as well [84].

4.3.3 Reverse microcontact printing technique (R μ CP)

In this project, we used a variation of μ CP called reverse micro printing technique and it is the most common technique to dye the tip of micropillars as recorded by previous researchers [25-27, 29-32, 34-39]. This methodology is similar to the microprinting technique with the difference that the ECM protein is transferred from a flat stamp to a substrate containing patterns. One major difference is the substrate exposure to either oxygen plasma or ozone treatment prior to microprinting to reduce its hydrophobicity. The high PDMS hydrophobicity may cause agglomeration of the ECM protein solution. This exposure to oxygen plasma is not needed in normal μ CP because glass and metals are hydrophilic by nature, allowing liquids to spread in the substrate. The process is illustrated in [Figure 4.5](#).

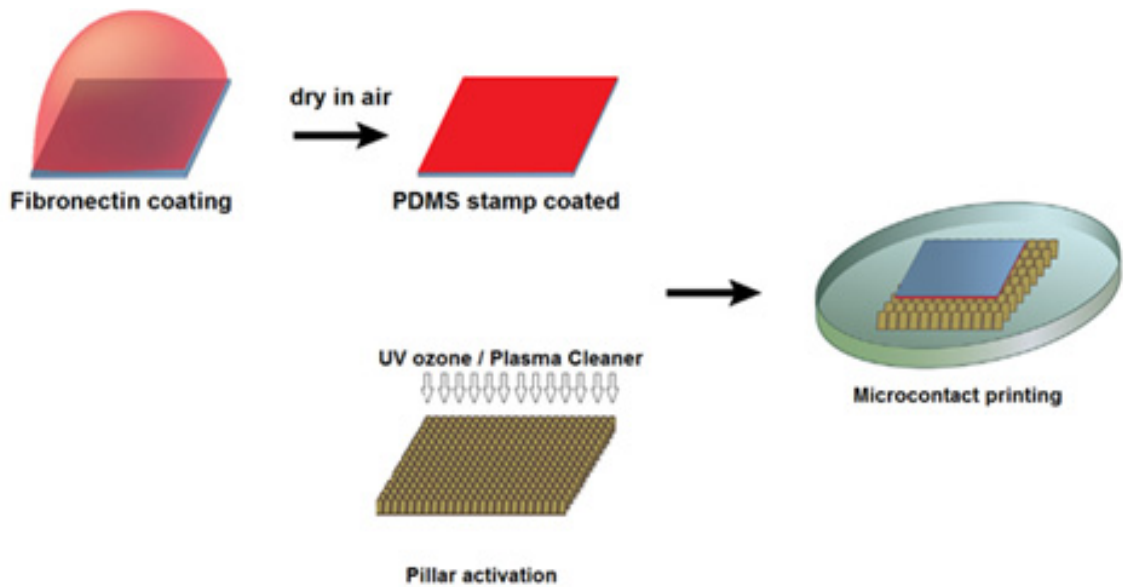


Figure 4.5. Soft lithography process flow.

A flat PDMS stamp was prepared with 1:10 curing agent - base polymer ratio using a petri dish as a mould. Then it was degassed for 30 min, cured at 65 °C for 1 hour and cut to a size slightly smaller than the PDMS micropillar substrate. Next, the stamp was covered with 50 µl of the ECM protein solution and incubated for 1 h at room temperature under a laminar flow hood protected from light to avoid photobleaching the dye.

Next, the micropillar substrate was exposed to oxygen plasma at 30 W for 60 s, in order to make the surface less hydrophobic and therefore a uniform coating was achieved. The incubated ECM protein solution was pipetted out, the stamp was then rinsed with PBS and sterile deionised water and dried with a stream of nitrogen. Immediately, the fibronectin-coated stamp face was placed in contact with the top of the micropillars with gentle pressure and incubated for 3 min to transfer fibronectin from the stamp to the substrate by adsorption. Excessive pressure will damage the micropillars.

4.3.3.1 R μ CP results

First results showed a very weak fluorescent signal where it was needed to use high exposure times around 25 s to be able to see it. This prolonged exposure to light causes high background between pillars and photobleaching of the FITC dye after a few seconds, as seen in [Figure 4.6](#).

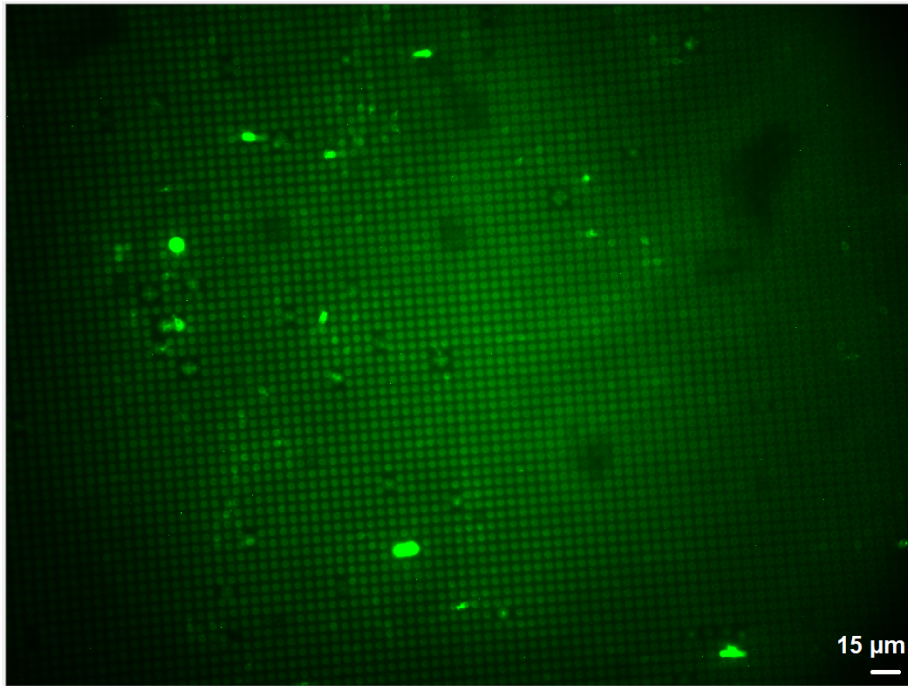


Figure 4.6. Protein transfer by soft lithography. 25 s exposure time.

This poor transfer might be attributed to not conformal contact between stamp and substrate. To ascertain this theory, a slight weight of 20 g was added to the top of the stamp during printing step and it is expected to obtain a stronger signal. Results are illustrated in [Figure 4.7](#); as expected, the exposure time was reduced from 20 s to 1 s proving that a stronger fluorescence signal was achieved.

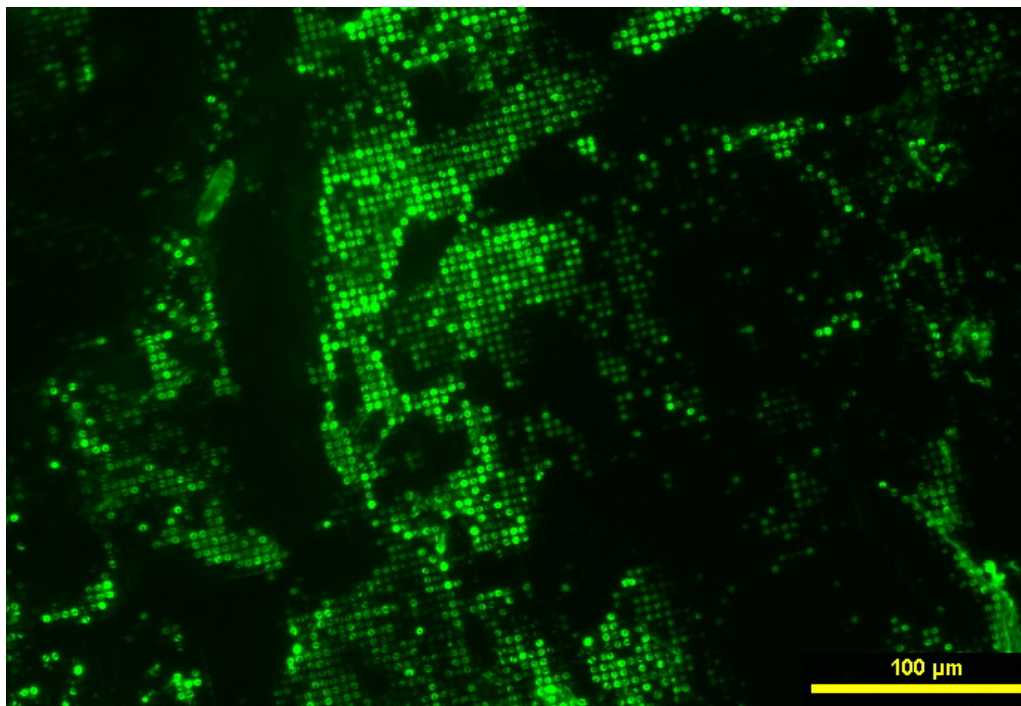


Figure 4.7. Non-uniformity protein transfer by soft lithography. 1 s exposure time. 5 min stamp pillar contact time.

However, the transfer was not uniform with clusters of protein. This may be caused by PDMS auto hydrophobicity recovery; it is well known that PDMS start to recover its hydrophobicity after a short period of time [65, 67, 68, 85, 86]. The hydrophobicity causes the ECM protein solution to group in small droplets once it is in contact with the pillars and consequently, the transfer was not uniform [84]. Therefore, the PDMS hydrophobicity level was studied by exposing the samples to oxygen plasma.

The power level was kept to a constant value of 30 W power, 10-sccm oxygen mass flow and the exposure time was varied, then the water contact angle was measured to obtain the hydrophobicity level. Results are presented in [Figure 4.8](#) and [Figure 4.9](#).

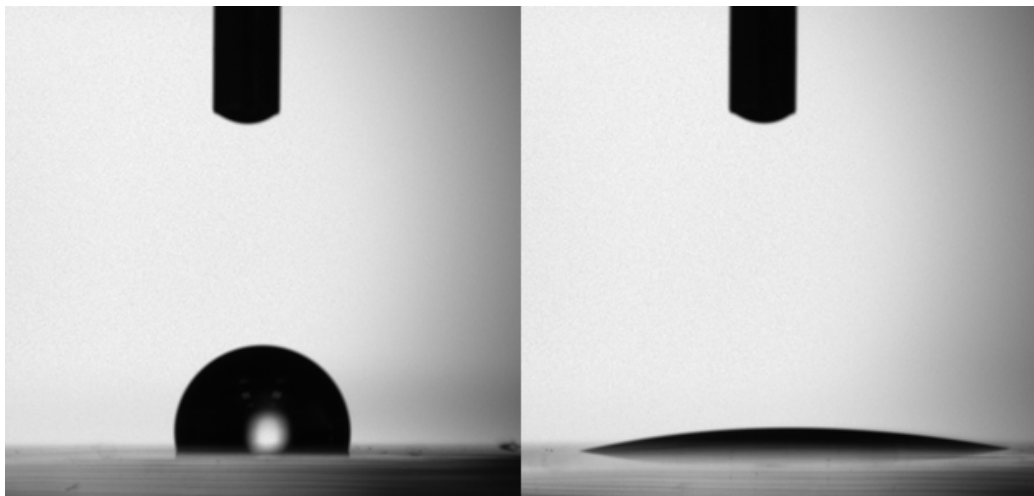


Figure 4.8. (Left) Contact angle before treatment. (Right) Contact angle after exposing for 90 s to oxygen plasma.

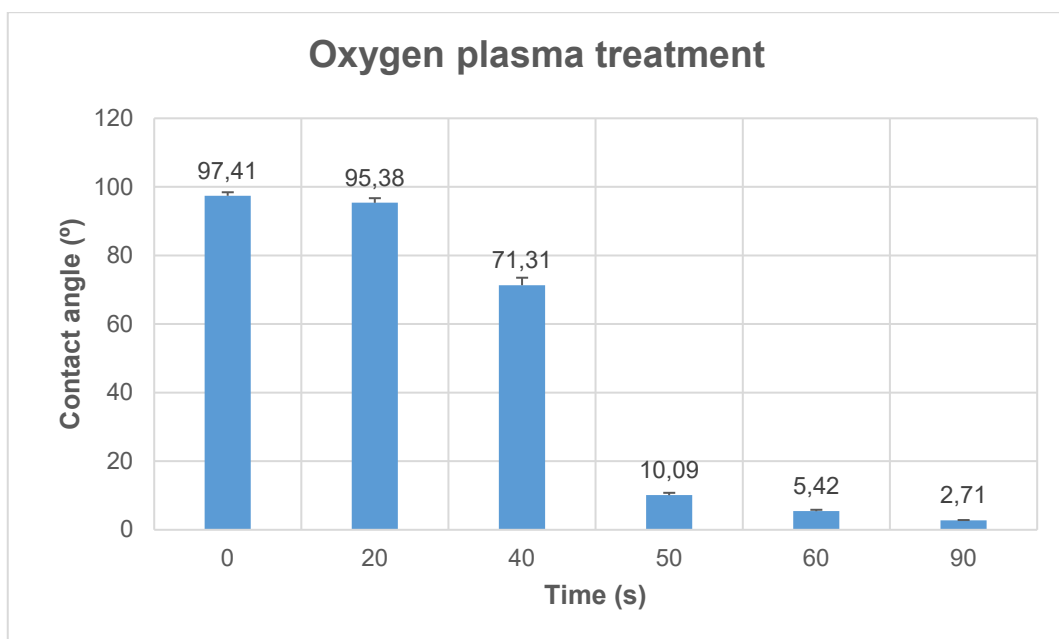


Figure 4.9. Water contact angle vs oxygen plasma exposure time in seconds.

Results suggested that water angle of non-treated PDMS was 97.41° which is in mutual agreement with values measured by previous researchers; for instance, Morent et al. [59] 107.6° , Demmin et al. [63] 115° , Gokaltun et al. [64] 112° , Tan et al. [65] 120° , Mata et al. [66] 108° , Kameya et al. [67] 105.6° , Wang et al. [68] 110° , Bodas et al. [69] 112° , Kuddannaya et al. [54] 114° and Chuah [35] et al. 108° . During the first 20 s of exposure to oxygen plasma, the contact angle decreased by 2° only and then the contact angle decreased by 24.07° in the 20-40 s range. The major decrease in the contact angle was seen in the 40-50 s range where it drastically dropped from 71.31° to 10.09° .

After 50 s of exposure time, the contact angle presented slight decreases. This demonstrates that PDMS needs to be exposed to oxygen plasma at least for 40 s to significantly decrease its hydrophobicity and exposures higher than 50 s are insignificant. Therefore, the exposure time used in our experiments was correct and this non-uniform coating may be due to a different cause. Measurements were significantly different with a $p\text{-value} < 0.01$.

Other hypotheses for non-uniform transfer is the variation in micropillars length, as previously seen in [section 3.3](#), or possible deformations on the stamp surface that will impede conformal contact between pillars and stamp.

Overall, protein transfer was either null or non-uniform. Even though that addition of weight improved it, it was not satisfactory enough to track pillars in our experiments and these results will be provided in [Chapter 5](#). Therefore, a more reliable method must be delivered.

4.3.4 Adapted method for reverse micro printing technique

Based on the hypothesis that conformal contact was not achieved because deformations in the stamp, we decided to change the stamp material to glass. Some of the benefits of using glass are that it is non-deformable, it has a flatter surface than PDMS and it has been extensively used in biology procedures.

Glass slides were cut into squares slightly smaller than the PDMS devices; this is 10x10 mm. It is important to clean the glass as much as possible to avoid the presence of particles in its surface, so the glass stamps were cleaned with acetone and exposed to oxygen plasma for 20 minutes. Oxygen plasma will render glass surface hydrophilic and this will not allow the protein to be transferred from the stamp to the micropillars. Therefore, we need to increase its contact angle by coating with a silane; we choose

to use (3-Aminopropyl) triethoxysilane (APTES) due to his demonstrated suitability for cell culture procedures [35, 54, 87-90].

The glass stamp was then submerged into a solution of 10% APTES in ethanol for 1 hour at room temperature. Mean contact angle after APTES treatment was 50.73°, which is in mutual agreement with values calculated by Siddique et al [87].

Next, a drop of 20 µl was added to the stamp of the ECM protein and it was incubated for 1 hour at 2 °C in a humidified petri dish to avoid the risk of evaporation. ECM protein was pipetted out and the stamp was dried with a stream of N₂. Immediately, the stamp was put in contact with the micropillars for 3 min and a weight of 20 g was added on the stamp as seen in [Figure 4.10](#).

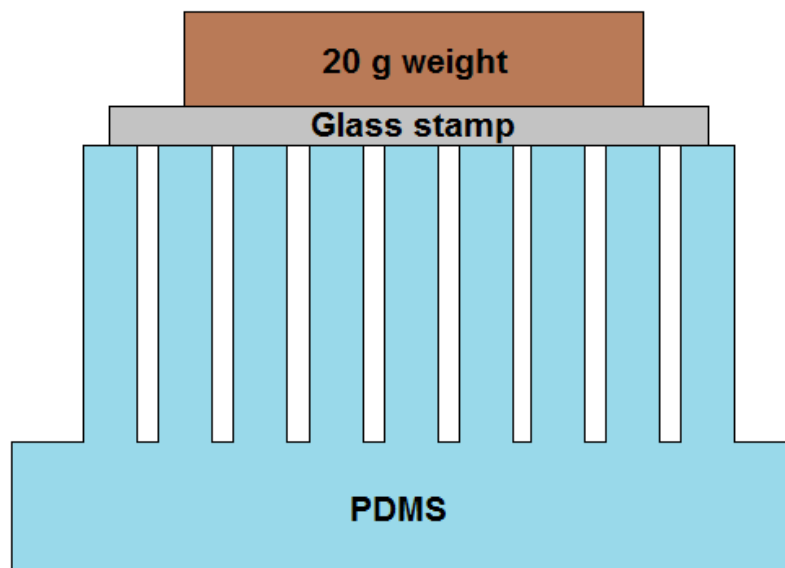


Figure 4.10. Adapted microcontact printing technique schematic view. Protein in the glass stamp is pressed against the tip of the pillars with the aid of a 20 g weight.

4.3.4.1 Adapted R_µCP results

Results are presented in [Figure 4.11](#) and show a uniform coating, brightfield images were used as control. Some areas give the impression that some pillars were unsuccessfully labelled, this is because these pillars were snapped avoiding them to be in contact with the stamp. This proves the accuracy and resolution of this adapted printing technique as printing only occurs in areas where the pillars are in contact with the stamp.

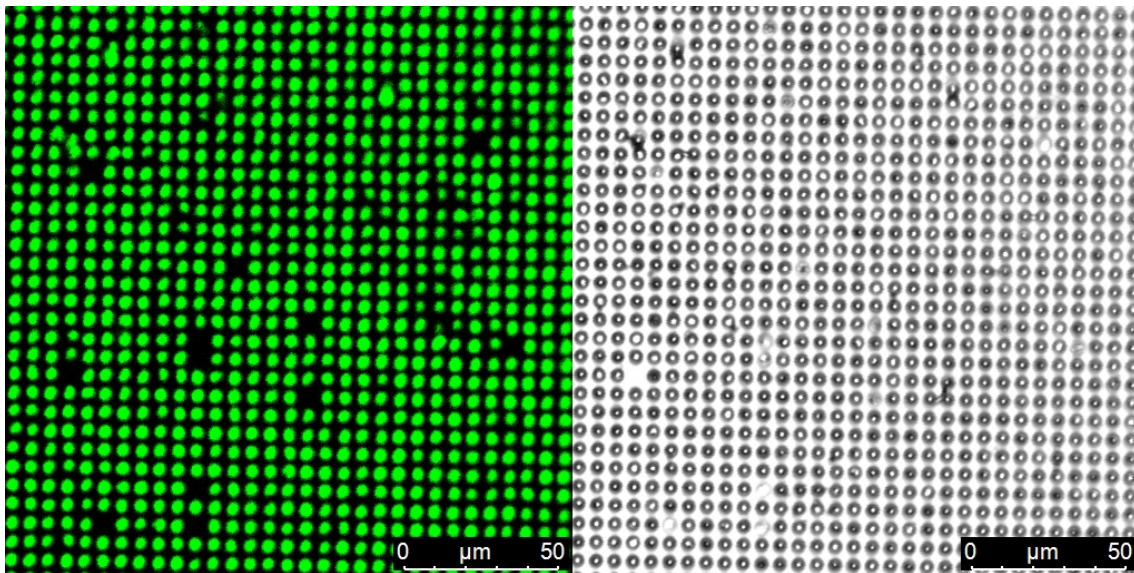


Figure 4.11. Adapted method for μ CP (Left) fluorescent. (Right) brightfield.

To ascertain if the transfer occurs only in areas in contact with the stamp, an image was acquired in the edge of the stamp footprint. Results are presented in Figure 4.12 and it clearly shows both areas, labelled and unlabelled pillars. Some advantages of this method are the reduction of the quantity of ECM protein solution from 50 μ l to 20 μ l and strong fluorescent signal.

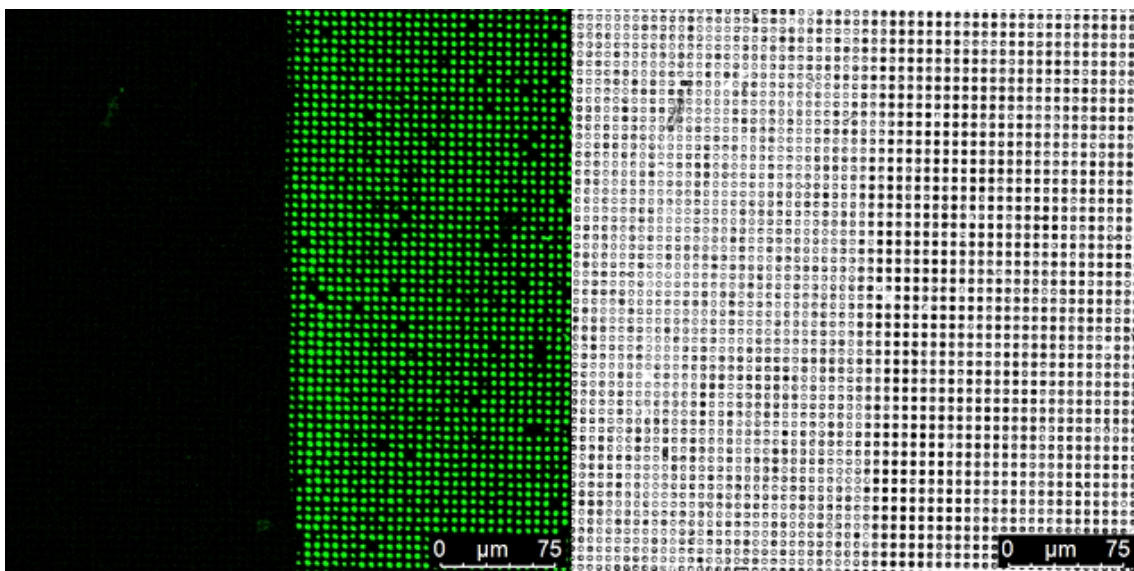


Figure 4.12. Adapted method for μ CP showing the edge of printing (Left) fluorescent and brightfield image (right).

The reliability of this method was tested, and it was seen that 70% of the samples were successfully coated, this means that ECM protein was present in the micropillar tips only with a strong fluorescent signal. Unsuccessful samples did not present ECM protein at all.

After a few weeks, all samples started to show areas where the protein was not transferred at all. The method was repeated several times with thorough care in every step with no improvement in the results. This poor protein adsorption was then suspected to be due to deterioration of the APTES solution. Therefore, a new bottle of APTES was purchased, the method was performed again and unfortunately, the issue was not solved. Furthermore, the weight on top of the stamp was increased as a measure to solve this problem. The weight was gradually increased by 2 g on every attempt until the pillars started to collapse when the weight was 40 g with no improvement in the protein adsorption. Consequently, this method was discarded.

4.3.5 Silane method

Apart from the fact that micro contact-printing technique failed to provide a uniform coating; the contact with air during the drying step may there lead to protein denaturation [82, 84]. So, another method was explored by Ganz [39] and Ladoux [91] which do not allow the protein to dry, this method transfer antibodies on PDMS flat surfaces. Hydrophobic interactions between the liquid and the surface cause the protein to adsorb. Briefly, a drop of antibody is put in contact with a silanized micropillar surface and then flattened with a glass coverslip. According to this study, capillarity avoids the solution to go between micropillars.

This methodology was slightly modified for this project. Firstly, the micropillars were treated with oxygen plasma for 1 min at 30 W and silanized under vacuum with Perfluorooctyl-trichlorosilane for 30 min to increase the contact angle to 120°. Next, 50 µl of the ECM protein was deposited all over the surface, flattened with a piece of glass coverslip to avoid protein solution clumps and then it was incubated overnight at 4 °C. This was done in a moisturised petri dish and sealed with parafilm to avoid evaporation of the ECM protein solution. Finally, the device was washed with PBS and sterile deionised water (SDW) twice.

4.3.5.1 Silane method results

Results shown in [Figure 4.13](#) had positive aspects such as good protein adsorption to PDMS micropillar tips, strong fluorescent signal and no adsorption between pillars. On the other hand, protein creates interesting protein links that look like “bridges”. This might create a problem with the customised MATLAB code during the cell migration analysis, this is because the code optically recognises circular micropillars and this will

be interfered by these “bridges”. One explanation might be the tendency of protein solution aggregation against a remarkably high hydrophobic surface.

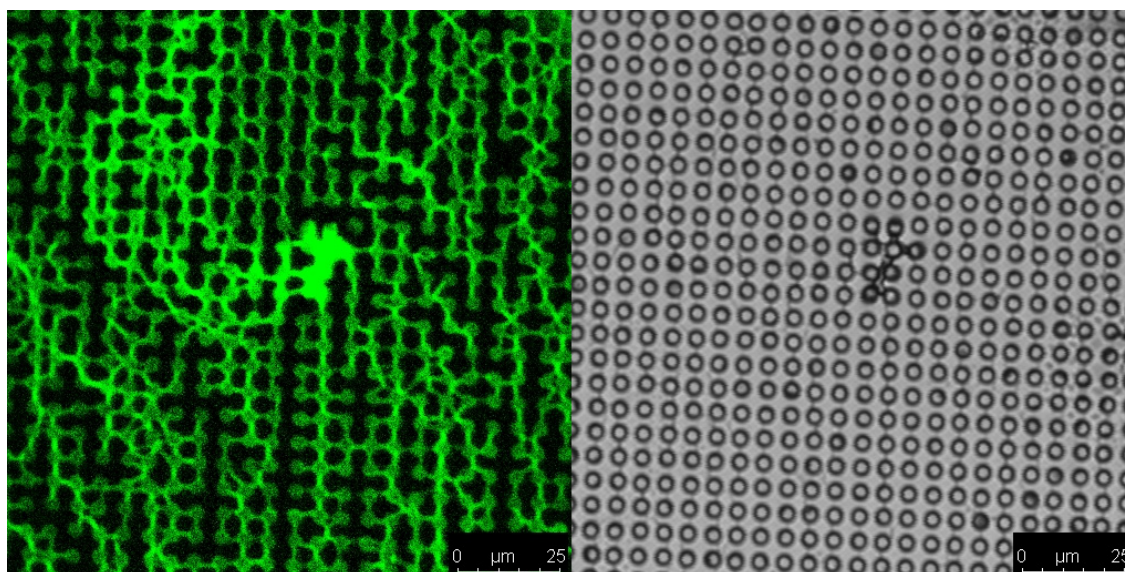


Figure 4.13. Silane method. (Left) fluorescent image of protein adsorption showing “bridges” between pillars. (Right) brightfield image used as control.

In order to break this protein bridges, we applied gentle sonication in ethanol for 30 s. Sonicating the coated devices may bring two outcomes, protein denaturation due to the rise in temperature and collapse of micropillars. Results after sonication are presented in [Figure 4.14](#).

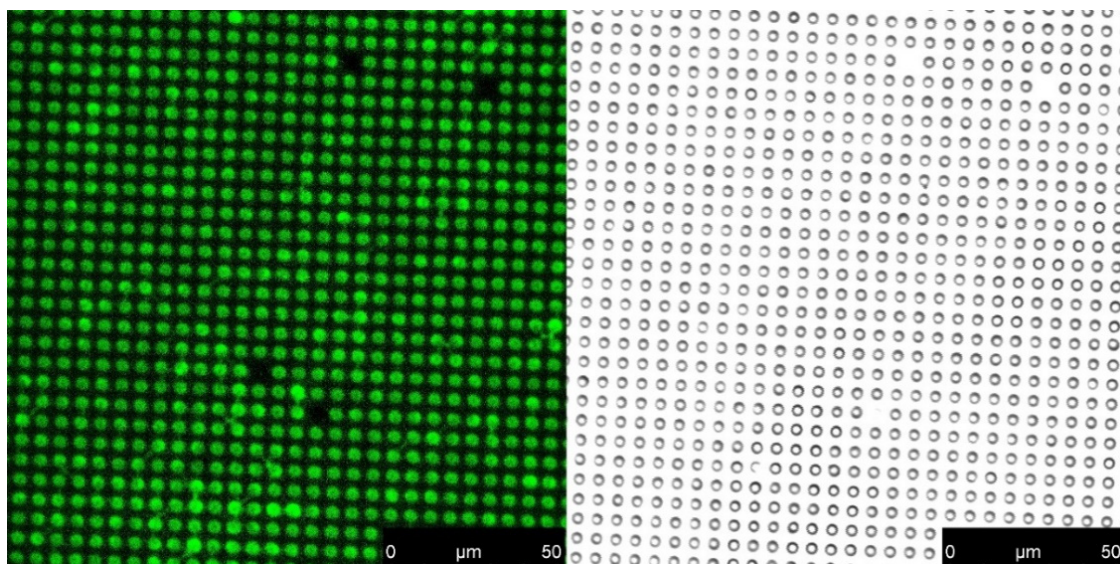


Figure 4.14. Silane method results. (Left) Fluorescent image of successful protein adsorption. (Right) brightfield image used as control.

After applying sonication, the protein bridges were removed showing results as good as the adapted μ CP technique; however, the repeatability of this method was around

35%. Failed samples presented collapsing pillars and/or protein bridges that couldn't be removed by sonication.

4.3.6 Micropillar array functionalization via Glutaraldehyde

After failing to obtain a reliable method to coat micropillar devices, we moved to chemical functionalization based on previous studies of microfluidics devices. The aim of this methodologies is to obtain a covalent bond between ECM protein and PDMS surface.

One of the outcomes of using chemicals in PDMS is the need to carefully choose which chemicals are going to be used, because PDMS may deform or etch in contact at some degree with nonpolar solvents. This chemical affinity to PDMS was studied by Lee et al [92] and his results are presented in Figure 4.15.

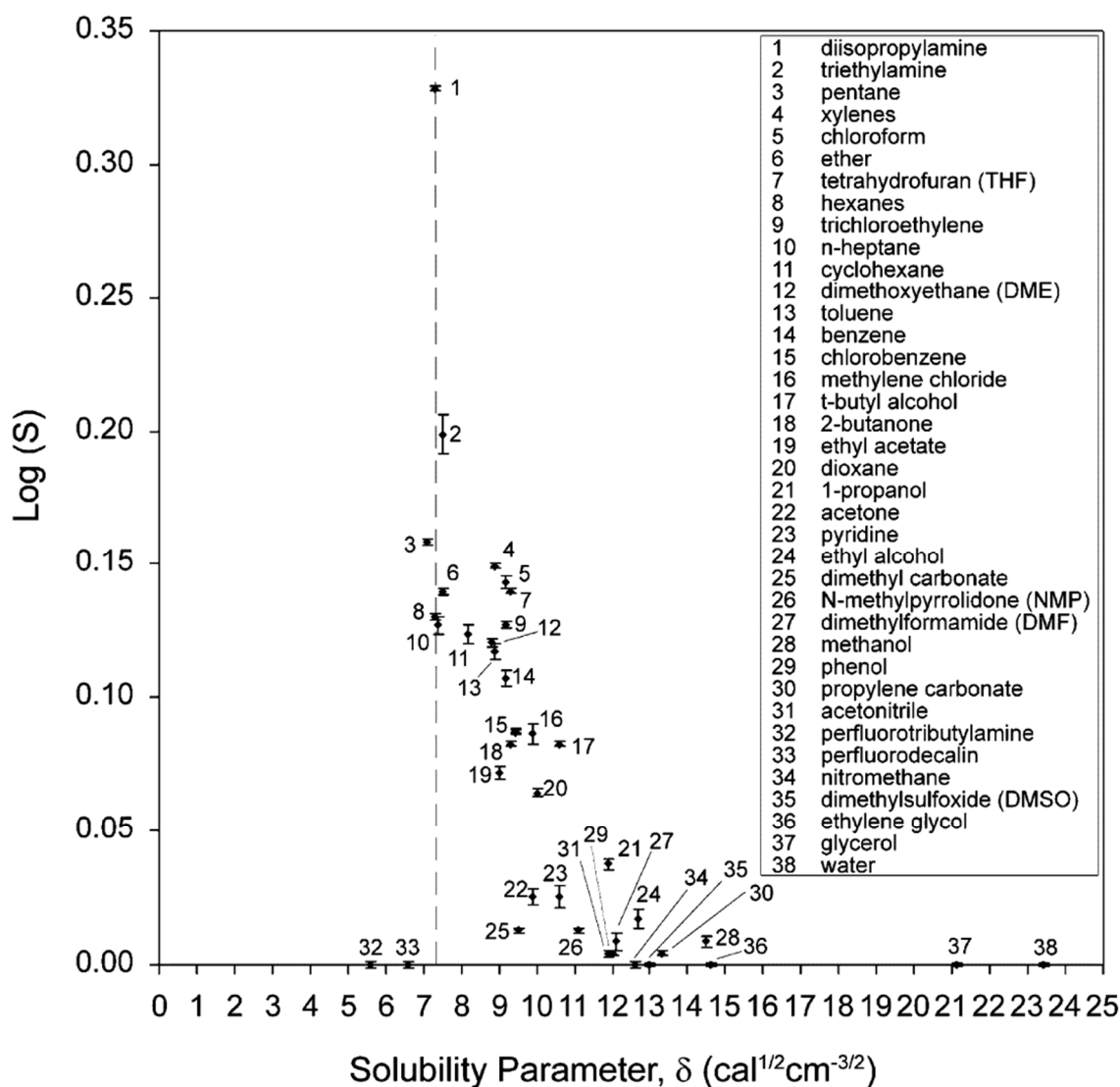


Figure 4.15. Relationship between swelling ratio and solubility parameter. Solvents are ranked according to his ability to swell PDMS [92].

The solubility parameter, δ ($\text{cal}^{1/2}\text{cm}^{-3/2}$), is often used to calculate the solubility of two materials. Two materials are soluble if they have a similar δ because overcoming this energy will allow the molecules of the solvent to enter the solute. Crosslinked polymers such as PDMS can't be dissolved and their solubility is measured by the change in dimensions, S (D/D_0), called swelling ratio. Therefore, it is expected that the swelling ratio increases when two materials have a closer cohesive energy density between them. However, this hypothesis is not always true because relationship δ vs S was experimentally found to be non-linear. For instance, acetone and methylene chloride have the same solubility parameter ($\delta = 9.9 \text{ cal}^{1/2}\text{cm}^{-3/2}$) and it is expected to swell PDMS in the same degree, but methylene chloride swells PDMS much more than acetone. This is due to the polarity of the solvent against PDMS where dispersion, polar and hydrogen-bonding forces are involved. Unfortunately, these parameters for PDMS are not available for most solvents and must be experimentally found. This paper ranked common solutions according to its ability to swell PDMS; consequently, this paper served as a guide to choose the chemicals to be used during our functionalization.

The following methodology aims to provide a strong, reliable and bio-friendly binding between PDMS and the ECM protein. The most common techniques to create functional groups on PDMS is the coating with 10% APTES in ethanol to generate primary amine groups ($-\text{NH}_2$) and then adding a crosslinker that will create a covalent bond between PDMS and the ECM protein [88, 93-95].

Prior coating with APTES, the methyl groups ($-\text{CH}_3$) from the native PDMS must be converted to hydroxyl groups ($-\text{OH}$) which will covalently bind to the silanes present in APTES. This can be done by exposing PDMS to oxygen plasma with the extra benefit of removing contaminants on the substrate and creating a temporal hydrophilic surface [96].

Glutaraldehyde (GA) is a protein crosslinking agent widely used in multiple fields such as histochemistry, cytochemistry, chemical sterilization, biomedical and pharmaceutical. It's a clear, cheap and soluble in organic solvents, ethanol and water and reacts quickly with amine groups at neutral pH. It has been demonstrated to be the most reliable cross-linking agent between the aldehyde family because of its 5-carbon atom chain length. Additionally, aldehyde groups ($-\text{CHO}$) present in glutaraldehyde can react with a range of functional groups such as thiol, phenol, amine and imidazole. In this project, we aim to create a covalent bond between the primary

amine groups (-NH₂) present in APTES with the amine groups from the ECM protein by using glutaraldehyde as a linker [97, 98].

The following methodology was adapted from previous studies [35, 54, 88-90] in PDMS surfaces. In every step, the micropillar surface was kept always wet to avoid collapsing of pillars due to evaporation forces. Firstly, the plasma oxidized PDMS was submerged into a solution of 10% APTES in ethanol for 1 hour at room temperature and then the device was rinsed in ethanol and SDW thrice to remove loosely bound APTES. Next, devices were submerged into a solution of 5% Glutaraldehyde in SDW for 30 min followed by a rinse in SDW thrice. Then a drop of 10 µl of ECM protein was deposited on the PDMS micropillar surface and incubated overnight at 4 °C in a moisturised petri dish. Finally, the device was rinsed in PBS and SDW thrice to remove unreacted ECM protein. An illustration of the chemical reactions is presented in [Figure 4.16](#).

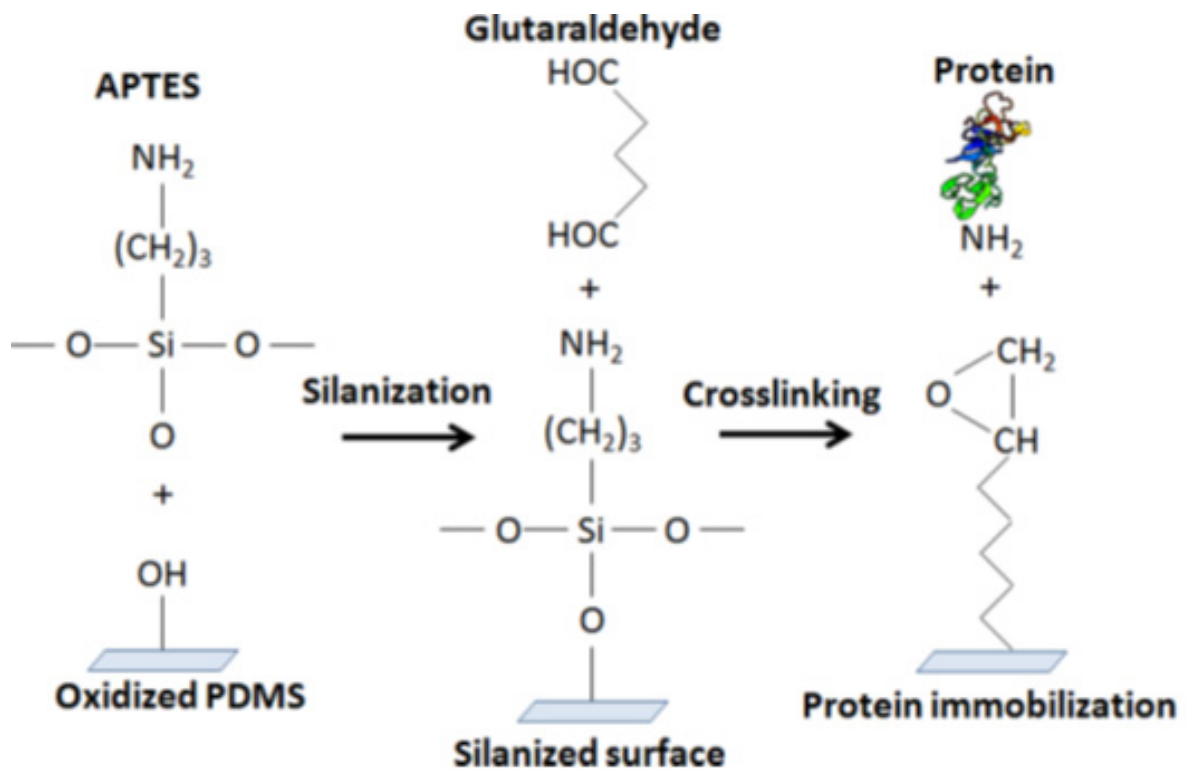


Figure 4.16. Schematic illustration of PDMS functionalization with GA [54].

4.3.6.1 Glutaraldehyde functionalization results

To characterise the surface modification of PDMS, contact angles were measured after coating with APTES and then after Glutaraldehyde. Prior to each contact angle measurement, we washed the samples 5 times in a solution of 0.1% Tween 20 in PBS, then twice in SDW and dried using CPD. The aim of these washes was to remove either APTES or Glutaraldehyde which was not covalently bound.

For APTES, we obtained an average contact angle of 51° which is in mutual agreement with Siddique [87], Chuah [35] and Kuddannaya [54]. In the case of Glutaraldehyde, we measured a mean contact angle of 40° in mutual agreement with Chuah [35] and Kuddannaya [54]. These results prove that APTES and Glutaraldehyde were successfully bound to the PDMS surface

Fluorescent images served as characterisation of the ECM protein coating. Promising results were seen where ECM protein bound only to the tip of the pillars with a strong fluorescent signal. However, some micropillar areas were not coated, as seen in the dark areas from the fluorescent image in Figure 4.17.

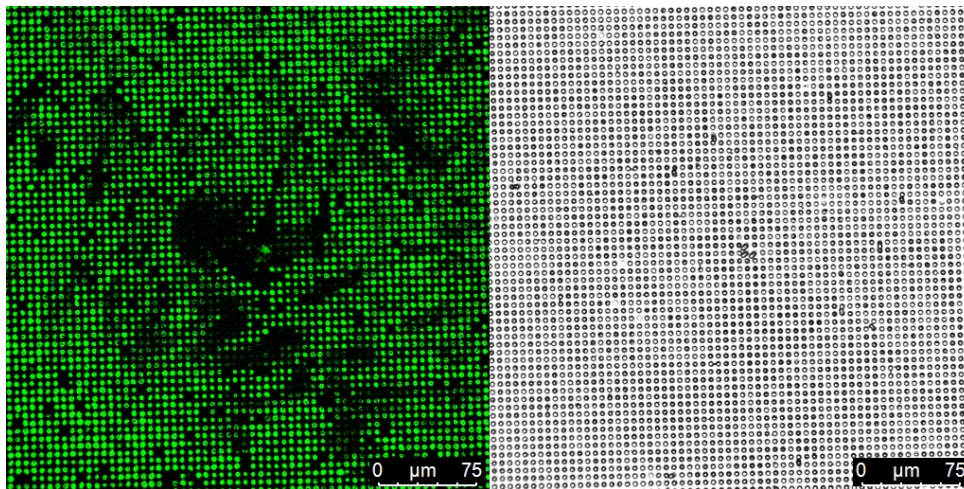


Figure 4.17. Micropillar array functionalization with glutaraldehyde crosslinker. (left) fluorescent (right) brightfield.

This is caused because glutaraldehyde is a homobifunctional cross-linker with two identical functional groups causing protein self-crosslinking. This functional groups randomly react with primary amino groups creating covalent bonds between any NH_2 groups in the system. This means that some NH_2 groups from the protein will covalently bind to amino groups from the surface or the undesirable crosslinking to other NH_2 groups from the ECM protein itself [88, 99].

4.3.7 Micropillar array functionalization via EDC/NHS coupling

To overcome this protein self-crosslinking, heterobifunctional crosslinkers are used because they have different reactive groups allowing sequential (two-step) and one-step conjugations, this reduces protein self-crosslinking and therefore a more uniform coating may be achieved. A well-established method for crosslinking proteins to surfaces is the use of 1-Ethyl-3-(3-dimethylaminopropyl) carbodiimide (EDC) and N-hydroxysuccinimide (NHS) heterobifunctional crosslinkers. EDC/NHS creates a

covalent bond between carboxyl groups (-COOH) and protein NH₂ groups with many advantages such as high binding efficiency, excellent biocompatibility and reactions can be done at room temperature at physiologic pH [95, 99-101].

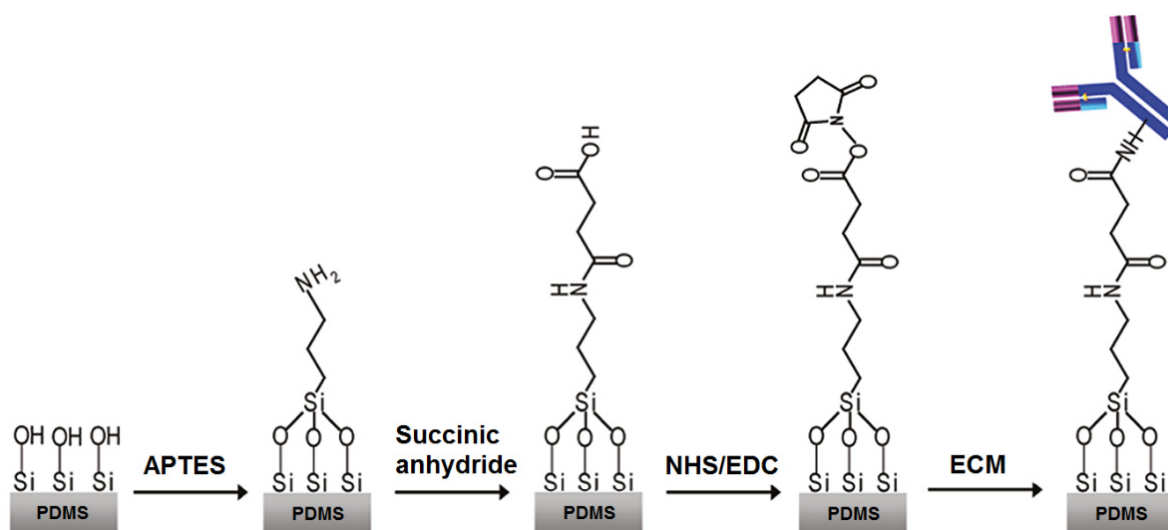


Figure 4.18. Schematic illustration of EDC/NHS coupling.

The following methodology is adapted from the investigation of Kim et al [95] and its illustrated in Figure 4.18. During all the procedure, reactions were performed at room temperature and the micropillar surface was kept always wet to avoid collapsing of pillars due to evaporation forces. Primary amine groups (NH₂) were introduced to the oxidised PDMS surface by incubation in a solution of 10% APTES in ethanol for 1 hour followed by rinses in ethanol and SDW thrice. These primary amine groups were then converted into carboxyl groups (-COOH) by submersion in a solution of PBS containing 5 mg/ml succinic anhydride and 5% of DMSO following rinses in PBS and SDW thrice.

To activate the carboxyl groups and create a link between them and the NH₂ groups from the ECM protein, devices were incubated for 1 hour in a PBS solution containing 0.1 M EDC and 0.2 M NHS. These concentrations were selected according to Wang et al [100] study, he demonstrated that these are the optimal concentrations for EDC/NHS activation. It is advised to prepare the EDC/NHS solution just before use because NHS quickly hydrolyse in aqueous solutions [99, 100]. Devices are then washed with PBS and SDW thrice prior incubation of 40 µl ECM protein for 30 min.

4.3.7.1 EDC/NHS functionalization results

Common methods to check availability of surface functional groups are electron microscopy (EM) and AFM. Nevertheless, they cannot quantify or validate these

functional groups. Other techniques such as x-ray photoelectron spectroscopy (XPS) and surface plasmon resonance (SPR) provide chemical properties to validate these functional groups; however, they are expensive, time-consuming and not often available in any laboratory. Thus, a quick, feasible, reliable and cost-effective method to quantify and validate these functional groups is helpful [102].

Here, we use a method created by Rushworth et al [102] at the University of Leeds, called midland blotting. This method can quantify and validate functional groups, bioreceptors and bound analytes in every step of the construction of a biosensor. Furthermore, it is rapid, cheap and allows faster optimization of the biosensor surface. It is based in the well-known western blotting procedure that use chemiluminescence to quantify proteins. This procedure consists in the attachment of horseradish peroxidase (HRP) to a target group; then, the addition of the enhanced chemiluminescence solution (ECL) reacts with the HRP emitting light. ECL is an enhanced luminol-based chemiluminescent solution for the detection HRP which catalyses the oxidation of luminol into a reagent which emits light. The light signal is proportional to the quantity of bound HRP. Figure 4.19 shows a schematic overview of the process.

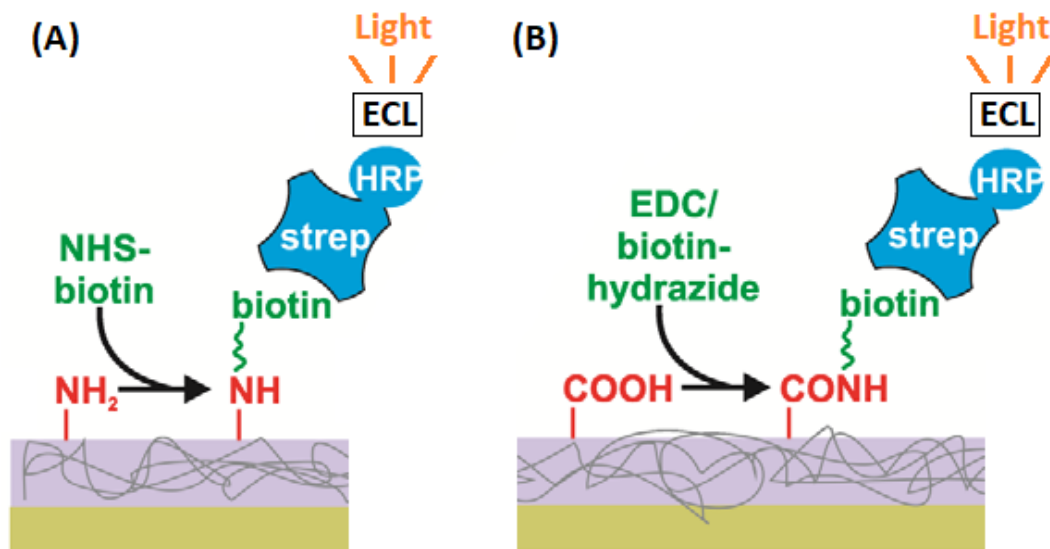


Figure 4.19. Midland blotting overview. Target groups (A) NH_2 (B) COOH [102].

The following methodology was performed at room temperature and within sealed humidified petri dishes to avoid evaporation of the solutions. PDMS micropillar devices were always kept wet to avoid pillar collapsing; therefore, drying steps from the original method were omitted. We use this method to validate the functional groups created

during every step of our previous EDC/NHS functionalization. This means that experiments were carried out: one for NH₂ groups after coating with APTES and then validation of -COOH groups after EDC/NHS functionalization.

To detect NH₂, a drop of 50 µl of PBS containing 4 mg/ml of NHS-Biotin and 20% DMSO was incubated in the micropillar surface for 30 min to bind biotin to the primary amine groups. Devices were then rinsed five times in 0.1% Tween 20 in PBS and then once with PBS followed by incubation of 50 µl of 1 µg/ml HRP-Streptavidin for 30 min. The streptavidin binds to the biotin from the previous step, leaving the HRP open to the surface to react with the ECL solution.

To detect COOH groups, a drop of 50 µl of PBS containing 1.25 mM Biotin Hydrazide and 5 mM EDC and 10% of DMSO was incubated in the micropillar surface for 1 hour to bind biotin to the carboxyl groups. Devices were then rinsed and incubated with HRP-Streptavidin as previously described for NH₂ detection.

For both experiments, samples were washed five times in 0.1% Tween 20 in PBS and then once with PBS prior adding 50 µl of ECL solution on the devices. Then, pictures of the chemiluminescence were acquired after 1 min using a G: BOX gel system. For all the measurements, control samples were used to demonstrate that attachment was through chemisorption rather than physisorption.

Finally, images were processed using the Miller [103] methodology in ImageJ software. This methodology consists in obtaining histograms of the signal intensity and then calculating a relative density to quantify the ECL strength signal. For better viewing, chemiluminescence and brightfield images were overlapped where green colour was used to aid viewing of the chemiluminescence areas.

Results for NH₂ functional groups are presented in [Figure 4.20](#), the signal from the APTES treated sample was around 6 times stronger than the control sample. This means that the treated sample successfully linked to the HRP and consequently it was demonstrated that primary amine groups were available all over the surface and they were functional.

The control sample showed a small amount of chemiluminescence; even though that control sample did not have any NH₂ groups. This may be due to tiny amounts of non-specific adsorption of either streptavidin and/or biotin during the midland blotting procedure. Consequently, more control samples must be implemented to know the

origin of this non-specific adsorption. These extra controls were implemented during validation of -COOH groups

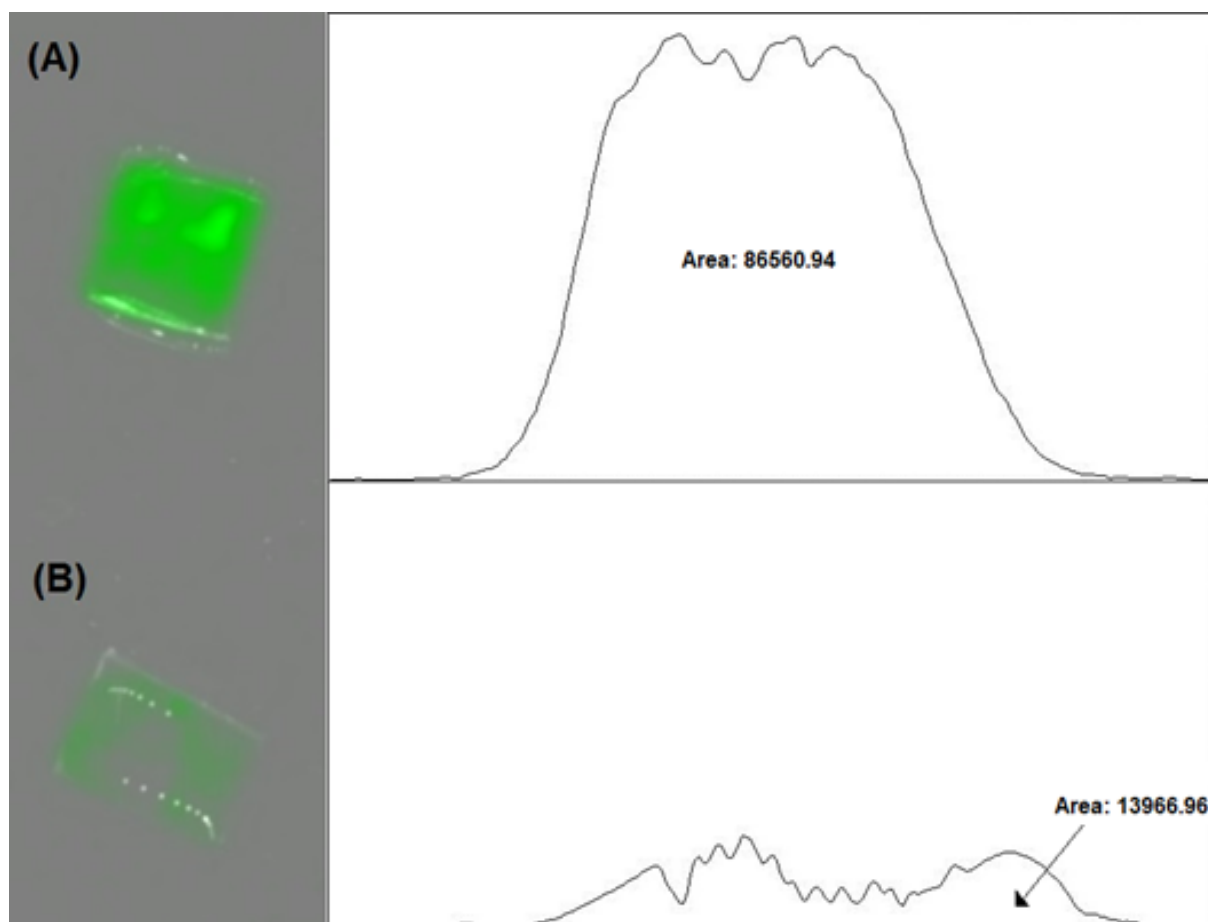


Figure 4.20. Chemiluminescence of NH₂ groups using Midland blotting procedure in PDMS micropillars. (A) APTES Treated (B) APTES untreated.

.For this experiment two samples (A and B) were functionalized with -COOH groups and 2 samples (C and D) were used as a control to ascertain whether biotin or streptavidin was adsorbing to the surface. The control sample (C) undergo the full midland blotting procedure; this means that layers of Biotin and Streptavidin were applied. The control sample (D) had only the Streptavidin-EDC layer. Results for COOH functional groups are presented in [Figure 4.21](#).

There was not much difference in the ECL signal between samples (C) and (D) and therefore, it was concluded that streptavidin was adsorbing in a small amount. This small non-specific adsorption was not relevant because samples (A) and (B) had 6-7 times higher ECL signal than control samples (C) and (D). This validates that carboxyl groups from EDC/NHS treated samples successfully linked to the HRP.

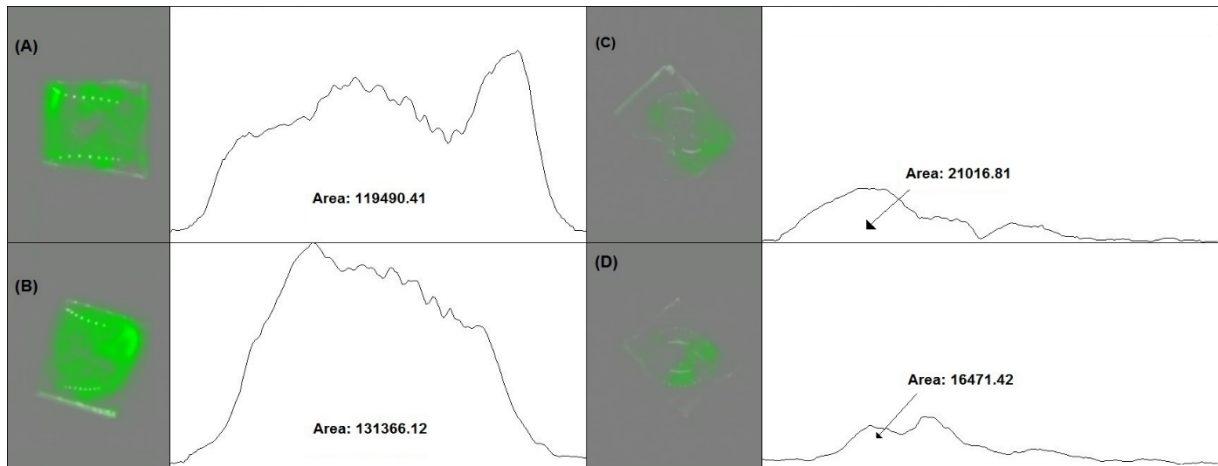


Figure 4.21. Midland blotting validation for carboxyl groups. (A) and (B) were functionalized samples with EDC/NHS. (C) and (D) were non-functionalized control samples. (D) without adding Biotin during Midland blotting procedure.

The presence of carboxyl groups in the surface was validated and then confocal microscope images of devices with the ECM protein were acquired, see Figure 4.22. Devices presented a uniform coating with no protein between pillars. Even though that fluorescent signal was not as strong as previous methods, this method achieved good repeatability of 90% of successful samples. These results prove that this methodology is the most reliable method to coat micropillar devices.

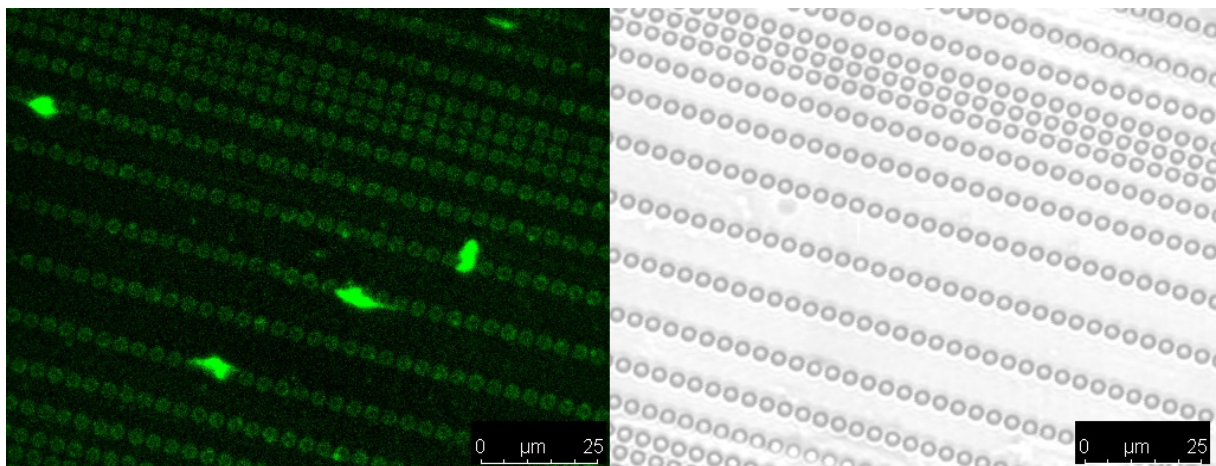


Figure 4.22. Confocal microscope image of ECM protein in EDC/NHS functionalized devices. (left) fluorescent (right) brightfield.

4.4 Summary

This chapter presented a protocol to prepare labelled ECM protein for cell migration studies with the main purpose of maximising protein adsorption to PDMS surfaces via hydrophobic and electrostatic interactions. In total 5 ECM protein functionalization

methods were studied, three of them by means of physisorption and two by chemisorption. The reliability of these methodologies was evaluated according to his repeatability to obtain a uniform coating rather than fluorescent signal strength.

The most common methodology to coat micropillar surfaces was first evaluated, this is the microcontact printing technique. Benefits of this technique are rapid methodology and the ability to be performed in any lab because it does not need specialised equipment or vacuum conditions. The drawback is the difficulty to achieve a uniform coating that is suspected to be because of non-conformal contact between stamp and micropillar surface.

The second evaluated methodology was a novel variation of microcontact printing technique by using a glass stamp rather than a PDMS stamp. Positive outcomes of this technique are a superior conformal contact between stamp and micropillar surface and strong fluorescent signal. The drawbacks are the addition of several steps to adequate the glass stamps to transfer ECM protein and that this method stopped working for unknown reasons.

The third technique to functionalize via physisorption is the silane method. The substrate was coated with a silane to increase its contact angle to 120° , then a drop of ECM protein solution was deposited and flattened with a coverslip. Hydrophobic interactions cause the protein to adsorb to the micropillars. This procedure achieved the strongest fluorescent signal of the studied methodologies. The drawback was the requirement to perform sonication to eliminate undesired protein “bridges” between pillars. This sonication may cause protein denaturation.

Two chemisorption methods to create covalent bonds were studied. These methodologies use a crosslinker to create bonds between primary amine groups from the ECM protein and the substrate. Both methodologies had the lowest fluorescent signal of the studied methodologies, yet the fluorescent signal strength was acceptable. The former used glutaraldehyde crosslinker with the benefit of coating only the micropillar tips, but nevertheless, some areas remained uncoated due to protein self-crosslinking. The latter is the EDC/NHS crosslinker which achieved a uniform coating all over the substrate surface with the benefits of a success rate of 90% of the samples.

Among the findings from this chapter, the protein should be negatively charged in order to improve its adhesion to a PDMS substrate. Moreover, the techniques provided in this thesis to coat PDMS micropillar tips in this chapter were proven to be more

effective than the traditional micro printing technique. The novel adaptation of the printing technique initially achieved optimal results in terms of uniform coating and strong fluorescent signal, and it needs to be studied more in depth to improve the repeatability of this method which suddenly stopped working. Silane methodology was proven to be a feasible procedure with strong fluorescent signal and uniform coating; however, the repeatability was not satisfactory. The chemical procedure using ECL/NHS coupling method achieved good repeatability of 90% of successful samples with an acceptable fluorescent signal; consequently, this method was selected to functionalize our PDMS devices for cell migration studies.

Chapter 5. Cell migration studies using PDMS micropillar devices

5.1 Introduction

The following chapter includes the experimental work carried out in the Newcastle Institute of Cancer Research facilities (NICR) after the devices were functionalized which includes cell culture, video acquisition and data analysis. The aim of this section is to successfully grow cells in our micropillar devices, to obtain videos of migrating cells, to process these videos to measure micropillar deflections and the corresponding forces caused by the migrating cell. These videos were processed using a novel customised MATLAB code and noise from raw data was successfully removed. Conclusions about how forces can be used to predict cell migration were exposed. All reagents were purchased from Sigma Aldrich unless otherwise stated.

5.2 Materials and methods

This section describes the methods used to study cell migration using PDMS micropillar devices, all reagents were purchased from Sigma-Aldrich (UK) unless otherwise is stated.

5.2.1 Tissue culture preparation

After the device was fabricated and functionalized with the ECM protein, epithelial cancerous cell lines A549 (lung cancer), NCI-H226 (lung cancer - pleura) and fibroblasts (HDF) were cultured in the micropillar devices. Tissue culture procedures were performed in a class II laminar flow hood that was cleaned with 70% ethanol. A549 cell lines were cultivated in a cell culture flask using RPMI 1640 medium and NCI-H226 and HDF cell lines in Dulbecco's modified eagle medium (DMEM) medium. Culture mediums were supplemented containing 10% foetal bovine serum, supplemented with 10 ml/L of penicillin-streptomycin antibiotic solution (10000 units penicillin and 10 mg streptomycin per ml) and 2.05 mM L-glutamine. Cells were then incubated using 5% CO₂ at 37° until 70-80% of confluency was achieved.

The following methodology was used to passage cells. The medium was removed and then cells were washed with 5 ml of PBS. Cells were then detached using trypsin-EDTA solution and left to incubate for 3-5 min with occasional shaking, they were ready when at least 90% of cells were detached. Next, 7 ml of RPMI medium was added to neutralise the solution and prevent cellular digestion. Then, the solution was

transferred to a 20 ml universal tube where a small aliquot of approximately 20 μl was removed to calculate cell density.

The remaining cells were spun in a centrifuge (1500 RPM) for 5 minutes to produce a cell pellet followed by removal of the supernatant. The cell pellet was then re-suspended in 1 ml of medium. Finally, a small quantity of the re-suspended solution was pipetted into an autoclaved coverslip cell chamber containing the micropillar device facing up. The medium was then added by a corresponding quantity to obtain a cell density between 1×10^5 - 1×10^6 cells/ml. Cell incubation time vary according to the cell line and may vary for each experiment; therefore, cells were checked with a brightfield microscope until cells start to spread. This cell chamber was purchased from AirekaCells and it's made of surgical stainless steel, top and bottom layer were sealed with conventional glass coverslips.

5.2.2 Video acquisition

Experiments were carried out in an SPE Leica inverted confocal microscope owned by the Bio-imaging unit within the NICR facilities. This microscope has its own incubator chamber making it ideal for live-cell imaging.

Cells attached to the PDMS devices and started to spread around 1-3 days after initial incubation. Micropillar devices were flipped face down due to the inverted configuration of the microscope. A schematic view of the set up for the experiments is presented in Figure 5.1.

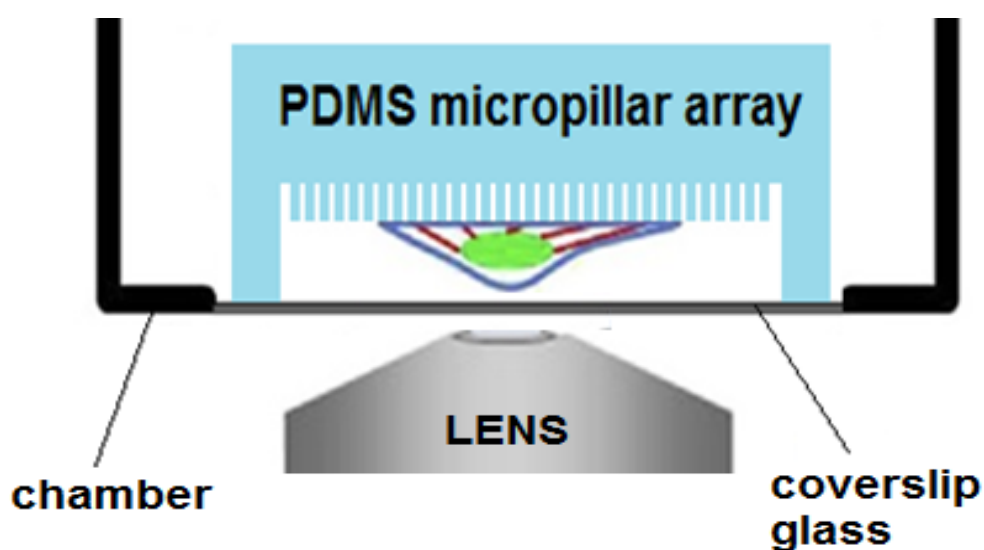


Figure 5.1. Schematic view of experimental set-up in an inverted microscope. PDMS micropillar devices were placed upside down in a metallic chamber with a coverslip glass bottom.

Microscope parameters were optimized because it was seen that a high scan speed accelerates the photobleaching effect; additional to this, the laser power was kept as low as possible to avoid damaging the cell. These optimized settings were 800 Hz scan speed and 17% laser power excitation for FITC (488 nm). Videos were captured overnight and converted to *.avi file to be processed in MATLAB.

5.2.3 Data analysis

This section presents a novel MATLAB code to process cell migration videos to obtain forces exerted by the cell in every pillar and frame by frame. This code stores each video frame as an image in a variable, convert frames to grayscale, detect coordinates of circular objects in every frame, link detected circular objects on every frame to the previous one, calculate the displacement of every pillar over time, correct noise from measurements and save results in an excel file. The code has the option to generate an image of a selected frame which shows the detected pillars. A video from Yamada Lab [104] of an MDCK migrating cell was used to test the code during its development, an example is presented in [Figure 5.2](#).

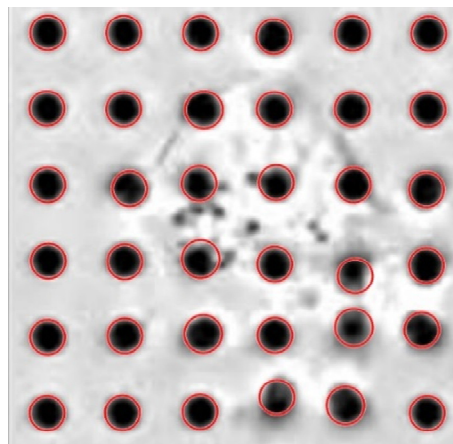


Figure 5.2. MDCK cell migration video processed in MATLAB [104].

Our customised code is based on the *imfindcircles* function from MATLAB and it has three initial parameters that must be manually entered by the user. These inputs are pixel/ μm conversion rate, range of micropillar diameter in pixels and detection sensitivity base from the first frame. The user must open the first image and measure the diameter of one pillar in pixels, the range of the pillar diameter will be ± 5 of the measured value. Pixel/ μm rate was calculated by dividing the image width in pixels by the width in μm obtained from the confocal microscopy software. Detection sensitivity base was selected by running the code on the first frame only, while the option to

illustrate the pillar detection was activated, this step requires the user to visually check if all and only the PDMS micropillars were detected.

The code will firstly use these parameters to compare the number of detected pillars on every frame versus the first frame. If the processing frame has equal circular features, the coordinates were then stored and linked to the previous frame. If it has fewer circular features than the first frame, the code will gradually increase the sensitivity detection base by 1% until it equals the first frame. On the other hand, if it has more circular features, the sensitivity was gradually decreased by 1%. Once every frame has the same quantity of circular features, the code computes the magnitude of the displacement and store it in a variable. The code will finally save the coordinates of each frame, a table containing the magnitude of displacement over time. Then, these displacements were multiplied by the stiffness 155.969 nN/ μm previously calculated in [section 3.2.1](#) to obtain the corresponding forces and exported to an excel file (.xlsx). The full code is presented as follows. Green text after the '%' symbol is the explanation of every step and input variables are in red colour:

```
%Read the video file and store it as 'obj' variable
obj = VideoReader('XXXX.avi');

%Count video frames and store it as 'frame' variable
numfiles = 0;
while hasFrame(obj)
    readFrame(obj);
    numfiles = numfiles + 1;
end

%Crop every frame to the desired area and store it in a cell called mydata.
for b = 1:numfiles;
    mydata{b} = read(obj,b);
    mydata{b} = imcrop(mydata{b},[X0 Y0 width height]);
    mydata{b} = imresize(mydata{b},3);
end

%Apply imfindcircles function to the first frame. This will detect circular features in the first
frame and store it in a variable called 'centres'. User must manually add the range of radius
to be calculated (rmin and rmax) and the sensitivity (S).
rmin= xxx; rmax= xxx ; S= xxx;

[centres{1}, radii{1}] = imfindcircles (mydata{1},[rmin rmax], 'ObjectPolarity', 'bright',
'Sensitivity', S, 'Method', 'TwoStage');

%calculating distance to origin axis of every pillar in the first frame to be used only to sort the
pillars according to its proximity to the origin axis.
[magnitude{1}] = (centres{1}(:,1).^2 + centres{1}(:,2).^2).^0.5;

%adding the calculated distance to the 'centres' matrix
centres{1}(:,3)=magnitude{1};
centres{1}(:,4)=radii{1};
```

%repeat the same procedure to the remaining frames. If current the frame has more pillars than frame#1 the sensitivity 'S' is increased by 1%, if it has fewer pillars the sensitivity 'S' is decreased by 1%. Both scenarios stop when the number of pillars of the current frame is equal to the first frame

```

for b = 2:numfiles
    for x=S:S/100:0.99
        [centres{b}, radii{b}]=imfindcircles(mydata{b},[rmin rmax],
            'ObjectPolarity','dark','Sensitivity', x);

        [magnitude{b}] = (centres{b}(:,1).^2 + centres{b}(:,2).^2).^0.5;
        centres{b}(:,3)=magnitude{b};
        centres{b}(:,4)=radii{b};
        if length(centres{1}) == length (centres{b})
            break
        end
    end
    if length (centres{b})~=length(centres{1})
        for x=S:-S/100:0.01
            [centres{b}, radii{b}]=imfindcircles(mydata{b},[rmin rmax],
                'ObjectPolarity','dark','Sensitivity',S);

            [magnitude{b}]=(centres{b}(:,1).^2+
                centres{b}(:,2).^2).^0.5;

            centres{b}(:,3)=magnitude{b};
            centres{b}(:,4)=radii{b};
            if length(centres{1}) == length (centres{b})
                break
            end
        end
    end
end
end
end

```

% SORT pillars according to its distance to the origin axis

```

for c = 1:numfiles
    [~, index] = sort(centres{c}(:,3),'descend');
    centres{c} = centres{c}(index, :);
    radii{c} = radii{c}(index, :);
end

```

% Link pillar centre coordinates of every frame match with the previous frame.

```

for d= 2:numfiles
    m=1;
    while m<100
        for e = 1:length(centres{d})-1
            if (((centres{d}(e,1)-centres{d-1}(e,1)).^2 + (centres{d}(e,2)-
                centres{d-1}(e,2)).^2).^0.5) >= max(radii{d})
                centres{d}([e e+1],1) = centres{d}([e+1 e],1);
                centres{d}([e e+1],2) = centres{d}([e+1 e],2);
                centres{d}([e e+1],3) = centres{d}([e+1 e],3);
                centres{d}([e e+1],4) = centres{d}([e+1 e],4);
            end
        end
        end
        for f = length(centres{d}):-1:2
            if (((centres{d}(f,1)-centres{d-1}(f,1)).^2 + (centres{d}(f,2)

```

```

-centres{d-1}(f,2)).^2).^0.5) >= max(radii{d})
    centres{d}([f f-1],1) = centres{d}([f-1 f],1);
    centres{d}([f f-1],2) = centres{d}([f-1 f],2);
    centres{d}([f f-1],3) = centres{d}([f-1 f],3);
    centres{d}([f f-1],4) = centres{d}([f-1 f],4);

        end
    end

    m=m+1;
end

%store 'centres' variable in new 'pillar' cell. This cell contains the coordinates of each pillar in
every frame
numpillars=length(centres{1});
for x=1:numpillars
    for a=1:numfiles
        pillar{x}(a,:)=centres{a}(x,1:2);
    end
end

%Apply gaussian filter to correct noise
for x=1:numpillars
    gaussian{x}(:,1)=smoothdata(pillar{x}(:,1),'gaussian');
    gaussian{x}(:,2)=smoothdata(pillar{x}(:,2),'gaussian');
end

%Store the pixel to micrometre conversion ratio.
n=xx;

%Calculate the displacement between the current and previous frame on every pillar and
every frame.
for g= 1:pillars
    for a=2:numfiles
        [gaussiandispl(a,g)]= (((gaussian{g}(a,2)-gaussian{g}(a-1,2)).^2 +
                                (gaussian{g}(a,1)-gaussian{g}(a-1,1)).^2).^0.5)/n;
    end
end

%Multiply the pillar displacement by the pillar stiffness to obtain the cell migration forces
Forces = 155.969.*gaussiandispl;

%Export the results to an excel file.
xlswrite ('forces.xlsx', Forces, 'Forces');

```

5.2.4 Noise removal

For illustration and explanatory purposes of our experiments, the first and last frame of one of our videos is used as an example, see [Figure 5.3](#). This video shows the migration of an A549 cell lying in micropillar devices with 3 μm diameter and 5 μm length, micropillars were numbered according to its distance to the right lower corner.

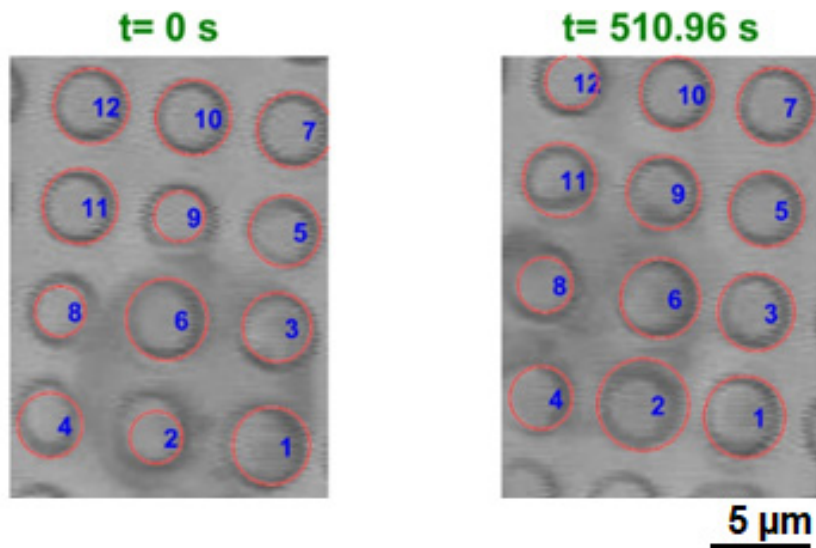


Figure 5.3. First and last frame from a video of a migrating A549 cell.

Plots of initial results on every video presented a distribution with noise all over the trend which and was identified as white Gaussian noise according to signal processing literature [105]. This noise was created by the algorithm used within the MATLAB *imfindcircles* function where detected circles from frames to frame were slightly not concentric and produced random peaks all over the data. This noise was eliminated by applying a Gaussian filter, as seen in Figure 5.4 of pillar 2 of the same video example.

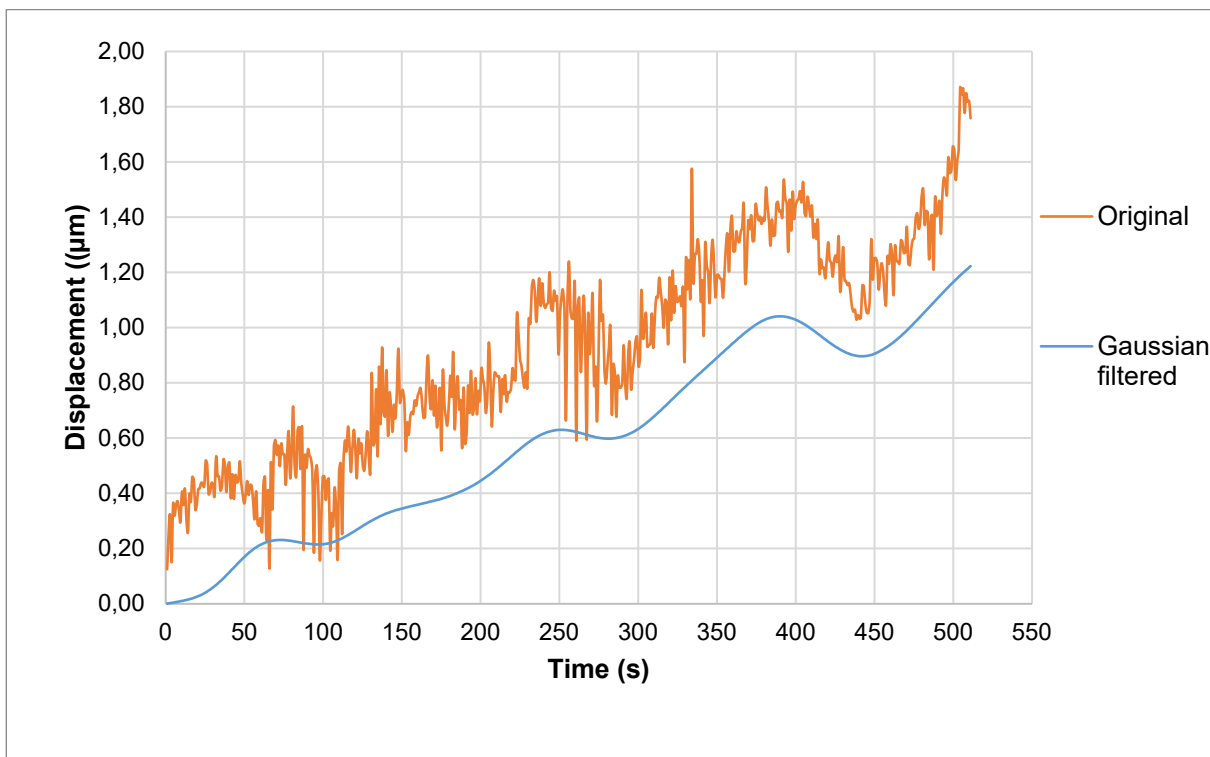


Figure 5.4. Original vs corrected noise by Gaussian filtering of pillar 2.

Additional to Gaussian white noise, data showed an increasing displacement all over the trend caused by a slight motion of the PDMS devices, as saw in [Figure 5.3](#). This motion is suspected to be because devices were slightly floating. Motion noise was removed by using micropillars which did not interact with a cell as control samples. Since all pillars from the video have the same motion, measurements from control samples reflect the effect of pure motion noise. The idea behind this is to subtract the pure motion noise from the samples. These controls were selected by inspecting their trends to find similarities and it was found that only pillar 7 and pillar 10 have similar paths and they were noticeably different to all other pillar trends, as seen in [Figure 5.5](#).

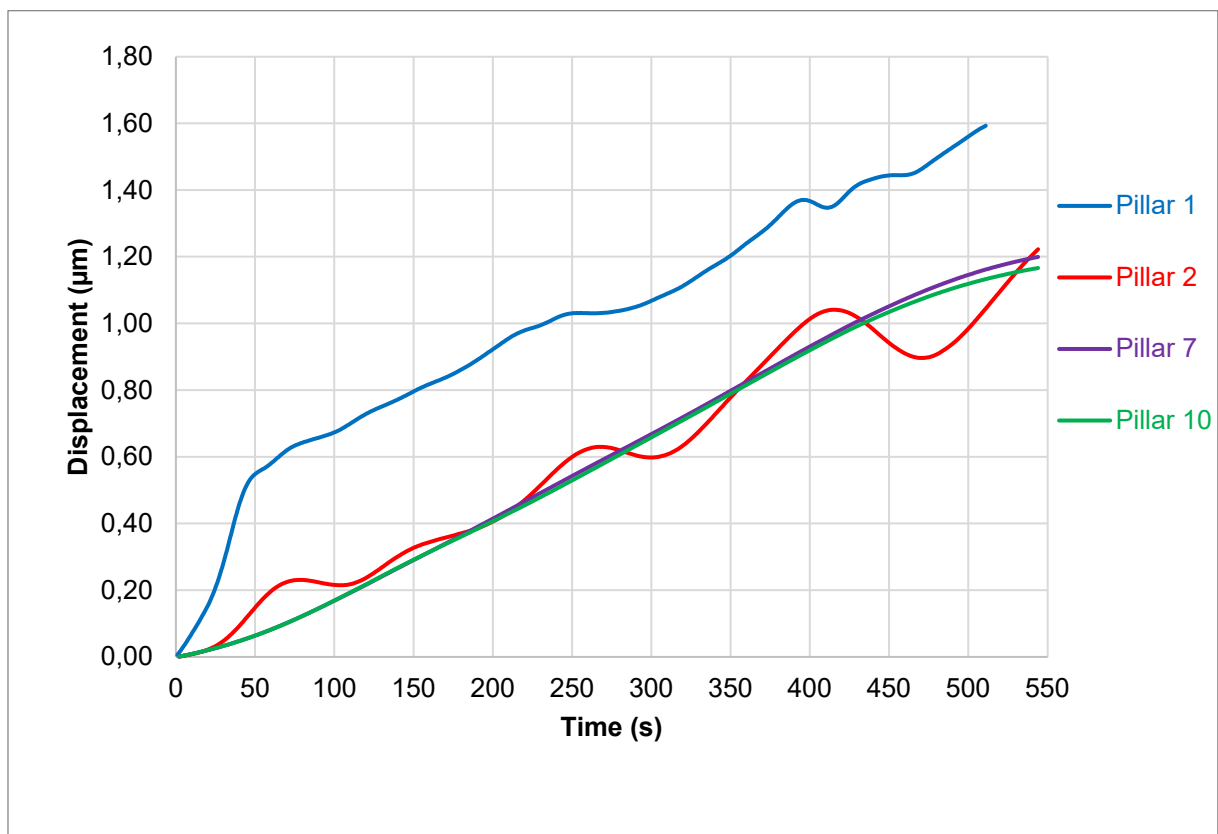


Figure 5.5. Displacement vs time plot. Pillar 7 and pillar 10 were control samples. Pillar 1 and pillar 2 were pillars deflected by A549 cells.

This visual control selection is not enough to prove that these pillars behave as controls because their medians and variance could be statistically different. To verify this, a Mann-Whitney U statistical test was performed, and it was found that medians and variances from control samples were not significantly different (p -value=0.94). Then to remove the motion noise, the average of control plots at every frame was subtracted from the micropillars who were in contact with a cell. This filtering was successful to remove this unexpected motion noise from our data, as seen in [Figure 5.6](#).

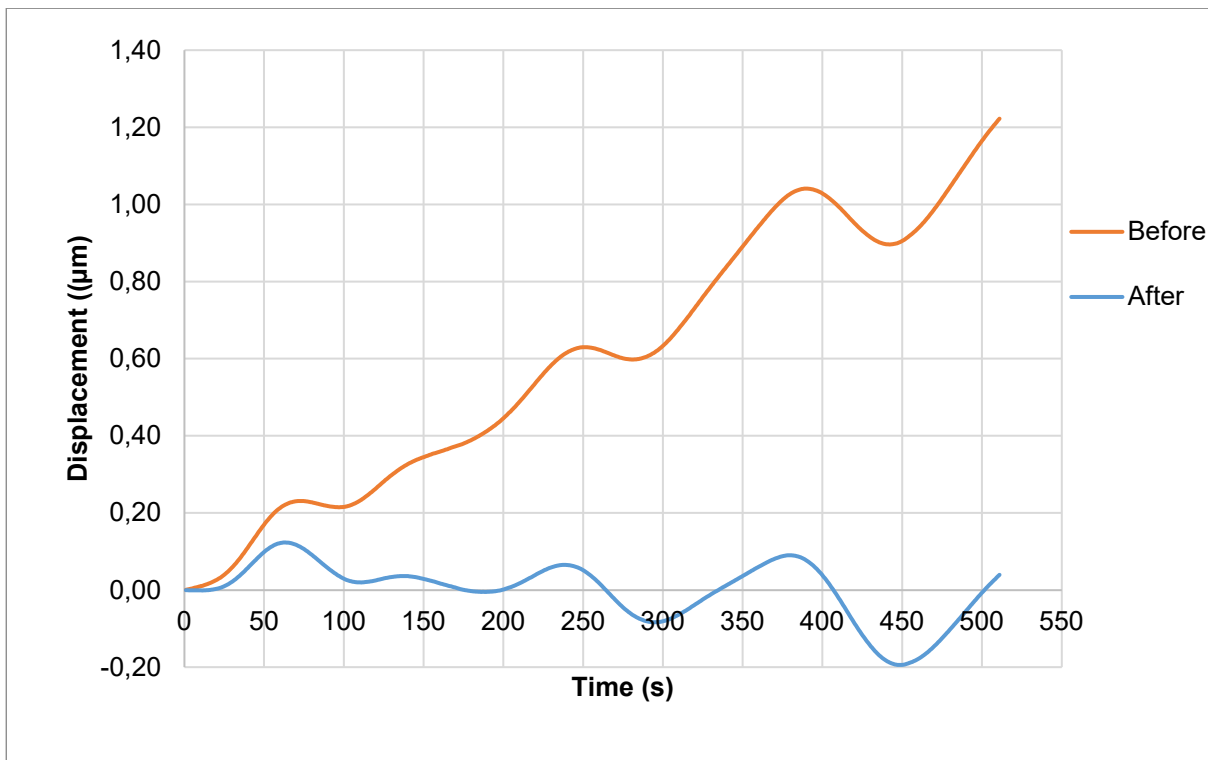


Figure 5.6. Removing motion noise from pillar 2 using control samples.

5.3 Results and discussion

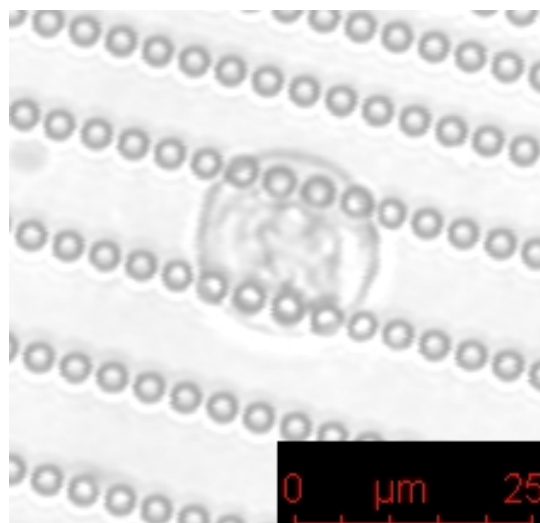


Figure 5.7. Cell lying in a micropillar device with pillars with 2 µm diameter and 5 µm length

Experiments were carried out using epithelial cancerous cell lines A549 (lung cancer), NCI-H226 (lung cancer - pleura) and fibroblasts (HDF) cell lines to test the reliability of our devices to measure migrating forces. It was seen that cells attached well to the micropillar devices and no cell sank between pillars even for devices with big space between micropillars, an example is shown in Figure 5.7. This proves that the ECM

protein coating was successful for cell attachment. In terms of cell motility, only micropillars devices with 3 μm diameter, 5 μm length and spaced by 3 μm promoted cell migration. This chapter presents the results of cells migrating in devices with these dimensions only.

For convenient explanatory purposes in this chapter, forces exerted by the cell that helps migration are called “pulling forces” and they are represented in every plot with positive magnitudes. On the other hand, forces which do not help migration are called “pushing forces” and they are represented in every plot as with negative values.

5.3.1 Cell migration of an epithelial A549 cell line

The following results correspond to the study of cell migration of an A549 cell which was the same cell used for the noise removal explanation, captions of cell migration are presented in Figure 5.8. In this analysis, pillar 7 and 10 were used as control samples for noise removal as previously described. Video length was 8 hours; however, only part of the video which shows migration is presented here.

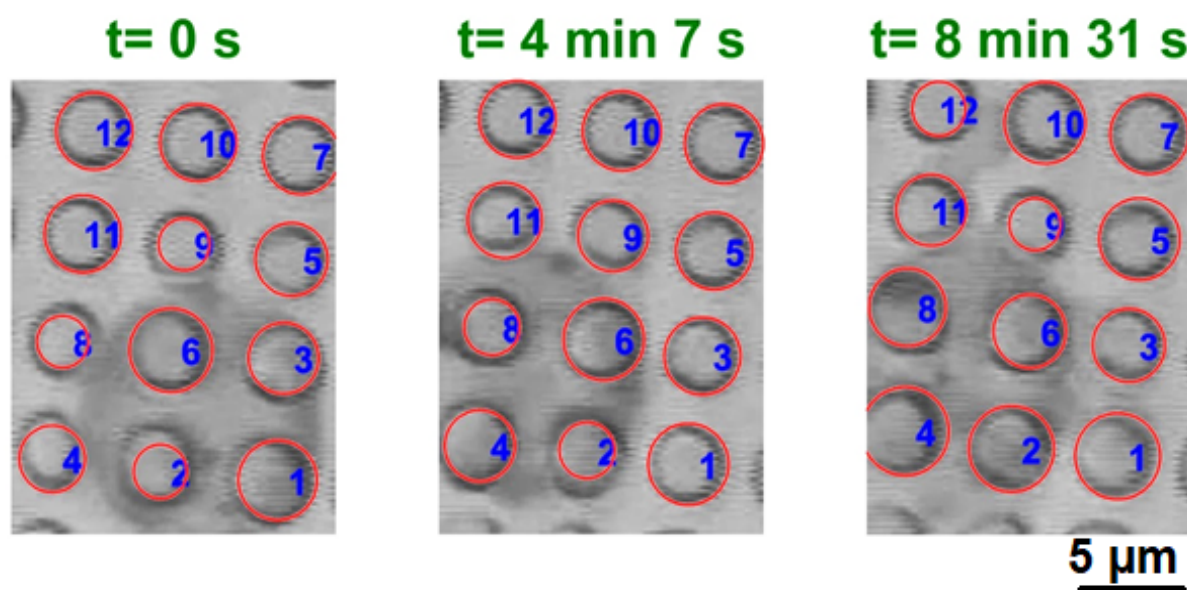


Figure 5.8. Two behaviours of a cell a migrating A549 cell in micropillar devices with 3 μm diameter and 5 μm length. Migration from (a) to (b) migration. Cell lamellipodium exploring the surrounding area from (b) to (c).

Overall, A549 cells exerted a maximum force of 79 nN and minimum force of -40 nN with an overall mode force of 1.01 nN on the micropillar devices. Mode forces were predominantly bigger in pillar 1 and 8 than other pillars with mode values of 54.05 nN and 47.52 nN respectively, as seen in the boxplots from Figure 5.9.

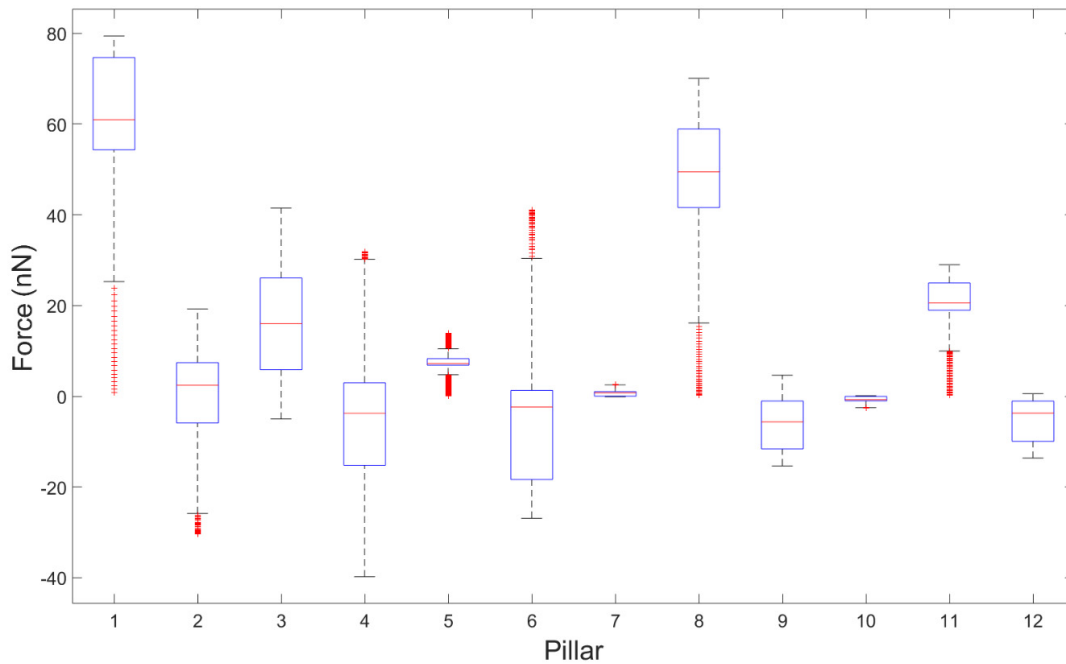


Figure 5.9. Boxplot of migration forces of an A549 cell. The central red line indicates the median, and the bottom and top edges of the box indicate the 25th and 75th percentiles, respectively. The whiskers extend to the most extreme data points not considered outliers, and the outliers are marked with a red '+' symbol.

The boxplot presents the distribution of forces on each pillar where the most predominant pulling forces were pillar 1, 3, 8 and 11 while pillars 2, 4 and 6 were mostly pushing forces. As expected, the distributions of forces in the control pillars 7 and 10 were near zero. Outliers are represented with a red cross which only represented less than 7% of the number of total forces on each pillar, this suggests that errors in this experimental data were minimal.

It was seen two cell behaviours in this micropillar array. The first behaviour was the migration of the front edge of the cell from pillar 2 and 6 to pillar 4 and 8 lasting 0 to 04:07 period, see [Figure 5.8 \(a-b\)](#). The second behaviour corresponds from 04:07 to 08:31 where the main behaviour was the cell exploring the surrounding area using its lamellipodium, [Figure 5.8 \(b-c\)](#). Forces involved in the most relevant micropillars from this section are presented in [Figure 5.10](#).

During the first behaviour, cell started with an aggressive movement by pulling back pillar 1 and 3 causing to move forward until the exerted forces reach a maximum force of 79 nN and 40 nN respectively at 01:14. During the same period, pillars 2 and 6 from the front edge were pulled back to aid this migration with maximum values of 16 nN

and 36 nN respectively. At the same time, the front of the cell quickly extends to pillar 4 and 8 and pulled them back to aid cell movement with a maximum force of 3 nN and 59 nN respectively in the first 2 min.

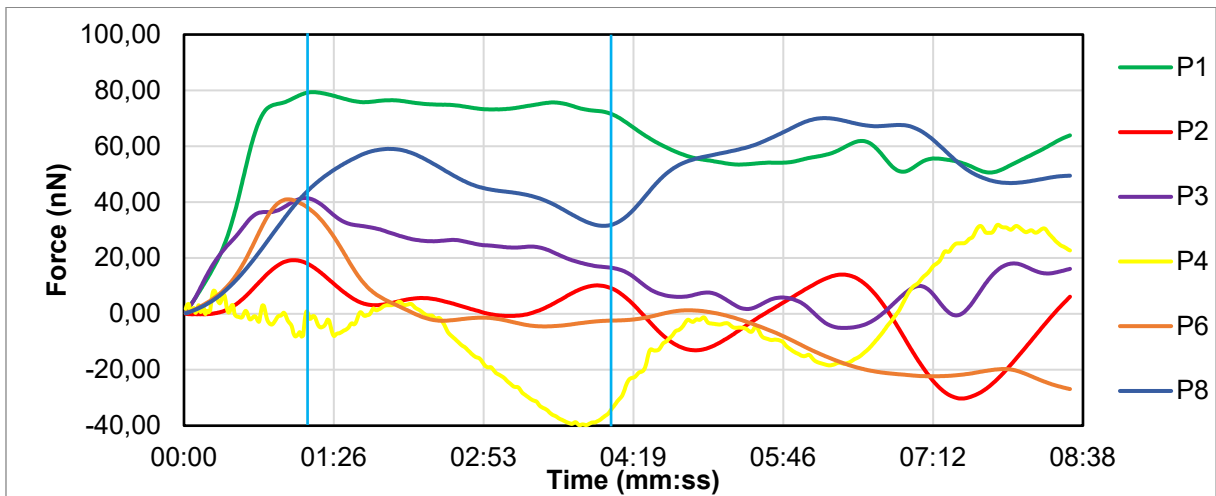


Figure 5.10. Force vs time plot of relevant micropillars during cell migration.

These findings suggest that forces were bigger in the rear edge of the cell rather than the front edge which is contradictory to Saez claims [31, 37]. Furthermore, cell started to turn to the right towards pillar 12 by exerting bigger forces in the front pillars from the right side (pillars 6 and 8) than the ones from the left side (2 and 4).

From the remaining period of this section (00:02-04:07) forces dropped to -33 nN in pillar 4, pillar 8 to 32 nN, pillar 2 to 8 nN, pillar 6 to -2 nN, pillar 1 slightly to 71 nN and pillar 3 dramatically to 16 nN. Surprisingly, forces from pillar 4 suggest that cell didn't use this pillar for migration; cell attached to it and then it was pushed due to the contractions of the body cell during migration causing magnitudes with negative values.

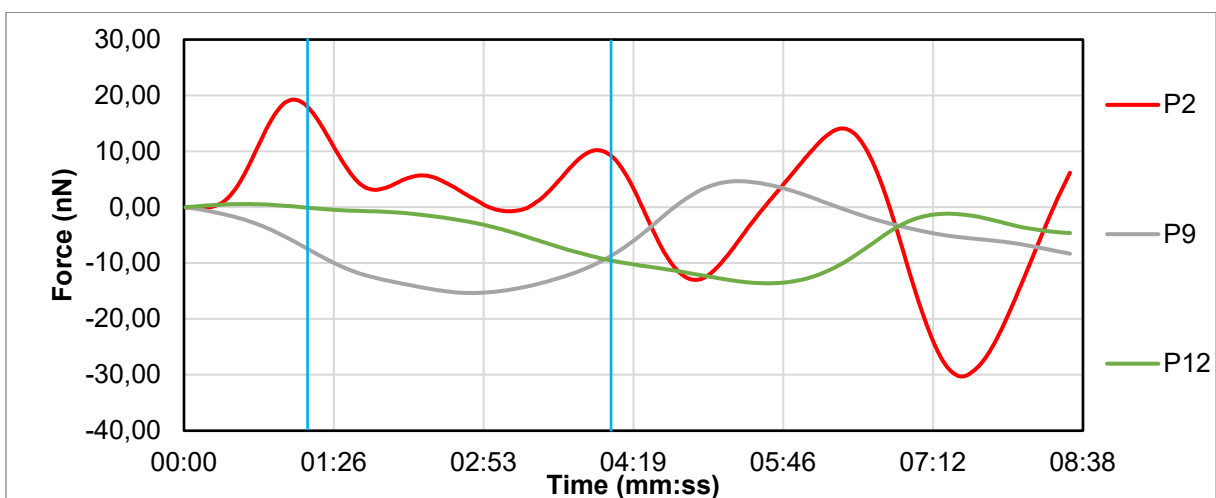


Figure 5.11. Forces in relevant micropillars in cell lamellipodium exploration.

The second behaviour from this video (04:07 – 08:31) covers the cell lamellipodium exploring the surrounding area to decide the new migration direction. At the beginning of this section, the front edge of the cell was standing in pillars 6 and 8 while the back of the cell was attached to pillars 2 and 6, as previously presented in [Figure 5.8 \(a-b\)](#). By inspecting at the forces from [Figure 5.11](#), cell extended its lamellipodium to explore the surrounding area. Cell mainly push pillar 12 for one and a half minutes until a force of -13 nN was reached, then it was pulled back until it reaches a force of -1 nN at 07:22 and finally it was pulled back again until the end of the video.

An interesting behaviour was the pushing and pulling exerted forces to pillar 2 at the back of the cell. From 04:07 s for 47 s, it was pushed reaching a force of -13 nN. Then, it anchors to the micropillar and starts to pull it back until a force of 14 nN was reached at 06:20. Next, the pillar was pushed again for 1 min and 10 s reaching a force of -30 nN. Finally, the pillar was pushed again until the end of the video reaching a force of 6.182 nN. It is concluded that these fluctuations between force directions in pillar 2 were consequences of the cell contractions when the cell was planning to stay on the pillar or to move to another one.

Regarding pillar 9, it was pushed from the period between 00:00 - 04:07 by the body of the cell and not by the lamellipodium; consequently, the plot shows negative forces during this period. The cell then anchors to pillar 9 and pulled it back until a force of 4 nN was reached at 05:21, for the remaining time of the video this pillar was pushed again.

It was uncertain the reason for the cell to stop migrating and it is concluded that cell could not find another pillar where it felt comfortable to step. However, a reason could be that the ECM protein functionalization was not uniform in the neighbour pillars and therefore, cell stop migrating.

5.3.2 Cell migration of an epithelial NCI-H226 cell line

Cell migration for epithelial cells NCI-H226 was observed during an interval of 35 min and 13 s. It is important to highlight that one pillar was missing due to PDMS residues in one orifice of the silicon mould, this issue was addressed in [section 3.1](#) This missing pillar did not stop cell migration where the cell extended its body to reach the next pillar instead of sinking in the gap created by the missing pillar. Migration started when the cell was lying in pillars 1,2,4 and 6 and then, the front part of the cell migrated to pillars 3,5 and 7, as seen in [Figure 5.12](#). Noise removal was performed using the same

methodology of A549 cells, with the exception that only pillar 8 from Figure 5.12 was used as a control sample.

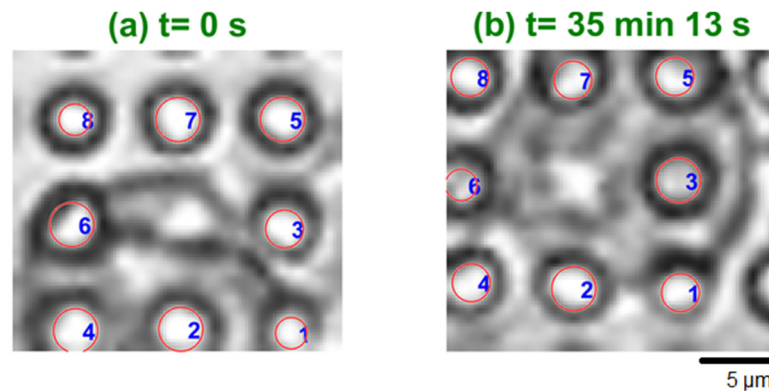


Figure 5.12. NCI-H226 cell migrating in micropillar device.

Boxplot from Figure 5.13 presents the distribution of forces on each micropillar where predominant pulling forces were pillar 1, 3 and 6 while pillars 2 and 4 were mostly pushing forces. This boxplot does not show outliers this means, that our experimental data was correct. Distribution of forces in pillar 8 was zero because this pillar was used as a control sample.

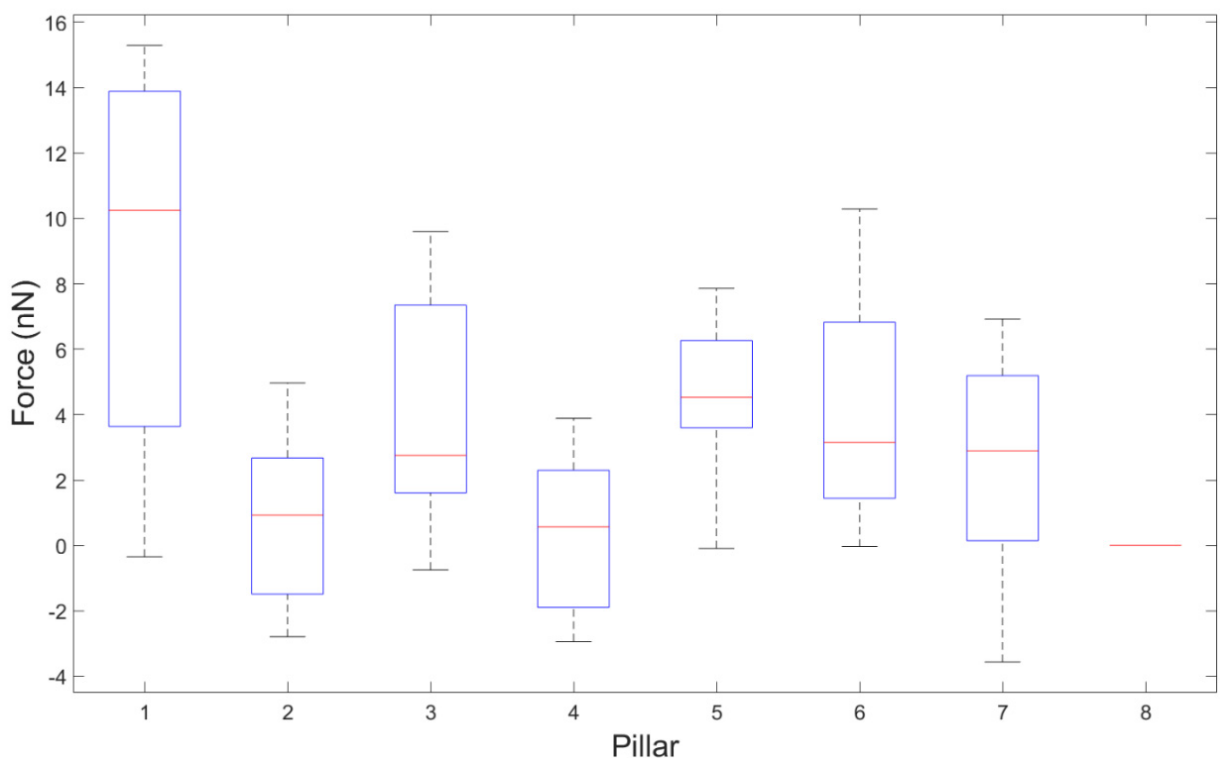


Figure 5.13. Boxplot of exerted forces of an NCI-H226 cell. On each box, the central red line indicates the median, and the bottom and top edges of the box indicate the 25th and 75th percentiles, respectively. The whiskers extend to the most extreme data points not considered outliers.

The maximum exerted force was seen in pillar 1 with a value of 15 nN while the minimum value was -3 nN in pillar 5 and the mode exerted force for the whole system was 1.05 nN. Cell migration was predominantly led by exerted forces in pillar 1 with a mode force of 13.26 nN, followed by pillar 3 and 6 with mode forces of 2.55 nN and 1.88 nN respectively. It was also seen that cell created negative forces on the pillars by pushing them as cell migrates, similar to the observed behaviour in A549 cell,

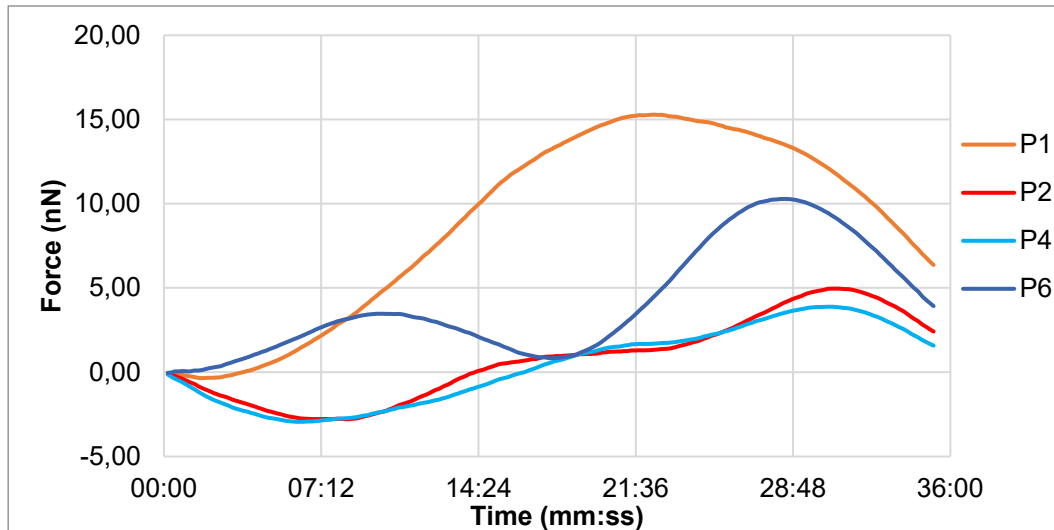


Figure 5.14. Force vs time plot of pillars 1,2,4 and 6 of NCI-H226 migrating cell.

Force vs time plot of pillars that initiated migration is illustrated in Figure 5.14. The cell started to exert a pulling increasing force in pillar 6 for 10 min until it reached 3 nN. At the same time, pillar 1 was pushed by the cell movement for 02:15 and then, cell started to pull this pillar with a force of 15 nN until 22:27 when the applied force gradually decreased to 6 nN at the end of the video. Also from the beginning of the video, pillars 2 and 4 were pushed by the body for 8:28 and 06:13 respectively; pillars then were pulled back with forces of 4 nN and 3 nN respectively until 30 min and 55 seconds and then both decreased until the end of the video to 2 nN and 1 nN respectively. Interestingly, cell interacted with these pillars almost simultaneously reflected in their similar trends with peaks and bottoms almost synchronized, as saw in Figure 5.14.

Furthermore, pillar 6 presented both increasing and decreasing forces after reaching the first peak of 3 nN at minute 10. The applied force felt for 7 minutes to a value of 1 nN, then it dramatically increased to a value of 10 nN at minute 28 and finally it decreased to 4 nN at the end of the video. This is suspected to be a consequence of the cell contracting its body, similar to the studied cell A549 from section 5.3.1

Regarding pillars 3,5 and 7 from [Figure 5.15](#); cell extended its body to reach pillar 5 at 2:04 and pillar 7 at 01:54; cell then pulled them back until reaching forces of 4 nN and 5 nN respectively at 11:24. This cell extension caused pillar 3 to be pushed until 03:17 when cell attached and pulled it back until reaching a force of 2 nN at 12:47. The rest of the cell behaviour in these pillars was contracting the body causing increasing and decreasing forces until the end of the video.

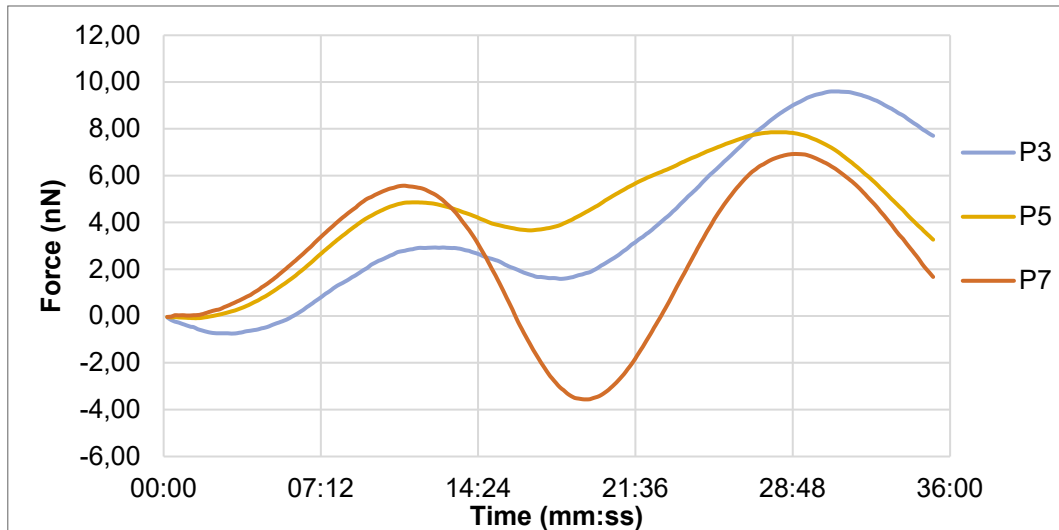


Figure 5.15. Force vs time plot of pillars 3,5 and 7 of NCI-H226 migrating cell.

5.3.3 Cell migration of a fibroblast HDF cell line

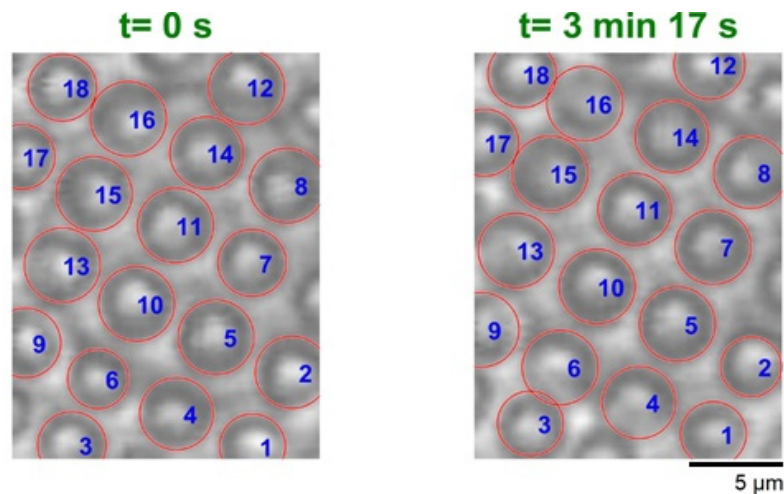


Figure 5.16. HDF cell migrating in a micropillar array.

This section presents to study of HDF fibroblasts of a 3 min video which showed little migration on the micropillar array, see [Figure 5.16](#). Noise removal was successfully performed using the same methodology previously explained in [section 5.2.4](#). The Mann-Whitney U statistical test was positive to confirm that pillars 1 and 17 can be used as control samples, p-value=0.94. the back of the cell was lying in pillars 8,12,14

and 16 while the front of the cell was in pillars 2,4,6 and 8. This cell generated maximal and minimal forces of 51 nN and -72 nN in pillar 13 and pillar 6 respectively with an overall mode force of 3.44 nN and a median force of 0.5 nN, as seen in the boxplot from [Figure 5.17](#).

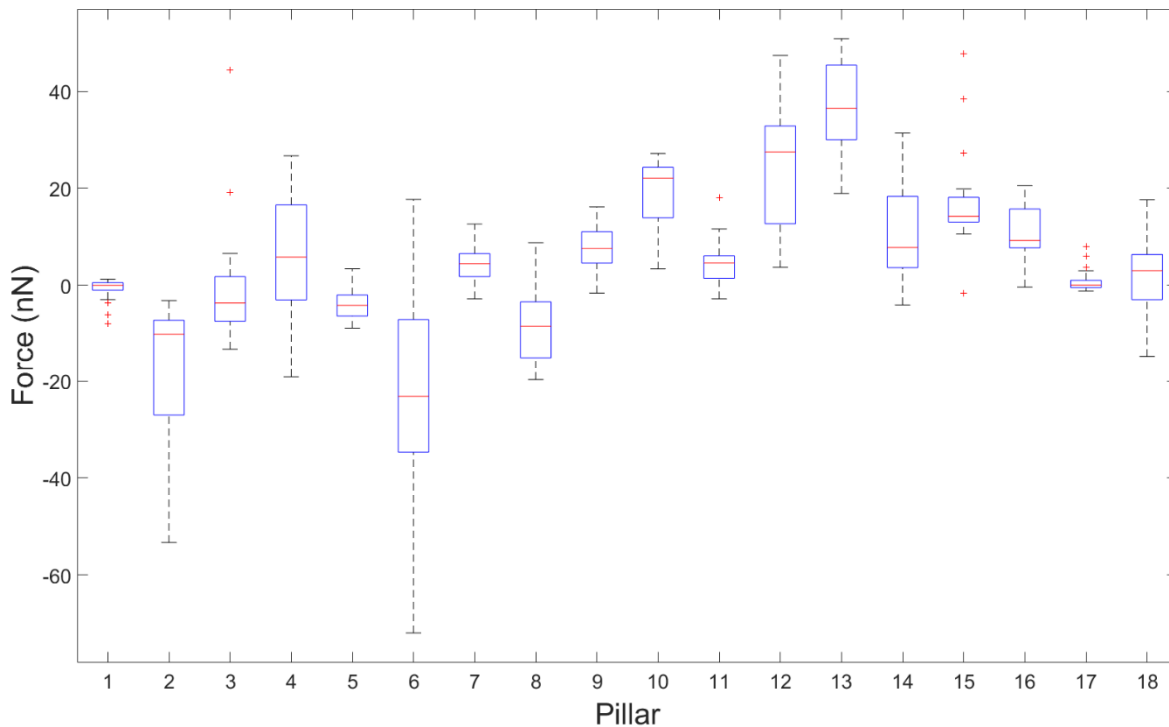


Figure 5.17. Boxplot of exerted forces of an HDF migrating cell. On each box, the central red line indicates the median, and the bottom and top edges of the box indicate the 25th and 75th percentiles, respectively. The whiskers extend to the most extreme data points not considered outliers, and the outliers are marked with a red '+' symbol.

The boxplot shows the distribution of forces on each pillar where the most predominant pulling forces were pillar 4, 12, and 13; in the other hand, pillars 2 and 6 were mostly pushing forces and control pillars 1 and 17 were null. The outliers were minimal in this experiment which represented less than 1% of the number of total forces on each pillar.

The main forces influencing migration were in pillar 13 from the front left side of the cell and pillar 12 at the back of the cell (middle) with mode force values of 37.50 nN and 24 nN respectively. Followed mode forces were pillars 2 (-11.20 nN), 4 (6 nN), 6 (-16.17 nN), 10 (23.52 nN), 15 (15.16 nN) and 16 (7.50 nN).

Force trends of pillars located at the front of the cell are illustrated in [Figure 5.18](#), they were the main contributors to cell migration during the first 52 seconds with exception of pillar 2 who was opposing to it. This means, that cell did not pull pillar 2 back and

instead, it was pushed by the body of the cell during the whole video with an opposing maximum force of -53 nN.

Pillar 6 then started to experience negative forces which opposed cell migration reaching a low peak of 71 nN at 02:35. Then, the cell starts to pull the pillar back until the end of the video. Pillar 4 was pushed by the body of the cell for the first 10 seconds and then it was pulled with an increasing force of 26 nN at 00:52, it was then experiencing a decreasing force as low as -19 nN at 02:46 where it started to pull again until the end of the video.

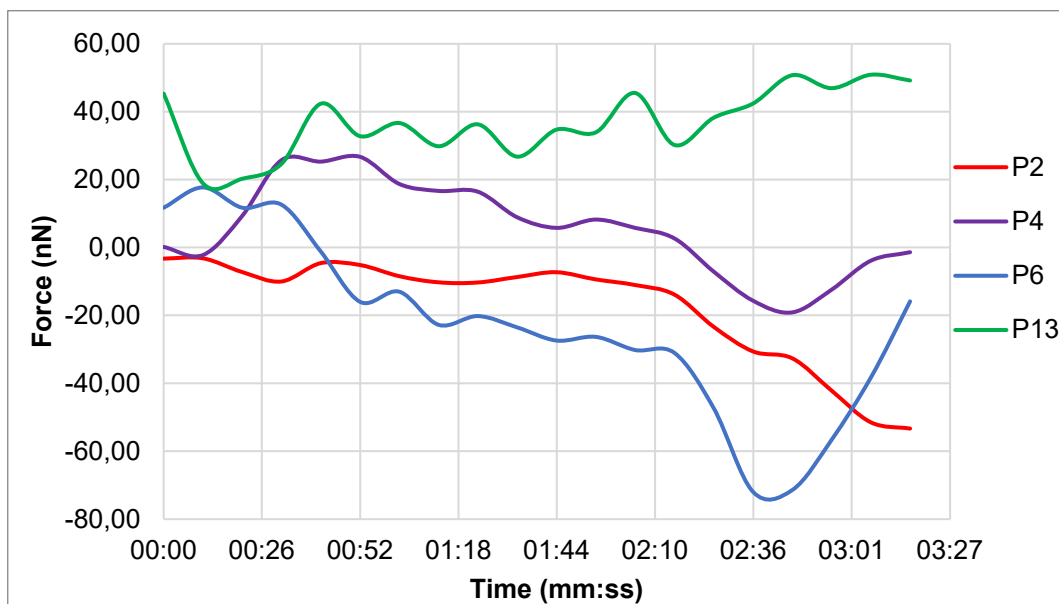


Figure 5.18. Force vs time plot of pillars 2,4, 6 and 13 of an HDF migrating cell.

Pillar 13 was the pillar experimenting the leading force during this study. At the beginning of the video, it was pushed for 10 seconds and then its force started to increase for the remaining time. It reached a maximum force of 50 nN at 03:06. This pillar experimented small periods of fluctuations of increasing and decreasing forces, probably caused by contractions of the body cell.

Most influencing forces from pillars at the centre and rear part of the cell are presented in Figure 5.19 and it shows that forces on these pillars contributed to cell migration, this means that all were in opposite direction to cell movement (positive in magnitude). Pillars 12 and 16 experienced increasing forces in most of their trend reaching maximum values of 47 nN 20 nN respectively at the end of the video.

Pillar 10 experienced fluctuations between increasing and decreasing forces. Pillar 10 force trend started by an increased for 10 seconds to a force value of 13 nN, it then decreased to 4 nN for another 10 seconds. Next, from to 00:21 to 00:52 increased to

23 nN, it then experienced a decrease for 10 seconds to 14 nN. Finally, the force trend increased to a maximum value of 27 nN at 02:04.

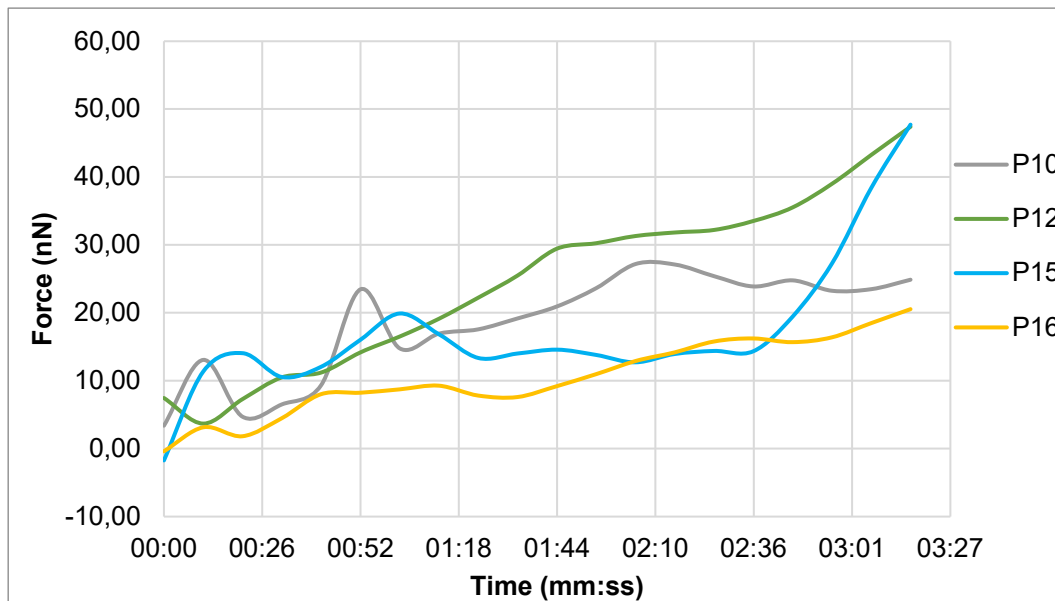


Figure 5.19. Force vs time plot of pillars 10,12, 15 and 16 of an HDF cell.

Likewise, pillar 16 experimented fluctuations of increasing and decreasing forces. Starting with an increase to 3 nN for 10 seconds and then it decreased to 2 nN in another 10 seconds period. Next, it increased for 20 seconds to a force of 8 nN followed by a slight increase to 9 nN at 01:13. Then, it increased to a maximum value of 20 nN at the end of the video.

It is noticeably seen that the most influences forces in cell migration were in the right side of the cell and it is concluded that cell will turn into that direction. The low overall median force of 0.5 nN was indicative that these micropillar dimensions cause little migration in HDF fibroblasts and therefore, different micropillar dimensions must be designed to study this type of cell line.

5.4 Summary

This chapter presented the experimental setup and the study of cell migration behaviour in HDF fibroblasts and epithelial cells A549 and NCI-H226 in micropillar devices with a stiffness of 155.969 nN/ μ m. This device was able to measure forces as high as 79 nN with a resolution of 0.01 nN. The noise was successfully removed from the signal and it was due to variations in micropillar centres detection, a better ECM protein functionalization could improve this issue.

It was seen that cells move forward by pulling certain pillars with direction opposite to cell migration. Attached focal adhesion points created a pushing effect in the remaining pillars; this pushing effect was in the same direction to cell migration. Mode forces in epithelial A549 and NCI-H226 cells were similar with an approximate value of 1 nN; however, they presented evident differences in migration times (8 min vs 36 min) and maximal local forces (60 nN vs 15 nN). The global median force in HDF fibroblast cells was 0.5 nN, this low median force of HDF cells is a consequence of the minimal migration and it suggests that micropillar devices with bigger stiffness must be designed for this type of cell. These findings in local forces, confirm that this device can provide useful information for cell migration studies in epithelial cells and can be used to detect a specific cell line.

Furthermore, this device offered a tool to predict cell migration direction. It was seen that cells exert bigger forces on the side where it was going to move next; as seen in NCI-H226 cell migration, where it turned to the left while HDF and A549 cells turned to the right. Sections that cell moved forward, pillars were pulled in the same direction. This was proved by the observations of the A549 lamellipodium, that forces were greater in the right side of the cell before it extends the lamellipodium in the same side to sense and decide a new path to move. This lamellipodium sensing mechanism was initiated by pushing several pillars before focal point attachment occurs; it pushes a pillar, then retracts and then the same procedure for another pillar until it chooses where to move next.

Increasing and decreasing fluctuations in the force trends were a consequence of cell contracting its body, it is suspected to be that cell was trying to change its migration direction and it is proposed to study in future work. Additionally, it is suggested to improve the ECM protein functionalization to ease the noise signal from measurements.

Chapter 6. Conclusion

This project highlighted the importance of studying cell mechanotransduction to improve the general understanding of the mechanisms behind cell metastasis with the aim to aid researchers in the development of tools and drugs to fight cancer. This thesis focused on how cell migration is affected specifically by the substrate topography and stiffness. A micropillar device was developed to perform cell migration studies in epithelial cells and fibroblasts. This device succeeded to provide a platform to researchers to study cell migration, by measuring local forces exerted by the cell in each micropillar. These local forces bent the micropillars and this deflection was measured with a microscope to calculate the corresponding force magnitude. Micropillar devices were made of PDMS and functionalized with fibronectin ECM protein.

A range of PDMS micropillar designs with 11 different arrangements and 3 cross-sectional areas were proposed. Micropillars designs were 5 μm long and had an estimated young modulus of 2 MPa according to the manufacturer's recipe. The calculated micropillar stiffness was 155.969 nN/ μm for the 3 μm circular pillar, 34.291 nN/ μm for the 2 μm circular pillar and 56.549 nN/ μm for the elliptical micropillar. Assumptions for theoretical deflection were based in the Timoshenko's beam theory instead of the Euler Bernoulli beam theory used by previous researchers, these assumptions were corroborated by the finite element analysis (FEA) with <2% error.

The 11 proposed micropillar arrangements were designed with the following rationale. Templates #1, #2 and #3 were meant to provide a micropillar device which had the same percentage of ECM protein all over the substrate to efficiently measure local migration forces. Templates were #4, #5 and #6 aimed to test the limits of the PDMS fabrication. Design #7 was designed to study how cells behave in elliptical micropillars which are close to each other and do not have the same percentage of ECM protein. Designs #8, #9, #10 and #11 aimed to provide a micropillar arrangement which is effective to confine cells to a specific area.

The micropillar device was fabricated by casting and demoulding from a silicon mould where problems with stiction were solved by applying a silane coat to the silicon surfaces. Collapsing pillars was another issue during micropillar fabrication which was eased by performing critical point drying (CPD). Final PDMS micropillar dimensions and arrangements were characterized with SEM and AFM instruments where AFM

measurements showed that pillars were not the same height within a range of 4 μm to 4.7 μm . This discrepancy in the pillar height led to assume a constant pillar length of 5 μm in every fabricated device. Devices were successfully manufactured except for designs #5 and #6 which presented collapsed pillars. The pillars in these designs collapsed in the areas where the distance between pillars was less than 3.5 μm .

Devices were functionalized with an extracellular matrix protein (ECM) to allow attachment of cells to the micropillar tips for efficient transmission of the cell forces to each micropillar. The used ECM protein in this thesis was Fibronectin and it was prepared with conditions to maximise protein adsorption to the PDMS surfaces. A range of different methods was addressed and tested to provide the most robust method to coat PDMS micropillar devices.

The first studied method was the reverse microprinting technique which is the most widely used method among researchers due to its low cost and feasibility. This method was not successful to achieve a uniform coating. Consequently, this method was modified by changing the stamp material to glass instead of a PDMS and then a uniform coating was achieved with a high fluorescent signal. However, the repeatability of this method was low and therefore it was discarded.

A second method was explored which enhances protein adsorption by increasing the material hydrophobicity. A silane coat was applied prior to ECM protein incubation and a water contact angle of 120° was achieved. The common non-specific adsorption problem of hydrophobic surfaces was eased by pressing the ECM protein against the silane coating with a piece of glass. The successful samples had a uniform coating with a stronger fluorescent signal than microprinting technique; nevertheless, the repeatability of this method was only 35%.

Next method that was revised was a chemical method using crosslinkers to achieve a covalent bond between the ECM protein and PDMS surfaces. Glutaraldehyde crosslinker was used first due to its low cost, but it caused non-uniform coatings because of its self-crosslinking effect on proteins. Thus, the crosslinker was changed to EDC/NHS which creates covalent bonds without protein self-crosslinking. This functionalization was characterized using the midland blotting procedure that validates the presence of carboxyl groups ($-\text{COOH}$) in the PDMS surface. This method was used for the final experiments because it achieved a uniform coating with moderate fluorescence signal and high repeatability of 90% of successful samples.

During data acquisition, cancerous epithelial cell lines A549, NCI-H226 and HDF fibroblasts were cultivated on the devices and videos of its migration were recorded. It was decided to begin the studies as proof of principle with devices from design #2 which has 3 μm diameter. Stiffness of the pillars of this device was calculated with the assumption that every pillar has a length of 5 μm and a Young modulus of 2 MPa and it was obtained a stiffness of 155.969 nN/ μm . Each measurement of micropillar deflection was multiplied by this stiffness to calculate the exerted force caused by cell migration.

Then a novel MATLAB code was created to detect the micropillars deflection caused by the forces exerted by the cell. This code stored each video frame in a variable, converted frames to grayscale, detected coordinates of circular objects in every frame, linked detected circular objects on every frame to the previous one, calculated the displacement of every pillar over time, corrected noise from measurements and exported the results in an excel file. These measurements were noisy due to slight variation in the detection of micropillar centres and it was needed to apply a Gaussian filter to remove it.

Results showed that the overall mode force values were 1 nN for epithelial cells A549 and NCI-H226 respectively. This equality in overall mode forces in cells A549 and NCI-H226 suggest that globally these cells have a similar manner to exert forces; however, locally they have key differences such as migration times (8 min vs 36 min) and maximal local mode force values (54.05 nN vs 13.26 nN). It is concluded that A549 were stronger but less motile than NCI-H226 cells.

The overall force of HDF fibroblasts had a median value of 0.5 nN. This low median force was a consequence of the minimal migration on this micropillar device with a maximum local mode force value of 37.5 nN. Additionally, it was seen that cells only migrate for 3 min suggesting that this micropillar device is not suitable to study fibroblasts and therefore, a micropillar device with a bigger stiffness must be designed for HDF fibroblasts migration studies.

Furthermore, insights into cell migration prediction were seen. Cell exerted bigger forces either in the front or the back of the cell before moving forward. Before turning right or left, cell exerted bigger forces on the side where it was going to move next. As part of the migration, cell extended its lamellipodium in search of places to continue migration; it was seen that cell first pushes several micropillars in the surrounding area.

Then, cell attached a focal point on the tip of the micropillar where it decided to migrate next.

The performed studies in this thesis proved that micropillars with 3 μm length and 5 μm length are suitable for epithelial cell migration studies with a force resolution of 0.01 nN.

6.1 Future work

It is suggested as future work to improve the ECM protein functionalization in the micropillar devices to reduce the noise caused by the MATLAB algorithm. This will increase the efficiency of the devices and improve the force resolution.

Results from this project assumed that PDMS has a young modulus of 2 MPa according to the manufacturer's recipe. This value of young modulus should be measured as small changes in the value of the young modulus could compromise the results. This could be done by performing a lateral force measurement using an AFM in the tip of a single micropillar which gives realistic data instead of using FEA approximation. Apart from obtaining the young modulus, this type of measurements can give other useful information such as micropillar spring constant, maximum deflection and measure quantity of adsorbed protein.

Furthermore, it is proposed to perform more studies with different epithelial cell lines with micropillar with 3 μm diameter and 5 μm length used in this thesis along with micropillars with 2 μm diameter from design #1 which is expected to have a higher sensitivity. A record of the local forces on each epithelial cell line can provide a powerful tool to differentiate cells from each other. This information could help researchers to study the effect of drugs in the migration behaviour of epithelial cells by adding these drugs to the cell media which could lead to the potential development of treatments to stop metastasis.

The observations in the cell decision-making path need to be studied more in depth. A better understanding of how cancerous cells decide its migration path, could lead to the development of drugs to control cell migration. Here, it is proposed to perform these studies in the micropillars designs 3, 7, 10 and 11 which were initially designed to study cell behaviour but were not tested in this project.

It is also suggested to perform studies using micropillars from designs 4, 8 and 9 could lead to developing tools to confine certain cells lines in a desired area, this could be used in microfluidics devices to sense the presence of a specific cell line.

References

- [1] W. H. Organization. "Cancer." World Health Organization. <https://www.who.int/en/news-room/fact-sheets/detail/cancer> (accessed 4/01/2019, 2019).
- [2] N. C. Institute. "What is cancer?" National cancer institute. <https://www.cancer.gov/about-cancer/understanding/what-is-cancer> (accessed 4/01/2019, 2019).
- [3] W. H. Organization. "World fact sheets." World Health Organization. <http://gco.iarc.fr/today/data/factsheets/populations/900-world-fact-sheets.pdf> (accessed 4/01/2019, 2019).
- [4] S. E. Cross, Y.-S. Jin, J. Rao, and J. K. Gimzewski, "Nanomechanical analysis of cells from cancer patients," *Nature nanotechnology*, vol. 2, no. 12, pp. 780-783, 2007.
- [5] K. D. Costa, A. J. Sim, and F. C. P. Yin, "Non-Hertzian Approach to Analyzing Mechanical Properties of Endothelial Cells Probed by Atomic Force Microscopy," *Journal of Biomechanical Engineering*, vol. 128, no. 2, pp. 176-184, 2005, doi: 10.1115/1.2165690.
- [6] C. Dalmay, A. Pothier, M. Cheray, F. Lalloué, M.-O. Jauberteau, and P. Blondy, "On-chip biosensors based on microwave detection for cell scale investigations," in *Biomedical Engineering Systems and Technologies*: Springer, 2010, pp. 51-63.
- [7] R. Ananthkrishnan and A. Ehrlicher, "The forces behind cell movement," *International journal of biological sciences*, vol. 3, no. 5, p. 303, 2007.
- [8] D. A. Lauffenburger and A. F. Horwitz, "Cell migration: a physically integrated molecular process," *Cell*, vol. 84, no. 3, pp. 359-369, 1996.
- [9] P. Heil and J. P. Spatz, "Lateral shear forces applied to cells with single elastic micropillars to influence focal adhesion dynamics," *Journal of Physics: Condensed Matter*, vol. 22, no. 19, p. 194108, 2010.
- [10] A. Saez, M. Ghibaudo, A. Buguin, P. Silberzan, and B. Ladoux, "Rigidity-driven growth and migration of epithelial cells on microstructured anisotropic substrates," *Proceedings of the National Academy of Sciences*, vol. 104, no. 20, pp. 8281-8286, 2007.
- [11] B. C. Isenberg, P. A. DiMilla, M. Walker, S. Kim, and J. Y. Wong, "Vascular smooth muscle cell durotaxis depends on substrate stiffness gradient strength," *Biophysical journal*, vol. 97, no. 5, pp. 1313-1322, 2009.
- [12] C.-M. Lo, H.-B. Wang, M. Dembo, and Y.-I. Wang, "Cell movement is guided by the rigidity of the substrate," *Biophysical journal*, vol. 79, no. 1, pp. 144-152, 2000.
- [13] S. Lee, J. Hong, and J. Lee, "Cell motility regulation on a stepped micro pillar array device (SMPAD) with a discrete stiffness gradient," *Soft Matter*, 10.1039/C5SM00649J vol. 12, no. 8, pp. 2325-2333, 2016, doi: 10.1039/C5SM00649J.
- [14] N. Zaari, P. Rajagopalan, S. K. Kim, A. J. Engler, and J. Y. Wong, "Photopolymerization in microfluidic gradient generators: microscale control of substrate compliance to manipulate cell response," *Advanced Materials*, vol. 16, no. 23-24, pp. 2133-2137, 2004.
- [15] J. A. Burdick, A. Khademhosseini, and R. Langer, "Fabrication of gradient hydrogels using a microfluidics/photopolymerization process," *Langmuir : the ACS journal of surfaces and colloids*, vol. 20, no. 13, pp. 5153-5156, 2004.
- [16] J. Y. Wong, A. Velasco, P. Rajagopalan, and Q. Pham, "Directed movement of vascular smooth muscle cells on gradient-compliant hydrogels," *Langmuir : the ACS journal of surfaces and colloids*, vol. 19, no. 5, pp. 1908-1913, 2003.
- [17] D. S. Gray, J. Tien, and C. S. Chen, "Repositioning of cells by mechanotaxis on surfaces with micropatterned Young's modulus," *Journal of Biomedical Materials Research Part A*, vol. 66, no. 3, pp. 605-614, 2003.
- [18] S. Kidoaki and T. Matsuda, "Microelastic gradient gelatinous gels to induce cellular mechanotaxis," *Journal of biotechnology*, vol. 133, no. 2, pp. 225-230, 2008.
- [19] K. O. Okeyo, H. Miyoshi, and T. Adachi, *Innovative Approaches to Cell Biomechanics*. Springer, 2015.

- [20] S. Kidambi, N. Udpa, S. A. Schroeder, R. Findlan, I. Lee, and C. Chan, "Cell adhesion on polyelectrolyte multilayer coated polydimethylsiloxane surfaces with varying topographies," *Tissue engineering*, vol. 13, no. 8, pp. 2105-2117, 2007.
- [21] M. Ghibaudo, L. Trichet, J. Le Digabel, A. Richert, P. Hersen, and B. Ladoux, "Substrate Topography Induces a Crossover from 2D to 3D Behavior in Fibroblast Migration," *Biophysical Journal*, vol. 97, no. 1, pp. 357-368, 7/8/ 2009, doi: <http://dx.doi.org/10.1016/j.bpj.2009.04.024>.
- [22] N. Scuor, P. Gallina, H. V. Panchawagh, R. L. Mahajan, O. Sbaizero, and V. Sergo, "Design of a novel MEMS platform for the biaxial stimulation of living cells," *Biomedical microdevices*, vol. 8, no. 3, pp. 239-246, 2006.
- [23] R. Swierczewski, J. Hedley, and C. P. F. Redfern, "High-resolution micromechanical measurement in real time of forces exerted by living cells," *Cell Adhesion & Migration*, vol. 10, no. 3, pp. 322-330, 2016/05/03 2016, doi: 10.1080/19336918.2015.1120398.
- [24] R. Swierczewski, J. Vazquez, J. Hedley, M. Birch, and C. Redfern, "Microsystem for Real Time High Resolution Measurement of Cell Forces," *Sensors Journal, IEEE*, vol. 13, no. 5, pp. 1602-1609, 2013.
- [25] M. Gupta, L. Kocgozlu, B. R. Sarangi, F. Margadant, M. Ashraf, and B. Ladoux, "Micropillar substrates: A tool for studying cell mechanobiology," *Methods in cell biology*, vol. 125, pp. 289-308, 2015.
- [26] O. Du Roure *et al.*, "Force mapping in epithelial cell migration," *Proceedings of the National Academy of Sciences of the United States of America*, vol. 102, no. 7, pp. 2390-2395, 2005.
- [27] J. Le Digabel, M. Ghibaudo, L. Trichet, A. Richert, and B. Ladoux, "Microfabricated substrates as a tool to study cell mechanotransduction," *Medical & biological engineering & computing*, vol. 48, no. 10, pp. 965-976, 2010.
- [28] L. E. Dickinson, D. R. Rand, J. Tsao, W. Eberle, and S. Gerecht, "Endothelial cell responses to micropillar substrates of varying dimensions and stiffness," *Journal of Biomedical Materials Research Part A*, vol. 100, no. 6, pp. 1457-1466, 2012.
- [29] H. van Hoorn *et al.*, "The nanoscale architecture of force-bearing focal adhesions," *Nano letters*, vol. 14, no. 8, pp. 4257-4262, 2014.
- [30] M. Ghibaudo *et al.*, "Traction forces and rigidity sensing regulate cell functions," *Soft Matter*, vol. 4, no. 9, pp. 1836-1843, 2008.
- [31] A. Saez, A. Buguin, P. Silberzan, and B. Ladoux, "Is the mechanical activity of epithelial cells controlled by deformations or forces?," *Biophysical journal*, vol. 89, no. 6, pp. L52-L54, 2005.
- [32] J. Fu *et al.*, "Mechanical regulation of cell function with geometrically modulated elastomeric substrates," *Nature methods*, vol. 7, no. 9, p. 733, 2010.
- [33] A. T. Higa, "Cellular mechanotransduction via microfabricated post arrays," University of California, Berkeley, 2012.
- [34] A. Jasaitis, M. Estevez, J. Heysch, B. Ladoux, and S. Dufour, "E-cadherin-dependent stimulation of traction force at focal adhesions via the Src and PI3K signaling pathways," *Biophysical journal*, vol. 103, no. 2, pp. 175-184, 2012.
- [35] Y. J. Chuah, S. Kuddannaya, M. H. A. Lee, Y. Zhang, and Y. Kang, "The effects of poly (dimethylsiloxane) surface silanization on the mesenchymal stem cell fate," *Biomaterials science*, vol. 3, no. 2, pp. 383-390, 2015.
- [36] J. L. Tan, J. Tien, D. M. Pirone, D. S. Gray, K. Bhadriraju, and C. S. Chen, "Cells lying on a bed of microneedles: an approach to isolate mechanical force," *Proceedings of the National Academy of Sciences*, vol. 100, no. 4, pp. 1484-1489, 2003.
- [37] A. Saez *et al.*, "Traction forces exerted by epithelial cell sheets," *Journal of Physics: Condensed Matter*, vol. 22, no. 19, p. 194119, 2010.
- [38] N. Q. Balaban *et al.*, "Force and focal adhesion assembly: a close relationship studied using elastic micropatterned substrates," *Nature cell biology*, vol. 3, no. 5, p. 466, 2001.
- [39] A. Ganz *et al.*, "Traction forces exerted through N-cadherin contacts," *Biology of the Cell*, vol. 98, no. 12, pp. 721-730, 2006.
- [40] D. Venes, *Cyclopedic Medical Dictionary*: F. A. Davis Company, 2005. [Online]. Available: <http://NCL.ebib.com/patron/FullRecord.aspx?p=253406>.

- [41] S. Ghassemi, N. Biais, K. Maniura, S. J. Wind, M. P. Sheetz, and J. Hone, "Fabrication of elastomer pillar arrays with modulated stiffness for cellular force measurements," *Journal of Vacuum Science & Technology B: Microelectronics and Nanometer Structures Processing, Measurement, and Phenomena*, vol. 26, no. 6, pp. 2549-2553, 2008.
- [42] F. Boccafoschi, M. Rasponi, C. Mosca, E. Bocchi, and S. Vesentini, "Study of cellular adhesion by means of micropillar surface topologies," in *Advanced materials research*, 2012, vol. 409: Trans Tech Publ, pp. 105-110.
- [43] G. Bao and S. Suresh, "Cell and molecular mechanics of biological materials," *Nature materials*, vol. 2, no. 11, pp. 715-725, 2003.
- [44] D. Chandra, "Capillary force in high aspect-ratio micropillar arrays," 2009.
- [45] N. Klejwa, N. Harjee, R. Kwon, S. M. Coulthard, and B. L. Pruitt, "Transparent SU-8 three-axis micro strain gauge force sensing pillar arrays for biological applications," in *Solid-State Sensors, Actuators and Microsystems Conference, 2007. TRANSDUCERS 2007. International*, 2007: IEEE, pp. 2259-2262.
- [46] A. D. Theocharis, S. S. Skandalis, C. Gialeli, and N. K. Karamanos, "Extracellular matrix structure," *Advanced drug delivery reviews*, vol. 97, pp. 4-27, 2016.
- [47] G. Plopper, B. Lewin, L. Cassimeris, V. Lingappa, and G. Plopper, "The extracellular matrix and cell adhesion, Cells," ed: Jones and Bartlett, Sudbury, 2007.
- [48] D. Riveline *et al.*, "Focal Contacts as Mechanosensors," *Externally Applied Local Mechanical Force Induces Growth of Focal Contacts by an Mdia1-Dependent and Rock-Independent Mechanism*, vol. 153, no. 6, pp. 1175-1186, 2001, doi: 10.1083/jcb.153.6.1175.
- [49] J. Xiao *et al.*, "PDMS micropillar-based microchip for efficient cancer cell capture," *RSC Advances*, vol. 5, no. 64, pp. 52161-52166, 2015.
- [50] S. M. Khare, A. Awasthi, V. Venkataraman, and S. P. Koushika, "Colored polydimethylsiloxane micropillar arrays for high throughput measurements of forces applied by genetic model organisms," *Biomicrofluidics*, vol. 9, no. 1, p. 014111, 2015.
- [51] I. Schoen, W. Hu, E. Klotzsch, and V. Vogel, "Probing cellular traction forces by micropillar arrays: contribution of substrate warping to pillar deflection," *Nano letters*, vol. 10, no. 5, pp. 1823-1830, 2010.
- [52] D. Bray, "Critical point drying of biological specimens for scanning electron microscopy," *Supercritical Fluid Methods and Protocols*, pp. 235-243, 2000.
- [53] P. Echlin, *Handbook of sample preparation for scanning electron microscopy and X-ray microanalysis*. Springer Science & Business Media, 2011.
- [54] S. Kuddannaya, Y. J. Chuah, M. H. A. Lee, N. V. Menon, Y. Kang, and Y. Zhang, "Surface chemical modification of poly (dimethylsiloxane) for the enhanced adhesion and proliferation of mesenchymal stem cells," *ACS applied materials & interfaces*, vol. 5, no. 19, pp. 9777-9784, 2013.
- [55] T. E. o. E. Britannica. "Adsorption." Encyclopædia Britannica.
<http://www.britannica.com/science/bone-anatomy/Vascular-supply-and-circulation>
(accessed 21 January 2019, 2019).
- [56] K. Nakanishi, T. Sakiyama, and K. Imamura, "On the adsorption of proteins on solid surfaces, a common but very complicated phenomenon," *Journal of bioscience and bioengineering*, vol. 91, no. 3, pp. 233-244, 2001.
- [57] M. Rabe, D. Verdes, and S. Seeger, "Understanding protein adsorption phenomena at solid surfaces," *Advances in colloid and interface science*, vol. 162, no. 1-2, pp. 87-106, 2011.
- [58] M. Wahlgren and T. Arnebrant, "Protein adsorption to solid surfaces," *Trends in biotechnology*, vol. 9, no. 1, pp. 201-208, 1991.
- [59] R. Morent *et al.*, "Adhesion enhancement by a dielectric barrier discharge of PDMS used for flexible and stretchable electronics," *Journal of Physics D: Applied Physics*, vol. 40, no. 23, p. 7392, 2007.
- [60] L. Yu, Z. Lu, Y. Gan, Y. Liu, and C. M. Li, "AFM study of adsorption of protein A on a poly (dimethylsiloxane) surface," *Nanotechnology*, vol. 20, no. 28, p. 285101, 2009.

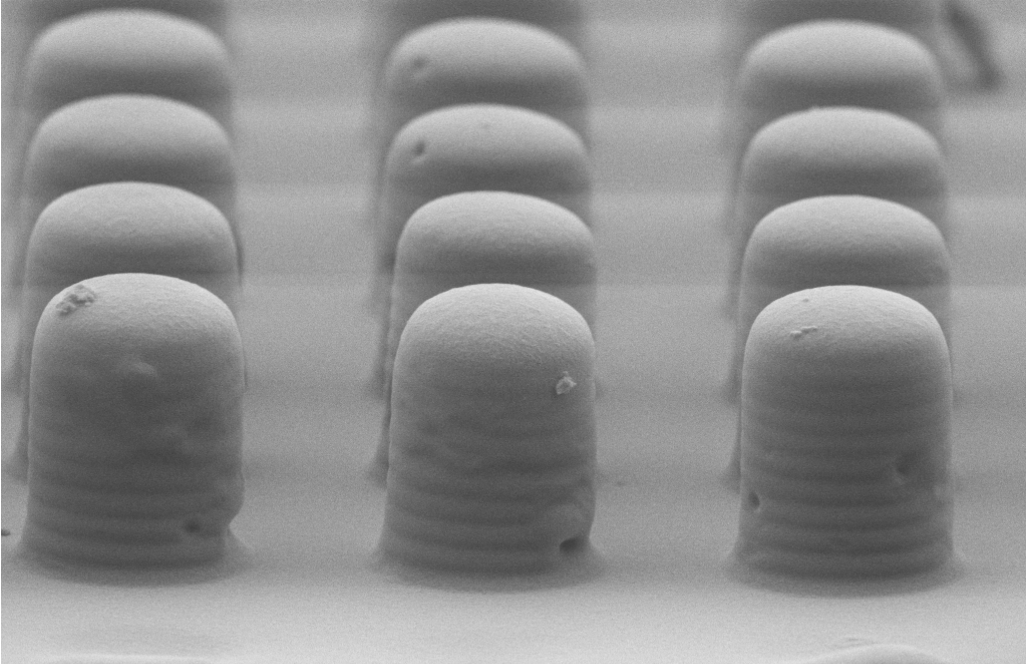
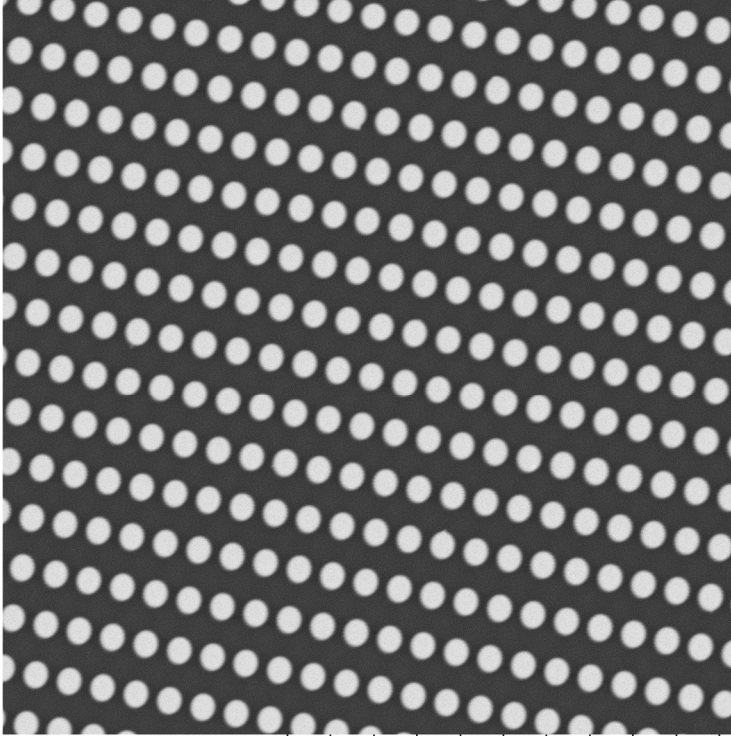
- [61] Y. Koga, P. Westh, K. Nishikawa, and S. Subramanian, "Is a methyl group always hydrophobic? Hydrophilicity of trimethylamine-N-oxide, tetramethyl urea and tetramethylammonium ion," *The Journal of Physical Chemistry B*, vol. 115, no. 12, pp. 2995-3002, 2011.
- [62] A. Sethuraman, M. Han, R. S. Kane, and G. Belfort, "Effect of surface wettability on the adhesion of proteins," *Langmuir : the ACS journal of surfaces and colloids*, vol. 20, no. 18, pp. 7779-7788, 2004.
- [63] S. Demming, C. Lesche, H. Schmolke, C. P. Klages, and S. Büttgenbach, "Characterization of long-term stability of hydrophilized PEG-grafted PDMS within different media for biotechnological and pharmaceutical applications," *Physica status solidi (a)*, vol. 208, no. 6, pp. 1301-1307, 2011.
- [64] A. Gokaltun, M. L. Yarmush, A. Asatekin, and O. B. Usta, "Recent advances in nonbiofouling PDMS surface modification strategies applicable to microfluidic technology," *Technology*, vol. 5, no. 01, pp. 1-12, 2017.
- [65] S. H. Tan, N.-T. Nguyen, Y. C. Chua, and T. G. Kang, "Oxygen plasma treatment for reducing hydrophobicity of a sealed polydimethylsiloxane microchannel," *Biomicrofluidics*, vol. 4, no. 3, p. 032204, 2010.
- [66] A. Mata, A. J. Fleischman, and S. Roy, "Characterization of polydimethylsiloxane (PDMS) properties for biomedical micro/nanosystems," *Biomedical microdevices*, vol. 7, no. 4, pp. 281-293, 2005.
- [67] Y. Kameya, "Wettability modification of polydimethylsiloxane surface by fabricating micropillar and microhole arrays," *Materials Letters*, vol. 196, pp. 320-323, 2017.
- [68] K. Wang, G. Ouyang, and X. Chen, "Surface modification and wettability of silicone PDMS film," in *Electronic System-Integration Technology Conference (ESTC), 2010 3rd*, 2010: IEEE, pp. 1-3.
- [69] D. Bodas and C. Khan-Malek, "Formation of more stable hydrophilic surfaces of PDMS by plasma and chemical treatments," *Microelectronic engineering*, vol. 83, no. 4-9, pp. 1277-1279, 2006.
- [70] S. ALDRICH. "Fibronectin from bovine plasma powder." Sigma Aldrich. https://www.sigmaaldrich.com/content/dam/sigma-aldrich/docs/Sigma/Product_Information_Sheet/f4759pis.pdf (accessed 20 October, 2017).
- [71] E. Gasteiger, C. Hoogland, A. Gattiker, M. R. Wilkins, R. D. Appel, and A. Bairoch, "Protein identification and analysis tools on the ExPASy server," in *The proteomics protocols handbook*: Springer, 2005, pp. 571-607.
- [72] iSpyBio. "Protein labeling with FITC." iSpyBio. <http://www.ispybio.com/search/protocols/fitc%20protocol3.pdf> (accessed).
- [73] ThermoScientific. "Zeba Spin Desalting Columns, 40K MWCO." https://assets.thermofisher.com/TFS-Assets/LSG/manuals/MAN0011691_Zeba_Spin_DesaltCol_Plate_40K_MWCO_UG.pdf (accessed).
- [74] S. ALDRICH. "FLUORESCCEIN ISOTHIOCYANATE." https://www.sigmaaldrich.com/content/dam/sigma-aldrich/docs/Sigma/Product_Information_Sheet/f7250pis.pdf (accessed 15/05/2019).
- [75] U. K. Laemmli, "Cleavage of structural proteins during the assembly of the head of bacteriophage T4," *nature*, vol. 227, no. 5259, p. 680, 1970.
- [76] F. He, "Laemmli-sds-page," *Bio-protocolBio101: e80*, 2011.
- [77] F. Analytics. "How SDS-PAGE works." bitesizebio. <https://bitesizebio.com/580/how-sds-page-works/> (accessed 13/05/2019).
- [78] D. R. Caprette. "Preparing Protein Samples for Electrophoresis." RICE university. <https://www.ruf.rice.edu/~bioslabs/studies/sds-page/denature.html> (accessed 13/05/2019).
- [79] F. von Post, "Microcontact printing of antibodies in complex with conjugated polyelectrolytes," ed: Institutionen för fysik, kemi och biologi, 2007.
- [80] M. Théry and M. Piel, "Adhesive micropatterns for cells: a microcontact printing protocol," *Cold Spring Harbor Protocols*, vol. 2009, no. 7, p. pdb. prot5255, 2009.

- [81] Y. Xia and G. M. Whitesides, "Soft lithography," *Annual review of materials science*, vol. 28, no. 1, pp. 153-184, 1998.
- [82] A. Bernard, J. P. Renault, B. Michel, H. R. Bosshard, and E. Delamarche, "Microcontact printing of proteins," *Advanced Materials*, vol. 12, no. 14, pp. 1067-1070, 2000.
- [83] E. Menard and J. Rogers, "Stamping techniques for micro-and nanofabrication," *Springer Handbook of Nanotechnology*, pp. 279-298, 2007.
- [84] T. Kaufmann and B. J. Ravoo, "Stamps, inks and substrates: polymers in microcontact printing," *Polymer Chemistry*, vol. 1, no. 4, pp. 371-387, 2010.
- [85] S. Bhattacharya, A. Datta, J. M. Berg, and S. Gangopadhyay, "Studies on surface wettability of poly (dimethyl) siloxane (PDMS) and glass under oxygen-plasma treatment and correlation with bond strength," *Journal of microelectromechanical systems*, vol. 14, no. 3, pp. 590-597, 2005.
- [86] T. Trantidou, Y. Elani, E. Parsons, and O. Ces, "Hydrophilic surface modification of PDMS for droplet microfluidics using a simple, quick, and robust method via PVA deposition," *Microsystems & Nanoengineering*, vol. 3, p. 16091, 2017.
- [87] A. Siddique, T. Meckel, R. W. Stark, and S. Narayan, "Improved cell adhesion under shear stress in PDMS microfluidic devices," *Colloids and Surfaces B: Biointerfaces*, vol. 150, pp. 456-464, 2017.
- [88] L. Yu, C. M. Li, and Q. Zhou, "Efficient probe immobilization on poly (dimethylsiloxane) for sensitive detection of proteins," *Front. Biosci*, vol. 10, pp. 2848-2855, 2005.
- [89] H. Xia, B. Mathew, T. John, H. Hegab, and J. Feng, "Microfluidic based immunosensor for detection and purification of carbonylated proteins," *Biomedical microdevices*, vol. 15, no. 3, pp. 519-530, 2013.
- [90] V. C. Pinto, G. Minas, and M. Correia-Neves, "PDMS biofunctionalization study for the development of a microfluidic device: Application to salivary cortisol," in *2015 IEEE 4th Portuguese Meeting on Bioengineering (ENBENG)*, 2015: IEEE, pp. 1-5.
- [91] B. Ladoux *et al.*, "Strength dependence of cadherin-mediated adhesions," *Biophysical journal*, vol. 98, no. 4, pp. 534-542, 2010.
- [92] J. N. Lee, C. Park, and G. M. Whitesides, "Solvent compatibility of poly (dimethylsiloxane)-based microfluidic devices," *Analytical chemistry*, vol. 75, no. 23, pp. 6544-6554, 2003.
- [93] R. Khnouf, D. Karasneh, and B. A. Albiss, "Protein immobilization on the surface of polydimethylsiloxane and polymethyl methacrylate microfluidic devices," *Electrophoresis*, vol. 37, no. 3, pp. 529-535, 2016.
- [94] R. Khnouf and D. Karasneh, "Polydimethyl siloxane microfluidic channel protein functionalization techniques," in *2016 IEEE 11th Annual International Conference on Nano/Micro Engineered and Molecular Systems (NEMS)*, 2016: IEEE, pp. 409-413.
- [95] J. Kim, J. Cho, P. M. Seidler, N. E. Kurland, and V. K. Yadavalli, "Investigations of chemical modifications of amino-terminated organic films on silicon substrates and controlled protein immobilization," *Langmuir : the ACS journal of surfaces and colloids*, vol. 26, no. 4, pp. 2599-2608, 2010.
- [96] K. C. Tang *et al.*, "Evaluation of bonding between oxygen plasma treated polydimethyl siloxane and passivated silicon," in *Journal of Physics: Conference Series*, 2006, vol. 34: IOP Publishing, p. 155.
- [97] I. Migneault, C. Dartiguenave, M. J. Bertrand, and K. C. Waldron, "Glutaraldehyde: behavior in aqueous solution, reaction with proteins, and application to enzyme crosslinking," *Biotechniques*, vol. 37, no. 5, pp. 790-802, 2004.
- [98] H. Yuan, W. M. Mullett, and J. Pawliszyn, "Biological sample analysis with immunoaffinity solid-phase microextraction," *Analyst*, vol. 126, no. 8, pp. 1456-1461, 2001.
- [99] ThermoScientific. "Crosslinking Reagents Technical Handbook." ThermoFisher. <https://tools.thermofisher.com/content/sfs/brochures/1602163-Crosslinking-Reagents-Handbook.pdf> (accessed 11/07/2019).
- [100] C. Wang, Q. Yan, H.-B. Liu, X.-H. Zhou, and S.-J. Xiao, "Different EDC/NHS activation mechanisms between PAA and PMAA brushes and the following amidation reactions," *Langmuir : the ACS journal of surfaces and colloids*, vol. 27, no. 19, pp. 12058-12068, 2011.

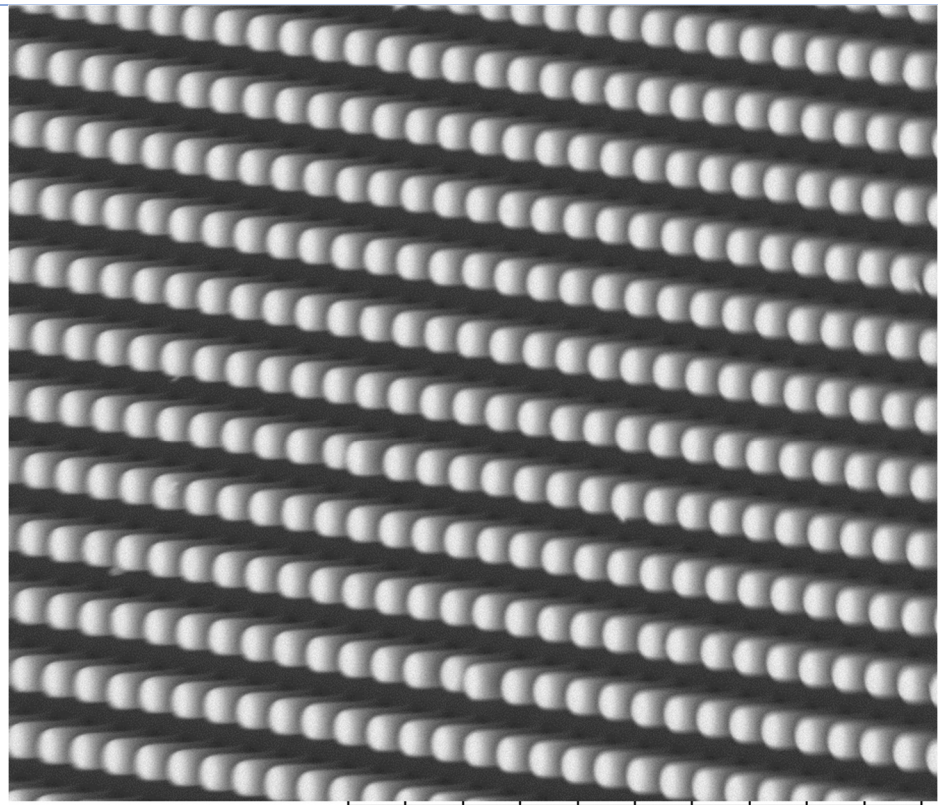
- [101] A. M. Lowe, B. H. Ozer, G. J. Wiepz, P. J. Bertics, and N. L. Abbott, "Engineering of PDMS surfaces for use in microsystems for capture and isolation of complex and biomedically important proteins: Epidermal growth factor receptor as a model system," *Lab on a Chip*, vol. 8, no. 8, pp. 1357-1364, 2008.
- [102] J. V. Rushworth, A. Ahmed, and P. A. Millner, "Midland Blotting: A Rapid, Semi-Quantitative Method for Biosensor Surface Characterization," *J Biosens Bioelectron*, vol. 4, no. 146, p. 2, 2013.
- [103] L. Miller, "Analyzing gels and western blots with ImageJ," *Lukemiller.org Miscellaneous Topics Vaguely Related to Science*, 2010.
- [104] Y. L.-U. o. C. Davis. "Traction force analysis: a migrating cell on a microfabricated pillar array." Yamalda Lab. https://www.youtube.com/watch?v=0SbLuq_DBOs (accessed 3/8/2016, 2016).
- [105] R. G. Brown and P. Y. Hwang, *Introduction to random signals and applied Kalman filtering*. Wiley New York, 1992.

Appendix A

Table A 1. SEM images of some fabricated micropillar devices

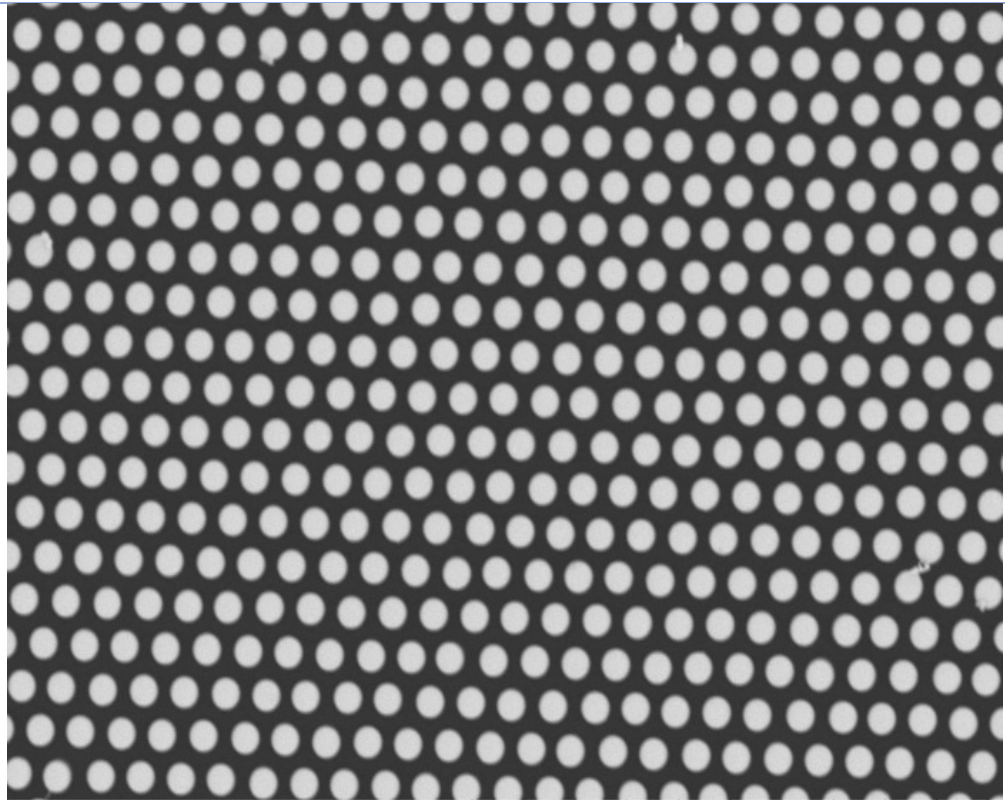
Design #	Micropillar design
2	 <p>1 μm EHT = 4.00 kV Signal A = SE2 Date :25 Oct 2018 WD = 6.5 mm Mag = 17.44 K X Aperture Size = 30.00 μm ZEISS</p> <p>This SEM image shows three columns of micropillars. Each pillar has a rounded top and a cylindrical body with horizontal ridges. The pillars are arranged in a regular grid pattern.</p>
3	 <p>2017-03-16 NL D7.9 x1.5k 50 μm</p> <p>This SEM image shows a dense array of micropillars, appearing as a regular grid of bright circular spots against a dark background. The pillars are arranged in a regular grid pattern.</p>

3



2017-03-16 NL D8.0 x1.5k 50 μm

7



2017-03-16 NL D6.6 x1.5k 50 μm

